Fakultät Mathematik und Naturwissenschaften
Technische Universität Dresden

Theoretical studies of carbon-based nanostructured materials with applications in hydrogen storage

von

M.Sc. Agnieszka Kuc

2008

THEORETICAL STUDIES OF CARBON-BASED NANOSTRUCTURED MATERIALS WITH APPLICATIONS IN HYDROGEN STORAGE

DISSERTATION

zur Erlangung des akademischen Grades
Doctor rerum naturalium
(Dr. rer. nat.)

vorgelegt
der Fakultät Mathematik und Naturwissenschaften der
Technischen Universität Dresden

von
M.Sc. Agnieszka Kuc

geboren am 01.08.1978 in Brzeg (Polen)

Gutachter:

Eingereicht am:
Tag der Verteidigung:

Acknowledgment

I would like to thank the people who contributed in different ways to the realization of this work. Special thanks:

To my supervisor, **Prof. Gotthard Seifert**, for advising and supporting me constantly during these years, for many fruitful and motivating discussions.
To **Prof. Thomas Heine** for helpful and interesting discussions, for introduction to the Fortran 77/90 programming language, and the possibility of participation in international collaboration.
To **Dr. Jan-Ole Joswig** for proof-reading of this thesis, for hints in LaTeX usage, and being a great partner in the practical teaching team.
To **Dr. Johannes Frenzel** for the introduction to computational programs and to LaTeX, for help in professional and everyday life.
To **Knut Vietze** for constant computational assistance and proof-reading of a part of this thesis.
To **Prof. Hélio Anderson Duarte** from UFMG, Belo Horizonte, and **his group** for the opportunity to collaborate during my visit in Brazil.
To the **referees** and the **members** of the commission who accepted to judge this work.
To **Dr. Andrey Enyashin** and **Dr. Lyuben Zhechkov** for their collaboration and contribution to this work.
To **Regina Luschtinetz** for help in everyday life.
To **Prof. Malcolm Heggie** and **Dr. Irene Suarez-Martinez** for kindly providing me the structures of defected and screw dislocated graphite.
To **Dr. Helmut Hermann** for opportunity to work experimentally on the hydrogen storage in nanoporous materials.
To **Mrs. Siegrid Hehme** for help with everyday bureaucracy.
To my **friends** and **colleagues** from the group for nice time spent in Germany.
To Stiftung Energieforschung BW, Deutscher Akademischer Austauschdienst, DAAD, in cooperation with the Brazilian Agencies Coordenação de Aperfeiçoamento de Pessoal de Nível Superior, CAPES, for financial support.

Finally my most sincere thanks go to the people who always supported me during these PhD studies:

To my best friend **Agnieszka Kawska** for years of friendship and support in professional and everyday life.
To my good friends **Dr. Agnieszka Jaron-Becker** and **Dr. Andreas Becker** for proof-reading of this thesis, the introduction to GAMESS-UK and help with Gaussian03.
Um agradecimento especial é para o meu namorado **Dr. Augusto Faria Oliveira**, que faz parte da minha vida há vários anos e que cuja inacreditável paciência e apoio, tanto na vida profissional como no dia-a-dia, merece muito mais do que apenas palavras.
Specialne podziękowania dla **mojej rodziny**, mamy i tata, mojej siostry i jej rodziny, których wsparcie i cierpliwość zasługują na dużo więcej niż tylko słowa.

Chemistry began by saying it would change the baser metals into gold.
By not doing that it has done much greater things.
Ralph Waldo Emerson

Contents

1 INTRODUCTION 1

2 METHODOLOGY 9
- 2.1 Theoretical Background . . . 11
  - 2.1.1 The Schrödinger Equation . . . 11
  - 2.1.2 Born-Oppenheimer Approximation . . . 12
  - 2.1.3 Hartree-Fock Method . . . 13
  - 2.1.4 Pseudopotentials . . . 15
- 2.2 Møller-Plesset Perturbation Theory . . . 15
- 2.3 Density Functional Theory . . . 18
  - 2.3.1 Basis Sets . . . 20
- 2.4 Density Functional based Tight-Binding . . . 22

3 CARBON STRUCTURES 27
- 3.1 Carbon Foams . . . 30
  - 3.1.1 Computational Details . . . 32
  - 3.1.2 Structure . . . 34
  - 3.1.3 Energetic and Mechanical Stability . . . 40
  - 3.1.4 Electronic Properties . . . 44
  - 3.1.5 Foams Intercalated by Carbon Nanotubes . . . 47
  - 3.1.6 Defected Graphite . . . 49
- 3.2 C_{60}-Intercalated Graphite . . . 51
  - 3.2.1 Computational Details . . . 52
  - 3.2.2 Structure . . . 53
  - 3.2.3 Energetic Stability and Electronic Properties . . . 54
- 3.3 Summary . . . 55

4 METAL-ORGANIC FRAMEWORKS 59
4.1 Zn-Based Metal-Organic Frameworks 63
4.1.1 Computational Details 65
4.1.2 Structures 66
4.1.3 Energetic and Mechanical Stability 73
4.1.4 Electronic Properties 75
4.2 A Cu-Based Metal-Organic Framework 81
4.2.1 Structure 81
4.2.2 Electronic Properties 84
4.3 Interactions between H_2 and Metal-Organic Frameworks . . . 86
4.3.1 Model Structures and Validity of Methods 88
4.3.2 H_2 Interaction with Building Blocks 95
4.4 Summary 100

5 CONCLUSIONS 103

Chapter 1

Introduction

The increasing worldwide demand of energy, recognized in the recent years, has placed considerable strain on conventional sources, such as coal and petroleum. This fact, combined with concerns about environmental pollution arising from high CO_2 emissions, has led to a rapid development of technologies based on alternative energy sources, e.g. hydrogen or natural gas. However, their application on a large commercial scale has been impended by the absence of safe and economic techniques for an on-board storage.

Hydrogen is considered widely as the best overall solution in the long run, due to its pollutant-free combustion, which produces exclusively energy and water. Moreover, it is the most abundant element in the universe, although only less than 1 % is present as molecular hydrogen. In majority it is found chemically bound in water and, moreover, some is bound in liquid or gaseous hydrocarbons. Hydrogen possesses a three times larger chemical energy per mass unit than conventionally used liquid hydrocarbons (142 $\mathrm{MJmol^{-1}}$ and 47 $\mathrm{MJmol^{-1}}$ for hydrogen and hydrocarbons, respectively).[1] These features of hydrogen make it an excellent energy carrier.

There are major research challenges to overcome before technologies based on hydrogen as an energy source can be implemented in order to substitute conventional petroleum. Although first attempts of vehicles powered by hydrogen fuel cells have appeared as early as 1959 (Allis-Chalmers Fuel Cell Tractor) and 1966 (GM Electrovan), such power generators were considered for a long time to have no advantage over conventional combustion engines. However, during 1990s the interest in hydrogen fuel cells has grown dramatically. Several car companies began to seriously work on developing hydrogen-based fuel cells for mobile applications. At that time, the main motivation for hydrogen-based technologies was the reduction of CO_2 emission. Today, not only this target, but also a reduced dependence on crude oil has become a motivation for the development of hydrogen power for mobile and stationary applications.

The production of hydrogen does not exhibit significant problems, as there are many efficient methods to obtain this element. However, there is a major problem for using hydrogen as a fuel based on the lack of its efficient storage methods. Also recyclable (un)loading and recharging of the host remain problematic. Therefore, significant technical improvements of hydrogen storage methods are necessary. This is not only a technological, but also a major challenge in materials science.

Several methods are currently under consideration, among them three principal options for on-board hydrogen storage can be mentioned. These, according to the 2007 status,[2] are:

- Compression of gaseous hydrogen at 35−70 MPa and ambient temperature;
- Liquefaction at 20−30 K, 0.5−1 MPa;
- Solid state adsorption by dissociative adsorption in metal hydrides[1,3,4] or by associative adsorption in porous nanostructures.[5–7]

Hybrid solutions of at least two of the above technologies are very attractive, as well.

The presently available systems, high-pressure or liquefied-hydrogen tanks, possess several disadvantages. Among them are low safety, large tank size, and an inconvenient range of used pressures and temperatures. A possible solution for this problem would be to store hydrogen in low-weight solids. H_2 can be stored in solids by two principal mechanisms: chemisorption of hydrogen atoms (e.g. as hydrides[1,8] or aminoboranes[9]) and physisorption of hydrogen molecules in nanoporous, e.g. carbon-based, materials.[10–12]

Physisorption exhibits several advantages over chemical adsorption of hydrogen, for example complete reversibility and fast kinetics. In addition, a very small amount of interaction energy (10 kJ mol^{-1}) is involved, both in the H_2 up- and unloading process. Although hydrides, e.g. $NaAlH_4$ or $LiBH_4$, are able to reach the 2010 goal of the US Department of Energy (DOE) for hydrogen (6 wt% of stored H_2 and 45 g l^{-1} volumetric density),[13] the high temperature needed for desorption, the general stability of hydrides, and high costs remain obstacles.

In contrast to most hydride storage media, materials physisorbing H_2 offer reversible (un)loading processes without the need of intensive external heating. As H_2 is a neutral molecule with a small polarizability, the two main contributions to the physical adsorption energy are weak London (dispersion) interactions and electrostatic interactions with a dipole in the H_2

molecule induced by the polarity of the host system. The dispersion interaction depends on the polarizability of H_2 and the host material, and on the distance between them.

Well-designed materials with a large surface area, high polarizability, high density of hydrogen per volume and per mass of the host are suggested to have reasonable storage capacities. Other factors are expected to affect the physisorption of hydrogen molecules, e.g. the size and shape of pores, the structure of a material or its surface termination.

The class of light and porous carbon materials may satisfy the above mentioned conditions for good storage media. They exhibit low mass densities, extensive pore structures and good chemical stabilities. A great variety of structural carbon forms is already well known in the literature, e.g. graphite, diamond, activated carbons, nanofibres, single- and multi-walled nanotubes, nanohorns, carbynes, fullerenes, etc. The hydrogen storage capacities have already been discussed for many of these materials on the basis of experiment and theory. However, the largest interest is paid to graphitic (sp^2) carbon structures (activated carbon,[5,14] graphene slit pores,[6,15] carbon nanotubes,[7,16,17] fullerenes[18,19]). The reported H_2 uptakes of these materials were discussed in the literature not without controversy, based on both, experimental and theoretical results (e.g. Reference [20]).

Graphite (with sp^2 hybridization) is one of the four ordered carbon allotropes, beside diamond (sp^3), fullerenes (perturbed sp^2), and carbynes (sp^1). It has a layered structure with an interlayer distance, d, of 3.354 Å, in which the planes are weakly bound via van der Waals forces. This distance is, however, too small for the free penetration of hydrogen molecules with a dynamic diameter of approximately 4 Å.[21] In addition, the specific surface area of bulked graphite is very low and therefore hydrogen uptake can not be observed.[22]

The ability to trap H_2 by slit-pore cavities is strongly determined by the pore size (e.g. interlayer distance between the graphite layers).[12,22] It was recently shown that the smaller pores ($d = 6 - 8$ Å) provide the highest capacity and large pores contribute only marginally to the storage capacity.[12] Small pores, moreover, exhibit a larger specific surface area for a given pore volume.[23] At distances smaller than 5 Å the interaction of hydrogen with graphenes is repulsive and no H_2 can penetrate freely in between the layers.[24] For a larger d ($>$20 Å), the capability of a pore to store H_2 reduces continuously.[12,15] Thus, a good storage material should have a pore size distribution in the range of 5−10 Å.[12,22,25]

Increasing the interlayer distance of graphite to desired ∼6 Å requires ∼75 meV per carbon.[24] The penetration of H_2 into a graphite material is, thus, an endothermic process that needs at least 320 meV per hydrogen molecule. Thus, the distance between the planes of graphite should be enlarged, in order to increase the storage capability.

Carbon nanotubes can be considered as rolled graphene sheets with a well-defined curvature. From the geometric point of view, such curved cavities are favored for gas adsorption. The potential from opposite walls inside the cavity will overlap so that the attractive forces are increased compared to those on a flat graphene surface.[26] Due to the van der Waals forces these tubes tend to form bundles in a hexagonal close-packed lattice. Here, the adsorption can occur not only inside the cavity but also on the outer surface, at the grooves and in channels between neighboring tubes. There is, however, a wide discrepancy in the experimental H_2 uptake for carbon nanotubes. The storage capacities vary in a range from around 0.1% [27] to 11% [28] by weight, depending on the purity of the samples and the used range of temperatures and pressures. In addition, various experimentally obtained high storage capacities have not yet been reproduced, neither in other experiments nor on the basis of theory.

So far, the highest reliable storage capacity was observed for superactivated carbon.[29] This material is a carbon modification that contains very small graphite crystallites and amorphous carbon. The pore diameter is usually less than 1 nm and the specific surface area is up to 3000 m^2g^{-1}. Similarly to nanotubes, there is a strong overlapping of the potential fields of the different pore wall sides. These properties make activated carbon an excellent candidate for hydrogen storage, but due to a wide pore-size distribution only a fraction of the pores is able to exhibit the favorable overlap.

The above mentioned nanomaterials can produce high packing densities of hydrogen, but these are still not high enough to satisfy the target of DOE. Its 2010 goal has not yet been reached with any of the investigated materials for moderate pressures and ambient temperature.[30,31] Moreover, the systematic engineering and identification of specific adsorption sites in carbon nanostructures is difficult. Beside graphite, diamond and solid C_{60}, carbon allotropes do not have well defined periodic structures.

Efficient H_2 storage could also be improved by other purposes. The well-defined crystal structure, with easily controlled pore sizes might be a perfect solution. Also the introduction of attractive electrostatic interactions, e.g. a strong surface polarization, can improve the storage capability of a material. The adsorbed H_2 molecules can, therefore, be polarized increasing the guest-host interaction.

One of the most interesting materials with these properties are metal-organic frameworks[32,33] (MOFs), a family of nanoporous materials that are assembled by the connection of metal oxide centers (so-called inorganic connectors) through molecular bridges (so-called organic linkers). They were synthesized for the first time by Yaghi et al.[34] in 1999. By varying the size of the organic bridges the defined void regions can be controlled. As it is possible to tailor their chemical composition and pore-size distribution, many potential applications have been proposed for MOFs, among them H_2 storage.[35–37]

A wide range of porous MOFs has been synthesized[35,38–40] so far. They differ from porous carbon structures by their systematic design strategies based on self-assembling.[41] Different organic linkers can be used to narrow the channels connecting the nanopores. This makes the hydrogen desorption more difficult and better materials can be optimized for practical storage at ambient conditions. Catenation of networks also narrows the channels and produces smaller pores. This effect increases the number of corners and edges and, by extend, the number of adsorption sites.[42,43] Two types of catenation can take place, interweaving (minimal displacement between networks) and interpenetration (maximal displacement). The research of the gas storage in MOFs is still in an early phase, as these compounds are fairly new.

The present work is focused on the currently active research area of searching for porous materials, which are suitable to store hydrogen by gas adsorption techniques. The key factor is to design light-weight storage systems with a large specific surface area, a controlled pore-size distribution, and a strong surface polarization. Among the studied systems, the attention is paid to graphite-based nanostructures with enlarged interlayer distance. Thus, in the present work more advanced materials (Chapter 3), C_{60} intercalated graphite,[44] honeycomb graphite,[45,46] and defected graphite,[47] are proposed. Moreover, metal-organic frameworks (Chapter 4) are studied in order to investigate the influence of organic linkers on the properties of these materials. The nature of the interactions between H_2 and MOFs is also of great interest and, therefore, was set as one of the goals of this thesis. The interaction of H_2 with carbon materials has been already well understood.[48–51]

This work is organized as follows: In Chapter 3.1 carbon foams are discussed as slit-pore materials with functionalized graphene sheets. This chapter also shows properties of defected graphite, in which the interlayer distance was enlarged by dislocations. The example of graphite structures intercalated by spacer molecules is discussed in Chapter 3.2. The role of organic bridges and the properties of metal-organic frameworks are presented in Chapters 4.1 and 4.2. Chapter 4.3 is focused on interactions between molecular hydrogen and MOFs. Finally, the main conclusions and an outlook are given in Chapter 5.

Chapter 2

METHODOLOGY

In this chapter the fundamentals of quantum-mechanical calculations employed in present work will be discussed. In Section 2.1 the basic approaches of quantum chemistry and the principle approximations are explained. The computational methods and main theories used in the present work, second order Møller-Plesset (MP2) perturbation theory, Density Functional Theory (DFT) and Density Functional based Tight-Binding (DFTB), are presented in Sections 2.2, 2.3 and 2.4, respectively.

2.1 Theoretical Background

2.1.1 The Schrödinger Equation

In theoretical chemistry investigations are employed to predict and/or to explain experimental results by describing the electronic structure of systems that contain nuclei and electrons. The goal is to solve the Schrödinger equation for a large number of atoms accurately and efficiently. The Schrödinger equation written as:

$$\hat{H}\Psi = E\Psi \tag{2.1}$$

is time-independent and non-relativistic. Here, $\hat{H}$ is the Hamilton operator, Ψ is the total wavefunction of the system and E is the energy. The complete Hamiltonian of a many body system with M nuclei and N electrons includes nuclear (T_n) and electronic (T_e) kinetic energy operators, and the potential energies of the electrostatic interactions between charged particles, V_{e-e}, V_{n-n}, and V_{e-n}:

$$\begin{aligned}\hat{H} &= T_n + T_e + V_{e-e} + V_{n-n} + V_{e-n} \\ &= -\frac{1}{2}\sum_{\alpha=1}^{M}\nabla_\alpha^2 - \frac{1}{2}\sum_{\mu=1}^{N}\nabla_\mu^2 \\ &+ \sum_{\mu=1}^{N}\sum_{\nu,\mu\neq\nu}^{N}\frac{1}{r_{\mu\nu}} + \sum_{\alpha=1}^{M}\sum_{\beta,\alpha\neq\beta}^{M}\frac{Z_\alpha Z_\beta}{R_{\alpha\beta}} - \sum_{\mu=1}^{N}\sum_{\alpha=1}^{M}\frac{Z_\alpha}{r_{\mu\alpha}},\end{aligned} \tag{2.2}$$

where Z_α and Z_β are the charges of the nuclei, $r_{\mu\nu} = |\vec{r}_\mu - \vec{r}_\nu|$, $R_{\alpha\beta} = |\vec{R}_\alpha - \vec{R}_\beta|$, and $r_{\mu\alpha} = |\vec{r}_\mu - \vec{R}_\alpha|$ with r-electronic and R-nuclear spatial coordinates. Unfortunately, the Schrödinger equation is analytically solvable only for very simple cases, e.g. a hydrogen atom or one-electron positive ions. Nevertheless, there is a way to systematically approach the wave function of the ground state, the state that delivers the lowest energy. This is the so-called variational principle, which is the foundation for nearly all the approximate methods in quantum chemistry. According to this principle for a quantum molecular system an approximate wavefunction, when substituted into the Schrödinger equation, will always yield a higher energy than the actual ground state energy E_0 of the system.

$$\langle \Psi_{trial} | \hat{H} | \Psi_{trial} \rangle = E_{trial} \geq E_0 = \langle \Psi_0 | \hat{H} | \Psi_0 \rangle, \tag{2.3}$$

where the equality holds if and only if Ψ_{trial} is identical to Ψ_0. The variational principle allows to approximate the wavefunction, Ψ. It also shows how to evaluate the quality of a given approximate Ψ and how can it be improved. The calculated energy will be closer to the true energy if the chosen wavefunction is more precise.

2.1.2 Born-Oppenheimer Approximation

The aim of quantum mechanical calculations is to solve the Schrödinger equation for structures with many electrons and nuclei. In order to treat the many-body problem efficiently a number of approximations must be considered.

Quantum chemical methods are mainly based on the so-called Born-Oppenheimer approximation, which assumes that the nuclear and the electron motion can be separated entirely. The wavefunction $\Psi(\vec{r}, \vec{R}) = \Psi_e(\vec{r}) \cdot \Psi_n(\vec{R})$. As the masses of the nuclei are much larger (about three orders of magnitude) than those of the electrons, the electrons move much faster than the nuclei. Thus, the nuclei can be considered as stationary and the electrons are, therefore, moving in a potential of fixed nuclear sites. This assumption, introduced by Born and Oppenheimer,[52] leads to a zero kinetic energy of the nuclei (T_n) and the constant potential energy due to the nucleus-nucleus repulsion (V_{n-n}). Therefore, the Hamiltonian is reduced to its pure electronic component only:

$$\begin{aligned}\hat{H}_e &= T_e + V_{e-e} + V_{e-n} \\ &= -\frac{1}{2}\sum_{\mu=1}^{N}\nabla_\mu^2 + \sum_{\mu=1}^{N}\sum_{\nu,\mu\neq\nu}^{N}\frac{1}{r_{\mu\nu}} - \sum_{\mu=1}^{N}\sum_{\alpha=1}^{M}\frac{Z_\alpha}{r_{\mu\alpha}}\end{aligned} \tag{2.4}$$

and the electronic Schrödinger equation can be written as:

$$\hat{H}_e\Psi_e(\vec{r}) = E_e\Psi_e(\vec{r}). \tag{2.5}$$

$\Psi_e(\vec{r})$ depends directly on the electronic coordinates and parametrically on the nuclear coordinates. Thus,

$$[T_e + V_{e-e} + V_{e-n}]\Psi_e(\vec{r}) = E_e\Psi_e(\vec{r}) \tag{2.6}$$

for constant $(\vec{R})$. This wave function will change when the nuclei are moved. The total energy is obtained from E_e by adding the electrostatic energy due to the interaction between nuclei.

2.1.3 Hartree-Fock Method

Hartree-Fock (HF) is one of the simplest *ab initio* ('from the beginning' in Latin) methods. It is a variational method and the calculated energies are greater than the exact energy.

HF uses the wavefunction as the fundamental variable. The N-electron wavefunction is represented as a Slater determinant, Φ_{SD}, as an anti-symmetrized product of single-particle wavefunctions.

$$\Phi_{\mathrm{SD}} = \frac{1}{\sqrt{N!}}det|\phi_1(\vec{x_1})\phi_2(\vec{x_2})\ldots\phi_N(\vec{x_N})|. \tag{2.7}$$

This determinant ensures the obedience of the Pauli principle. The electrons with the same spin are kept away from each other. This defines the exchange principle.

One of the advantages of the HF method is that it breaks the many-electron Schrödinger equation into many simpler one-electron equations. Each of those is solved to yield a single-electron wave function (ϕ_μ; a spin orbital) and an energy. The orbital describes the behavior of an electron in the net field of all the other electrons. The Hartree-Fock equation can be written as follows:

$$\hat{F}_\mu \phi_\mu = \varepsilon_\mu \phi_\mu, \qquad \mu = 1, 2, 3, \ldots, N, \tag{2.8}$$

where ε_μ are the eigenvalues (orbital energies) of the Fock effective one-electron operator $\hat{F}_\mu$. This is a traditional so-called eigenvalue problem. The Fock operator has a following form:

$$\hat{F}_\mu = -\frac{1}{2}\nabla_\mu^2 - \sum_\alpha \frac{Z_\alpha}{r_{\mu\alpha}} + \hat{V}_{\mathrm{HF}}. \tag{2.9}$$

The first term is the kinetic energy, the second stands for the potential energy due to the electron-nucleus attraction, and $\hat{V}_{\mathrm{HF}}$ is the Hartree-Fock potential:

$$\hat{V}_{\mathrm{HF}} = \sum_\mu (\hat{J}_\mu - \hat{K}_\mu), \tag{2.10}$$

where $\hat{J}_\mu$ and $\hat{K}_\mu$ are the so-called Coulomb and exchange operators respectively:

$$\hat{J}_\mu \phi_k(\vec{x}_1) = \int \frac{|\phi_\mu(\vec{x}_2)|^2}{|\vec{r}_2 - \vec{r}_1|} d\vec{x}_2 \phi_k(\vec{x}_1), \tag{2.11}$$

$$\hat{K}_\mu \phi_k(\vec{x}_1) = \int \frac{\phi_\mu^*(\vec{x}_2)\hat{P}_{12}[\phi_\mu(\vec{x}_2)\phi_k(\vec{x}_1)]}{|\vec{r}_2 - \vec{r}_1|} d\vec{x}_2. \tag{2.12}$$

$\hat{P}_{12}$ is the permutation operator. The repulsion between electrons is replaced by the interaction of each electron with the averaged electrostatic field of other electrons and nuclei. Thus, the two-electron repulsion operator $\frac{1}{r_{\mu\nu}}$ in the Hamiltonian is replaced by the operator $\hat{V}_{\mathrm{HF}}$. Equation 2.8 is one for single particles and not for all N particles. The Fock operator is complicated in the sens that it depends on the solutions of the $\hat{J}_\mu$ and $\hat{K}_\mu$ operators, which themselves depend on the orbital ϕ_μ.

In HF the probability of finding an electron at some location around an atom depends on the distance from the nucleus. It does not, however, depend on the distance to the other electrons (the overestimation of the electron repulsion). In this way the electron correlation is neglected. This is not physically true and comes from the mean field treatment of electron-electron interactions. Thus, HF fails to describe e.g. London dispersion interactions, however, it accounts correctly for the electrostatic interactions and the Pauli repulsion.

Correlation effects (the differences between the single- and many-determinant wavefunction) are very important, as they improve the accuracy of computed energies and molecular geometries. There are several types of calculations that require the correlation effects, e.g. transition metals or weakly interacting systems. Many methods begin the calculations using the HF method and then correct for the correlation, e.g. Møller-Plesset perturbation theory (MPn, n-order of correction), configuration interaction (CI), or coupled cluster theory (CC).

2.1.4 Pseudopotentials

Electrons in a system can be divided into core and valence electrons. Unlike the chemically mostly inert core electrons, the valence ones form chemical bonds and govern the properties of the material. Thus, the core electrons can be combined with the potential of the nuclei to form a so-called pseudopotential. The pseudopotentials reproduce the exact all-electron wavefunction at a distance from the nucleus that is greater than a cut-off radius. This is chosen to be around halfway between the most outer node and most outer extremum of the wavefunction. The pseudopotential replaces the core wavefunction by a smooth nodeless function which is easy to represent numerically. Thus, the pseudo-wavefunctions are equal to the true wavefunctions outside of the core region. The larger the chosen radius, the faster a calculation is, but a lower accuracy is reached. Reducing the radius results in a better accuracy of the potential.

Readers with a deeper interest in quantum chemistry are referred to References [53–55] for more details.

2.2 Møller-Plesset Perturbation Theory

Hartree-Fock method often provides a good description of a system. However, in some case correlation effects, that are neglected in HF, play an important role. The correlation effects can be considered as a small perturbation and treated using the perturbation theory, e.g. Møller-Plesset (MP) perturbation theory.[56] MP theory of n-th order (MPn) uses the HF wavefunction as the unperturbed wavefunction.

The effective one-electron Fock operator $\hat{F}$ is given in Equation 2.8. The unperturbed Hamiltonian is chosen as a sum of those operators:

$$\hat{H}^0 = \sum_{\mu=1}^{N} \hat{F}(\mu). \tag{2.13}$$

The zero-th order eigenfunction for the ground state is the HF solution given as the Slater determinant:

$$\Psi_{\mathrm{HF}} = \Psi_0^{(0)} = \frac{1}{\sqrt{N!}} det|\phi_1(\vec{x_1})\phi_2(\vec{x_2})\ldots\phi_N(\vec{x_N})|. \tag{2.14}$$

Ψ_{HF} contains the N electrons in the spin-orbitals of the lowest energy and it is an eigenfunction of $\hat{H}^0$:

$$\hat{H}^0\Psi_{\mathrm{HF}} = \sum_{\mu=1}^{N} \hat{F}(\mu)\Psi_{\mathrm{HF}} = \sum_{\mu=1}^{N} \varepsilon_\mu \Psi_{\mathrm{HF}} \tag{2.15}$$

Equivalently:

$$E_0^{(0)} =< \Psi_0^{(0)}|\hat{H}^0|\Psi_0^{(0)} >=< \Psi_{\mathrm{HF}}|\sum_{\mu=1}^{N} \hat{F}(\mu)|\Psi_{\mathrm{HF}} >= \sum_{\mu=1}^{N} \varepsilon_\mu. \tag{2.16}$$

All the other eigenfunctions of $\hat{H}^0$ can be formed by permuting the N electrons among the M spin-orbitals. Thus, all the possible excited-state determinants are formed. The Slater determinant for a singly-excited state, Ψ_i^a, is the eigenfunction of $\hat{H}^0$ with eigenvalue $\sum \varepsilon_\mu - \varepsilon_i + \varepsilon_a$. For doubly-excited state, Ψ_{ij}^{ab}, this determinant will be an eigenfunction of $\hat{H}^0$ with eigenvalue $\sum \varepsilon_\mu - \varepsilon_i - \varepsilon_j + \varepsilon_a + \varepsilon_b$, etc.

In order to apply perturbation theory the electronic Hamilton operator takes a form:

$$\hat{H} = \hat{H}^0 + \Delta\hat{H}, \tag{2.17}$$

where $\hat{H}^0$ is an unperturbed Hamiltonian and $\Delta\hat{H}$ is a perturbation. Thus

$$\Delta\hat{H} = \hat{H} + \sum_{\mu=1}^{N} \varepsilon_\mu. \tag{2.18}$$

The zero-th order wavefunction is the HF wavefunction, $\Psi_0^{(0)} = \Psi_{\text{HF}}$ and the zero-th order energy is given as:

$$E_0^{(0)} = \sum_{\mu=1}^{N} \varepsilon_\mu \tag{2.19}$$

for the occupied spin orbitals.

The first-order perturbation to the ground state energy is:

$$\begin{aligned} E_0^{(1)} &= \langle \Psi_0^{(0)} | \Delta \hat{H} | \Psi_0^{(0)} \rangle \\ &= \langle \Psi_0^{(0)} | \hat{H} - \sum_{\mu=1}^{N} \hat{F}(\mu) | \Psi_0^{(0)} \rangle \\ &= \langle \Psi_0^{(0)} | \hat{H} | \Psi_0^{(0)} \rangle - \langle \Psi_0^{(0)} | \sum_{\mu=1}^{N} \hat{F}(\mu) | \Psi_0^{(0)} \rangle \end{aligned} \tag{2.20}$$

with $\Psi_0^{(0)} = \Psi_{\text{HF}}$. The first-order corrected ground state energy is then given as:

$$\begin{aligned} E_0 &= E_0^{(0)} + E_0^{(1)} \\ &= \langle \Psi_{\text{HF}} | \sum_{\mu=1}^{N} \hat{F}(\mu) | \Psi_{\text{HF}} \rangle + \langle \Psi_{\text{HF}} | \hat{H} | \Psi_{\text{HF}} \rangle - \langle \Psi_{\text{HF}} | \sum_{\mu=1}^{N} \hat{F}(\mu) | \Psi_{\text{HF}} \rangle \\ &= \langle \Psi_{\text{HF}} | \hat{H} | \Psi_{\text{HF}} \rangle = E_{\text{HF}}. \end{aligned} \tag{2.21}$$

Thus, the HF energy is the energy for the ground state corrected through a first-order in the MP expansion series.

To improve the HF energy the second-order correction must be evaluated (MP2). The second-order correction to the ground state depends on the first-order correction to the wavefunction. This depends on the matrix elements of the perturbation between the unperturbed ground state and excited states (m) of $\hat{H}^0$. The matrix elements $\langle \Psi_{\text{HF}} | \Delta \hat{H} | \Psi_{\text{m}}^{(0)} \rangle$ are identically zero, when $\Psi_{\text{m}}^{(0)}$ is a singly excited configuration. The triple and higher excitations give also zero matrix elements with $\Psi_{\text{HF}}^{(0)}$. The only contributions appear when $\Psi_{\text{m}}^{(0)}$ is a doubly excited configuration relative to $\Psi_{\text{HF}}^{(0)}$, and thus it can be written:

$$E_0^{(2)} = \sum_{i,j}^{N} \sum_{a,b}^{N_v} \frac{| < \Psi_{\text{HF}} | \Delta \hat{H} | \Psi_{ij}^{(ab)} > |^2}{\varepsilon_i + \varepsilon_j - \varepsilon_a - \varepsilon_b}, \tag{2.22}$$

where

$$E_{ij}^{(ab)} = E_0^{(0)} - \varepsilon_i - \varepsilon_j + \varepsilon_a + \varepsilon_b \tag{2.23}$$

i, j denote the occupied and a, b the unoccupied molecular orbitals, the ε_x are the corresponding energies, and $E_{ij}^{(ab)}$ is the energy of the doubly excited determinant $\Psi_{ij}^{(ab)}$.

The MP2 calculations include the calculation of the HF energy and the evaluation of the sum for the second-order energy correction by using the HF molecular orbitals and orbital energies. The third- (MP3) and fourth-order (MP4) calculations are also common, however, are more expensive and time consuming. Møller-Plesset calculations are not variational but they are size extensive.

2.3 Density Functional Theory

Density Functional Theory (DFT)[53,54,57] determines the energy of a system by using the electron density instead of the many-electron wavefunction. The origin of DFT comes from the theorems of Hohenberg and Kohn:[58] The first theorem says that it is possible to calculate the energy of a system in its ground-state using only the electron density $\rho(\vec{r})$:

$$\rho(\vec{r}) = N \int \Psi_0^*(\vec{r}, \vec{r_2}, \ldots, \vec{r_N})\ \Psi_0(\vec{r}, \vec{r_2}, \ldots, \vec{r_N})\ d\vec{r_2} \ldots d\vec{r_N}. \tag{2.24}$$

Especially the ground-state energy is solely determined by $\rho(\vec{r})$:

$$E = E[\rho(\vec{r})]. \tag{2.25}$$

The total number of electrons (N) is also defined by $\rho(\vec{r})$:

$$N = \int \rho(\vec{r})\ d\vec{r}. \tag{2.26}$$

No exact functional has been derived yet for most properties, although some good approximations exist. The second Hohenberg-Kohn theorem says that once the functional with the total electronic energy is known, one can calculate it approximately by inserting approximate densities $\rho'(\vec{r})$. Similarly to the variational principle for the wavefunction, one can improve the calculation by minimizing $E\rho'(\vec{r})$:

$$E[\rho'(\vec{r})] \geq E[\rho(\vec{r})]. \tag{2.27}$$

The practical scheme for calculating the ground-state properties from electron density was provided by Kohn and Sham in 1965.[59] They have proposed a set of self-consistent equations, so-called Kohn-Sham (KS) equations, in order to solve the many-body problem:

$$\left[-\frac{1}{2}\nabla^2 + V_{\text{ext}}(\vec{r}) + \int \frac{\rho(\vec{r'})}{|\vec{r}-\vec{r'}|} d\vec{r} + V_{\text{xc}}(\vec{r})\right] \phi_\mu(\vec{r}) = \varepsilon_\mu \phi_\mu(\vec{r}), \tag{2.28}$$

$$\rho(\vec{r}) = \sum_{\mu=1}^{N} |\phi_\mu(\vec{r})|^2, \tag{2.29}$$

$$V_{\text{xc}}(\vec{r}) = \frac{\delta E_{\text{xc}}[\rho(\vec{r})]}{\delta\rho(\vec{r})}. \tag{2.30}$$

The KS equations are single-particle equations similar to the HF method. The first term in Equation 2.28 stands for the kinetic energy, the second (V_{ext}) is the electron-nucleus attraction, and the third is the so-called Hartree potential, V_{H}. V_{xc} is the exchange-correlation potential. In this approach the electron-electron interaction is formulated in a mean field approach. The three potentials, V_{ext}, V_{H} and V_{xc}, are summarized to the effective potential V_{eff}. Now, the ground-state energy of the electronic system can be written as:

$$E_e[\rho(\vec{r},s)] = \sum_{\mu}^{N} \varepsilon_\mu - \frac{1}{2}\iint \frac{\rho(\vec{r})\rho(\vec{r'})}{|\vec{r}-\vec{r'}|}\, d\vec{r}d\vec{r'} + E_{\text{xc}} - \int \rho(\vec{r})\; V_{\text{xc}}[\rho(\vec{r},s)]\; d\vec{r}. \tag{2.31}$$

The KS equations can be solved only iteratively and self-consistently. At first, the electron density is guessed. The obtained potential is then used to determine the new $\rho(\vec{r})$, which again is inserted into the KS equations, etc. In order to give an expression for the exchange-correlation potential further approximations are needed. The well-known approximations are the Local Density Approximation (LDA)[60,61] and the Generalized Gradient Approximation (GGA).[62]

In the LDA E_{xc} is calculated using the expressions for the exchange-correlation energy of an homogeneous electron gas with the same $\rho(\vec{r})$:

$$E_{\mathrm{xc}}^{\mathrm{LDA}}[\rho(\vec{r})] = \int \rho(\vec{r}) \left[\varepsilon_{\mathrm{x}}^{\mathrm{hom}}[\rho(\vec{r})] + \varepsilon_{\mathrm{c}}^{\mathrm{hom}}[\rho(\vec{r})] \right] d\vec{r}, \tag{2.32}$$

where $\varepsilon_{\mathrm{x}}^{\mathrm{hom}}$ and $\varepsilon_{\mathrm{c}}^{\mathrm{hom}}$ are the exchange and the correlation energies per electron of an homogeneous electron gas of density $\rho(\vec{r})$.

In case of more or less homogeneous densities LDA will give high-accuracy results. However, in many real systems the electron density is not uniform and varies spatially. Usually, the LDA overestimates the binding energies and underestimates the band-gap energies.

A better account for the non-uniform electron density in real systems can be achieved within the GGA. The exchange correlation energy in the GGA includes terms that depend not only on the electron density but also on its spatial derivatives.

$$E_{\mathrm{xc}}^{\mathrm{GGA}}[\rho(\vec{r})] = \int \rho(\vec{r})\; \varepsilon_{\mathrm{x}}^{\mathrm{hom}}[\rho(\vec{r})]\; F_{\mathrm{xc}}[\rho(\vec{r}), |\nabla\rho(\vec{r})|, \ldots]\; d\vec{r}, \tag{2.33}$$

where F_{xc} is dimensionless and $\nabla\rho(\vec{r})$ is the gradient of the electron density. The GGA gives more precise binding and atomization energies.

It must be kept in mind, that DFT is a ground-state theory and may fail in excited state description. It should also be noted that the LDA and GGA approaches fail in describing the long-range interactions.

2.3.1 Basis Sets

The HF approach approximates the N-electron wavefunction (Ψ_e) with a single Slater determinant (Φ_{SD}) of N single-electron orbitals (ϕ_μ). The HF equation should be solved in order to determine ϕ_μ and the single-particle energies ε_μ. In order to calculate any realistic system, Roothaan (1951) suggested the expansion of orbitals into a set of pre-defined basis functions, χ_k:

$$\phi_\mu(\vec{x}) = \sum_{k=1}^{N_b} \chi_k(\vec{x}) c_{k\mu}, \tag{2.34}$$

where the $c_{k\mu}$ are the expansion coefficients, ϕ_μ is the μ-th molecular orbital, χ_k is the k-th basis function, and N_b is the number of the basis functions.

Historically atomic orbitals were used as basis functions. Atomic orbitals (AOs) are solutions of the HF equations for the atom, i.e. a wave functions for a single electron in the atom. To represent χ_k one can choose:

$$\chi(\vec{r}) = R_{lm}(r)Y_{lm}(\Theta, \Phi), \tag{2.35}$$

assuming that χ belongs to an atom placed at the origin. Y_{lm} is a spherical harmonic function, R_{lm} is the radial part, and r, ϕ and Θ are the spherical coordinates with respect to the position of an atom.

The commonly used basis set functions are Slater or Gaussian type orbitals and plane waves. Slater-type orbitals (STOs) have exponential radial parts in the form $\mathrm{e}^{(-\zeta r)}$:

$$\chi(\vec{r}) = Nr^{n-1}e^{(-\zeta r)}Y_{lm}(\Theta, \Phi), \tag{2.36}$$

where N is the normalization constant and ζ is the orbital exponent. The largest problem of using STOs is that it is complicated to calculate the matrix elements entering the Fock matrix. The standard solution to this problem is to represent the STOs with Gaussian-type orbitals (GTOs), also called Gaussians. These have the form $\mathrm{e}^{(-\alpha r^2)}$ and they are located (placed) at the nuclei and sometimes also at bond centers:

$$\chi(\vec{r}) = Nx^n y^m z^o e^{(-\alpha r^2)}, \tag{2.37}$$

where α is the orbital exponent, m, n, o are integers and x, y, z are Cartesian coordinates. When $m + n + o = 0$, then $\chi(\vec{r})$ is said to be a s-type Gaussian function; when $m+n+o = 1$, then $\chi(\vec{r})$ is a p-type Gaussian; and when $m+n+o = 2$, then $\chi(\vec{r})$ is a d-type Gaussian. The advantage of using this type of functions is that the the matrix elements can be calculated rather efficiently. A single Gaussian function poorly describes atomic orbitals. To circumvent this problem one can use a larger number of Gaussians, in particular those with large α (short-ranged). In this way a more accurate description can be reached. More accurate results can also be obtained when the basis set is augmented with so-called polarization functions, as d functions on carbon atom or p functions on hydrogen atom.

A completely different approach is used with plane waves. They have the general form $\mathrm{e}^{i\vec{k}\cdot\vec{r}}$, where $\vec{r}$ is the position vector and $\vec{k}$ is the propagation vector. They can not be ascribed to individual atoms and so are independent of the atom positions. The basis set quality can be systematically improved by including additional plane waves until convergency of the energy. However, they require the use of periodic boundary conditions. The advantage of Gaussian orbitals over plane waves is that a smaller number of basis functions is required.

2.4 Density Functional based Tight-Binding

The Density Functional based Tight-Binding (DFTB)[63–67] method is based on an LCAO ansatz for the Kohn-Sham wavefunction. In this approximation, the KS orbitals $\Psi_i(\vec{r})$ of a system are expanded in terms of atomic-like basis functions, ϕ_μ, centered at atomic sites, $\vec{R_\alpha}$:

$$\Psi_i(\vec{r}) = \sum_{\mu=1}^{N} C_\mu^i \; \phi_\mu(\vec{r} - \vec{R_\alpha}), \tag{2.38}$$

solving the KS equation in an effective one-particle potential ($V_{\text{eff}}(\vec{r})$):

$$\hat{H}\Psi_i(\vec{r}) = \varepsilon_i \Psi_i(\vec{r}) \tag{2.39}$$

where

$$\hat{H} = -\frac{1}{2}\nabla^2 + V_{\text{eff}}(\vec{r}). \tag{2.40}$$

The atomic orbitals ϕ_μ are obtained by e.g. self-consistent LDA calculations of the neutral atom. Within the LCAO ansatz the KS equations are transformed in to a secular problem:

$$\sum_{\mu=1}^{N} C_\mu^i (H_{\mu\nu} - \varepsilon_i S_{\mu\nu}) = 0; \qquad \forall\; i, \mu. \tag{2.41}$$

where the matrix elements of the Hamiltonian $H_{\mu\nu}$ and the overlap matrix elements $S_{\mu\nu}$ are defined as follows:

$$H_{\mu\nu} \equiv \langle \phi_\mu | \hat{H} | \phi_\nu \rangle \qquad S_{\mu\nu} \equiv \langle \phi_\mu | \phi_\nu \rangle. \tag{2.42}$$

The effective KS potential $V_{\text{eff}}(\vec{r})$ is approximated as a superposition of potentials of the compressed pseudo-atoms $V_\alpha(\vec{r_\alpha})$:[63]

$$V_{\text{eff}}(\vec{r}) = \sum_\alpha V_\alpha(\vec{r_\alpha}) \qquad \vec{r_\alpha} = |\vec{r} - \vec{R_\alpha}|. \tag{2.43}$$

Equation 2.43 can be further approximated by neglecting the three-center contributions and all crystal-field terms. $V_\alpha(\vec{r_\alpha})$ are determined from the self-consistent calculations of compressed pseudo-atoms. The compression of an atom is achieved by introduction of an additional potential in the form $(r/r_0)^n$ [68] in the atomic self-consistent calculations. Thus, the functions in the bonding regions stay unchanged, but the long-range tails of the valence electron basis functions decay more rapidly.

This approximation for the potentials is consistent with an approximation in the matrix elements of the Hamiltonian, which states:

$$H_{\mu\nu} = \begin{cases} \varepsilon_\mu^{\text{free atom}} & \text{if } \mu = \nu \\ \langle \phi_\mu^\alpha \,|-\frac{1}{2}\nabla^2 + V_\alpha + V_\beta|\, \phi_\nu^\beta \rangle & \text{if } \mu \in \{\alpha\}, \nu \in \{\beta\}, \alpha \neq \beta \\ 0 & \text{otherwise} \end{cases} \tag{2.44}$$

α and β indicate the atom on which the wave functions and the potentials are centered. Only the two-center Hamiltonian matrix elements are considered, but all two-center terms ($H_{\mu\nu}$, $S_{\mu\nu}$) are calculated exactly. Due to the fact that all matrix elements depend only on interatomic distances, they can be calculated only once for each pair of atom types and stored.

The total energy using the KS eigenvalues can be written as:

$$\begin{aligned} E_{\text{tot}}[\rho(\vec{r})] = \sum_i^{\text{occ}} \varepsilon_i - \frac{1}{2}\left[\int V_{\text{eff}}\rho(\vec{r})\; d^3\vec{r} + \int V_{e-n}\rho(\vec{r})\; d^3\vec{r}\right] \\ + E_{\text{XC}} - \frac{1}{2}\int V_{\text{XC}}\rho(\vec{r})\; d^3\vec{r} + V_{n-n}. \end{aligned} \tag{2.45}$$

When the density and the potential are written as a superposition of atomic-like contributions, the total energy takes the following form:

$$\begin{aligned}E_{\text{tot}}[\rho(\vec{r})] = \sum_i^{\text{occ}} \varepsilon_i - \frac{1}{2}\sum_\alpha\sum_\beta \int V_\alpha \rho_\beta(\vec{r})\ d^3\vec{r} - \frac{1}{2}\sum_\alpha\sum_\beta \int \frac{Z_\alpha \rho_\beta(\vec{r})}{r_\alpha}\ d^3\vec{r} \\ + \frac{1}{2}\sum_\alpha \sum_{\beta,\alpha\geq\beta} \int V_{\text{XC}}[\rho_\alpha(\vec{r}), \rho_\beta(\vec{r})]\ d^3\vec{r} + \frac{1}{2}\sum_\alpha \sum_{\beta,\alpha\neq\beta} \frac{Z_\alpha Z_\beta}{R_{\alpha\beta}}\end{aligned} \tag{2.46}$$

with $R_{\alpha\beta} = |\vec{R_\alpha} - \vec{R_\beta}|$. Applying further approximation, all terms except the sum of the eigenvalues can be written as a repulsive potential V_{rep}:

$$\begin{aligned}\sum_{\alpha\neq\beta} V_{\text{rep}}(R_{\alpha\beta}) = -\frac{1}{2}\sum_{\alpha\beta} \int V_\alpha(\vec{r})\rho_\beta(\vec{r})\ d^3\vec{r} - \frac{1}{2}\sum_{\alpha\beta} Z_\alpha \int \frac{\rho_\beta(\vec{r})}{r_\alpha}\ d^3\vec{r} \\ + \frac{1}{2}\sum_{\alpha\geq\beta} \int \tilde{V}_{\text{XC}}[\rho_\alpha(\vec{r}), \rho_\beta(\vec{r})]\ d^3\vec{r} + \frac{1}{2}\sum_{\alpha\neq\beta} \frac{Z_\alpha Z_\beta}{R_{\alpha\beta}},\end{aligned} \tag{2.47}$$

what leads to the simple expression for E_{tot}:

$$E_{\text{tot}}[\rho(\vec{r})] = \sum_i^{\text{occ}} \varepsilon_i + \sum_{\alpha>\beta} V_{\text{rep}}(R_{\alpha\beta}). \tag{2.48}$$

V_{rep} is a short-range repulsive potential, derived from reference LDA or GGA calculations of proper molecular and crystalline systems for a range of typical bond lengths.

These approximations in DFTB method give good results for polar and covalently bound systems. For heteroatomic systems, where elements have similar electronegativities, the partial charge redistribution have to be considered. Elstner et al.[69] have developed a self-consistent charge (SCC) correction for DFTB in order to allow a more accurate description of such heteroatomic systems.

In SCC-DFTB the total energy is written in terms of a second-order Coulomb correction:

$$E_{\text{tot}} = \sum_i^{\text{occ}} \varepsilon_i + \frac{1}{2}\sum_{\alpha,\beta} \Delta q_\alpha \Delta q_\beta \gamma_{\alpha\beta}(R_{\alpha\beta}) + V_{\text{rep}}(\alpha, \beta, R_{\alpha\beta}), \tag{2.49}$$

where q_α denotes the charge centered at the atom α (Mulliken[70]):

$$\Delta q_\alpha = q_\alpha + Z_\alpha = \sum_{\mu\in\alpha}\sum_\nu C_{\mu i} C_{\nu i} S_{\mu\nu} + Z_\alpha. \tag{2.50}$$

In Equation 2.49, $\gamma_{\alpha\beta}$ is related to the Hubbard parameter ($U_\alpha \approx \gamma_{\alpha\alpha}$), which can be calculated from DFT as follows:

$$U_\alpha = \frac{\delta \varepsilon_{\mathrm{HOMO}}}{\delta n_{\mathrm{HOMO}}}. \tag{2.51}$$

Thus, the second-order Coulomb correction to the KS matrix element gives:

$$H_{\mu\nu} = H^{(0)}_{\mu\nu} + \frac{1}{2} S_{\mu\nu} \sum_{\gamma} \Delta q_\gamma (\gamma_{\alpha\gamma}(R_{\alpha\gamma}) + \gamma_{\beta\gamma}(R_{\beta\gamma})). \tag{2.52}$$

$H^{(0)}_{\mu\nu}$ is used from the stored list for each pair of atom types. Other terms are calculated self-consistently with charge-derived corrections. This gives more accurate results, however the computational time is considerably increased.

In conclusion, the DFTB method is less expensive and time consuming than the DFT, and therefore was used in present work to calculate the properties of carbon materials and metal-organic frameworks (Chapter 3 and Sections 4.1 and 4.2). In order to correctly describe weak interactions (London dispersion) between molecular hydrogen and building blocks of metal-organic frameworks (Sections 4.3) the MP2 method was employed, whereas the HF calculations were performed to evaluate the electrostatic interactions. The DFT calculations also were performed for comparison.

Chapter 3

CARBON STRUCTURES

Carbon forms several stable allotropes. At ambient conditions of pressure and temperature, the most stable crystalline carbon allotrope is hexagonal graphite, that consists of graphene layers with sp^2 hybridized carbon atoms. Diamond (sp^3 carbon atoms), the second stable allotrope of carbon, is at the same conditions nearly as stable as graphite.

The discovery of fullerenes[71] and nanotubes[72] opened a fast developing research field on new carbon forms and their properties. Among the carbon structures graphenes,[73] onions,[74,75] diamondoids,[76,77] peapods,[78] scrolls,[79] etc. have been found and many others were proposed. Parallel to experiments, this subject has attracted theoretical scientists.[77,80–84] In particular, a great interest has been paid to graphite-based materials. Carbon nanostructures with enlarged distances between the graphene layers have been suggested for possible applications in gas-storage technologies. However, it remains to be discussed how graphene layers with well-defined interlayer distances (d) and high stability can be produced.

Several possibilities, indeed, have been proposed in literature: They include functionalization of the graphene sheets, e.g. by fluorination,[85,86] by doping with lithium-complexes[87] or by oxidation with acid agents. This results in randomly spread out hydroxy and epoxy groups, which expand the interlayer distance.[88,89] The interlayer spacing of such functionalized graphite can range between 4.7 Å and 9 Å, and depends on the preparation and the temperature. As functionalization transforms sp^2 into sp^3 carbon atoms, it allows covalent interlayer bonds and imposes loss of planarity.[90] Such structures contain both sp^2 and sp^3 hybridization of carbon atoms but require introduction of heavier atoms (O, F, Li, etc.).

Functionalization of graphene layers is possible also in pure carbon materials. For example, in carbon foams some of the sp^2 carbon atoms are transformed into sp^3 carbon atoms, which allows diamond-like fragments to appear. Dislocations in graphite[47,91] may increase the d-spacing as well. In this case the graphene planarity is lost and the structures consist either of purely sp^2 or sp^2 and sp^3 hybridized atoms.

An alternative possibility to increase the interlayer distance, while leaving the graphene sheets intact, is the intercalation with spacer molecules. The intercalation is a destabilizing process, in which the interlayer van der Waals contacts are broken. Thermodynamically it is partially compensated by formation of the spacer-layer interactions. The intercalation of spacers into graphite is, however, possible, as it was reported in a recent experimental synthesis and characterization of C_{60} fullerenes intercalated graphite.[92]

In this chapter, the discussion will be focused on properties of graphite-based materials, whose interlayer distances were significantly enlarged. In Chapter 3.1 carbon foams and defected graphite are discussed. Furthermore, the structure of C_{60}-intercalated graphite is investigated in Chapter 3.2.

3.1 Carbon Foams

In addition to pure sp^2 or sp^3 crystals, several experimental and theoretical works focus on the properties of new possible carbon forms, namely those with co-existing sp^2 and sp^3 hybridization.[45,90,93–96] Among them diamond-graphite hybrids, vacancies in graphite or carbon foams are of great interest. The investigations include, e.g. the pressure-temperature phase transition of graphite into a cubic diamond structure.[97] It was shown that some of the new carbon forms, e.g. a super-hard carbon phase produced from C_{60} fullerenes which contains both types of hybridization, appeared to have hardnesses higher than that of the (100) and (111) diamond faces.[98–100]

In this section, single-wall carbon foams[46] are discussed [see Figure 3.1]. Due to the pattern of open edges, two types of such structures can be built, so-called armchair and zig-zag foams, in analogy to the nomenclature of carbon nanotubes. The pore size is defined by a pair of integer numbers (N,M), which indicate the number of hexagonal units between the junctions. The junctions consist of the sp^3 boundary-atom chains [cf. Figure 3.2]. The two numbers are necessary to distinguish between the possible symmetric carbon foams of size $N = M$ and asymmetric ones with $N \neq M$. This nomenclature will be use in the following. As these materials are highly porous, they were investigated in terms of possible applications in hydrogen storage.

In 1987, Vanvechten et al.[101] showed that dense packing of C_{11} clusters consisting of three five-fold rings in a condensed phase can result in a foam-like system. The structure of carbon foams was, however, proposed only later by Karfunkel et al.[45] and Balaban et al.[93] Recently, experimental[95,96,102] and

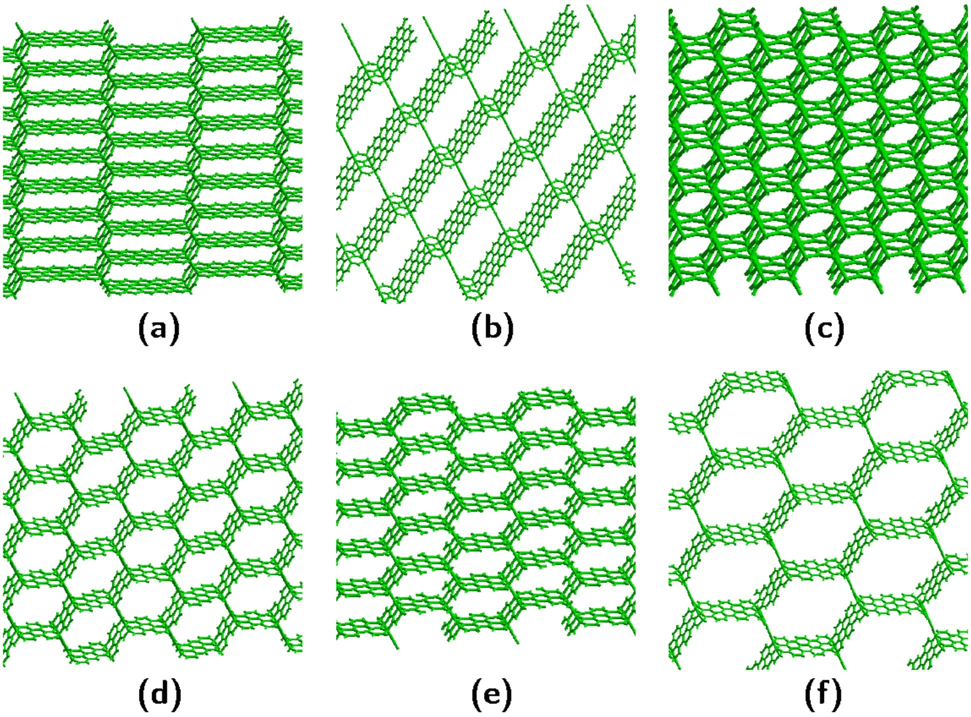

Figure 3.1: *Exemplary carbon foam structures; (a)-(c): (5,1), (1,5), (1,1) zig-zag carbon foams, respectively; (d)-(f): (3,3), (3,2), (5,5) armchair carbon foams, respectively (see text for the nomenclature).*

theoretical[94,103,104] investigations have shown that carbon-foam-like materials can be formed by rather simple syntheses. For example, the mesophase pitch precursor is molten at high temperatures resulting in so-called graphitic foams. Although these systems are no single-wall carbon foams, as they are discussed in this work, it is possible to achieve similar structures experimentally.

Single-wall carbon foams might be, however, formed by hierarchical self-assembly processes from layered graphite[21] or by a cold compression of carbon nanotubes.[102] The experiment of Wang et al.,[102] where a sample of carbon nanotubes has been coldly compressed in a diamond anvil cell, shows the transformation into what is believed to be a novel carbon allotrope. It was discussed on the basis of theoretical calculations[104] that the new form of carbon obtained by Wang et al.[102] can be described as a carbon foam structure.

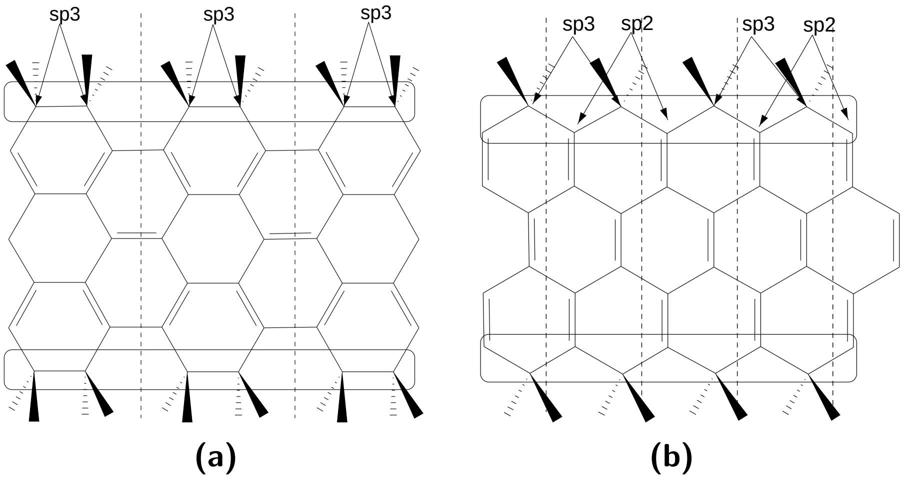

Figure 3.2: *The boundary atoms of zig-zag (a) and armchair (b) carbon foams. The unit cells are indicated by dashed lines.*

The results indicate that kinetically stabilized products, such as low-density carbon foam materials, may have possibly been formed in this experiment. It was also shown that the new crystalline carbon phase is a hard carbon phase with a high (calculated) bulk modulus.[104]

3.1.1 Computational Details

The systematic studies of the stability, electronic and mechanical properties of different carbon foams were performed using the DFTB method as it was discussed in Section 2.4. Periodic boundary conditions were used to calculate the infinite crystalline solid state.

The binding energies of the carbon foams can be considered as follows: The elementary cell consists of n_x carbon atoms at the boundaries (junctions) and n_i atoms inside the graphene fragments (stripes). Thus, the energy of a carbon foam can be written as

$$E_{\text{bind}} = n_i \varepsilon_\infty + n_x \varepsilon_x, \tag{3.1}$$

where ε_∞ is the binding energy of the infinite graphene layer, whereas ε_x describes the binding energy of the boundary atoms in the unit cell. Since

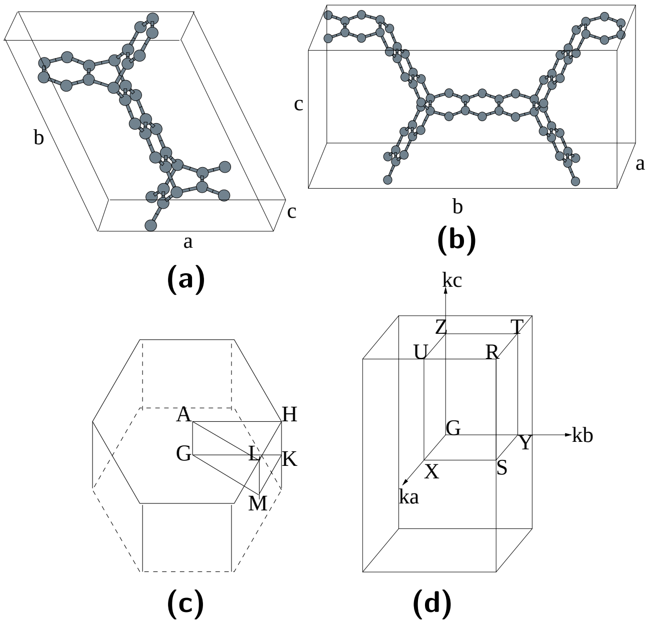

(a) (b) (c) (d)

Figure 3.3: *The hexagonal (a) and orthorhombic (b) elementary unit cells of the (3,3) zig-zag carbon foam and (c), (d) the respective Brillouin zones.*

the total number of atoms $n = n_i + n_x$, the energy can be expressed as follows:

$$E_{\text{bind}} = n\varepsilon_\infty - n_x\varepsilon_\infty + n_x\varepsilon_x, \tag{3.2}$$

Defining $\Delta\varepsilon = \varepsilon_x - \varepsilon_\infty$, the energy per atom becomes:

$$\frac{E_{\text{bind}}}{n} = \varepsilon_\infty + \frac{n_x\Delta\varepsilon}{n} \tag{3.3}$$

where the number of boundary atoms n_x per unit cell is hold constant at $n_x = 8$.

The conjugate-gradient scheme was chosen for the geometry optimization. The number of **k**-points was determined by reaching convergence for the total energy as a function of **k**-points according to the scheme proposed by Monkhorst and Pack.[105] Band structures were computed along lines between high symmetry points of the Brillouin zone. The first Brillouin zones with the highly symmetric points for hexagonal and orthorhombic unit cells [Figures 3.3 (a)−(b)] are shown in Figures 3.3 (c)−(d).

The mechanical properties were studied in detail by estimation of the bulk and shear moduli. The elastic constants (stiffness) c_{ij} were calculated using the finite-difference scheme (the derivatives of the total energy with strain $\varepsilon_{i,j}$) as:

$$\frac{\partial}{\partial \varepsilon_i} \cdot \left(\frac{\partial E}{\partial \varepsilon_j} \right) = c_{ij} \tag{3.4}$$

The matrix of constants was further used to obtain the bulk modulus

$$\mathbf{B} = \frac{1}{9} \left[c_{11} + c_{22} + c_{33} + 2 \left(c_{12} + c_{13} + c_{23} \right) \right] \tag{3.5}$$

for orthorhombic lattices or

$$\mathbf{B} = \frac{\Delta c_{33} + 2c_{13}}{\Delta + 2}, \tag{3.6}$$

for hexagonal unit cells, where

$$\Delta = \frac{c_{11} + c_{12} - 2c_{13}}{c_{33} - c_{13}}. \tag{3.7}$$

The shear modulus **G** can be calculated according to:

$$\mathbf{G} = \frac{1}{15} \left[\left(c_{11} + c_{22} + c_{33} - c_{12} - c_{13} - c_{23} \right) + 3 \left(c_{44} + c_{55} + c_{66} \right) \right] \tag{3.8}$$

3.1.2 Structure

Carbon foams are three-dimensional porous structures that contain both sp^2 and sp^3 hybridized atoms [see Figure 3.1]. They can be thought of as constructed from graphene planes interconnected rigidly with one another at 120°, forming a linear chain of sp^3 bonded atoms along the junction [see Figures 3.4]. At these junctions, always three graphene layers meet [c.f Figures 3.4 (c) and (f)] resulting in the honey-comb-shaped cross-section (CS) of the foam. If the graphitic segments are connected to each other at different angles than 120°, the systems with non-hexagonal CS are obtained. The present study was restricted to foams that contain only six-fold rings and hexagonal cross-sections.[46]

Carbon foams discussed here can also be considered as AA-stacked graphite structures with a significantly increased interlayer distance. Thus, N describes the length of graphene fragments linked together by M graphene

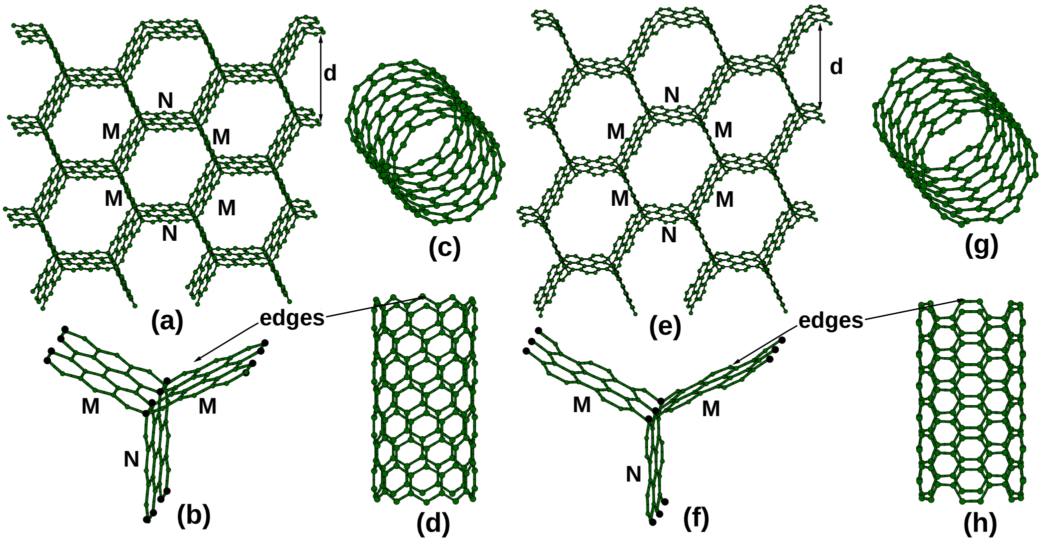

Figure 3.4: *(a) The structure of the (3,3) zig-zag carbon foam and (b) its bonding configuration at the junction in an orthorhombic lattice compared to the (10, 0) zig-zag carbon nanotube (c, d). (e) The structure of the (3,5) armchair carbon foam and (f) its bonding configuration at the junction in an orthorhombic lattice compared to the (5, 5) armchair carbon nanotube (g, h). Only three hexagonal units in a direction and two unit cells in b and c directions are shown for visual clarity. The black circles represent the linear chain of the sp^3 hybridized atoms.*

stripes. In other words, the N-stripes are functionalized by M-fragments. In this way, M determines the interlayer spacing as $d = \sqrt{3}M$. The ABAB-stacked forms are possible as well, as e.g. in the case of defected graphite (Section 3.1.6). The sp^2 carbon atoms, which are transformed into sp^3 atoms, make rigid interconnections between the graphene layers.

In Figure 3.4 (a) and (e) perspective views of the (3,3) zig-zag and the (3,5) armchair carbon foams are given, in comparison to the (10,0) zig-zag [Figures 3.4 (c), (d)] and (5,5) armchair [Figure 3.4 (g) and (h)] carbon nanotubes.

For a given pore size, the elementary unit cells of zig-zag and armchair carbon foams differ in the number of atoms (n). As an example, the (2,2) carbon foam consists of 44 and 20 carbon atoms for the zig-zag and the armchair foam, respectively. All structures can be represented in orthorhombic 3D carbon networks. Moreover, the zig-zag foams, with $N = M$, can be described within hexagonal lattices as well.

The interlayer distances d [Figure 3.4] vary in the range of 4.7 Å [(1,1) zig-zag foam] and 32.3 Å [(9,9) armchair foam]. The orthorhombic unit cell length in a direction can be as short as 2.46 Å and 4.27 Å for armchair and zig-zag carbon foams, respectively. The pore size is determined by the unit cell parameters b and c (see Figure 3.3 for definition). Keeping a at its minimum and reducing the width in the b and c directions to zero (N,M = 0), the structure reduces to a network of fourfold coordinated carbon atoms, namely that of cubic diamond (from armchair carbon foams) or hexagonal diamond (isodiamond; from zig-zag carbon foams).[93,106] On the other hand, increasing the system in a and b directions gives, in the $a, b \longrightarrow \infty$ limit, the structure of an isolated graphene layer.

The structures of zig-zag and armchair foams also differ in the types of connections (bonds): three types of covalent bonds, $sp^2{-}sp^2$, $sp^2{-}sp^3$, and $sp^3{-}sp^3$, can be found in the zig-zag arrangement (cf. Table 3.1), whereas armchair foams have two kinds of $sp^2{-}sp^2$ bonds (single and double; cf. Table 3.2) and $sp^2{-}sp^3$ bonds (there are no direct $sp^3{-}sp^3$ connections along the a axis). Comparing the geometries of carbon foams with the corresponding data for graphite and diamond (Table 3.1), one can find that the bond lengths are in between the values for both carbon allotropes. The $sp^3{-}sp^3$ bonds at the junctions are only slightly distorted from the ideal tetrahedral bonds in diamond. Moreover, the angles at the threefold and fourfold coordinated atoms are the same as those in graphite and diamond, respectively. The $sp^2{-}sp^2$ bond lengths in the zig-zag foams are very close to the bond lengths in graphite, whereas in armchair foams 'single' and 'double' bonds between sp^2 carbon atoms exist (cf. Table 3.2). The difference between 'single' and 'double' bonds decreases with increasing size, approaching the value of graphite.

Furthermore, the results indicate that the optimized unit cell sizes of carbon foams correspond to mass densities smaller than that of graphite (ρ = 2.27 g cm^{-3}) and diamond (ρ = 3.54 g cm^{-3}) [cf. Figure 3.5]. The only exception was found for the (1,1) zig-zag foam with a mass density of

Table 3.1: *The geometry parameters of the symmetric zig-zag carbon foams compared to the calculated and the experimental data for graphite and diamond (values in parenthesis).*

Structure	Bond length [Å]		Bond angle [°]	
graphite	sp^2-sp^2	1.420 (1.421)	$sp^2-sp^2-sp^2$	120.11 (120.00)
diamond	sp^3-sp^3	1.541 (1.545)	$sp^3-sp^3-sp^3$	109.47 (109.47)
(1,1)	sp^2-sp^2	1.359	$sp^2-sp^2-sp^2$	120.00
	sp^2-sp^3	1.536	$sp^3-sp^2-sp^3$	109.11
	sp^3-sp^3	1.557		
(2,2)	sp^2-sp^2	1.418	$sp^2-sp^2-sp^2$	120.00
	sp^2-sp^3	1.534	$sp^3-sp^2-sp^3$	109.16
	sp^3-sp^3	1.585		
(3,3)	sp^2-sp^2	1.420	$sp^2-sp^2-sp^2$	120.00
	sp^2-sp^3	1.530	$sp^3-sp^2-sp^3$	109.17
	sp^3-sp^3	1.567		
(4,4)	sp^2-sp^2	1.424	$sp^2-sp^2-sp^2$	120.00
	sp^2-sp^3	1.531	$sp^3-sp^2-sp^3$	109.16
	sp^3-sp^3	1.576		
(5,5)	sp^2-sp^2	1.425	$sp^2-sp^2-sp^2$	120.00
	sp^2-sp^3	1.532	$sp^3-sp^2-sp^3$	109.17
	sp^3-sp^3	1.575		

Table 3.2: *The geometry parameters of the symmetric armchair carbon foams.*

Structure	Bond length [Å]		Bond angle [°]	
(2,2)	sp^2-sp^2	1.352, 1.448	$sp^2-sp^2-sp^2$	120.87
	sp^2-sp^3	1.523	$sp^3-sp^2-sp^3$	110.46
(3,3)	sp^2-sp^2	1.372, 1.442	$sp^2-sp^2-sp^2$	120.63
	sp^2-sp^3	1.518	$sp^3-sp^2-sp^3$	110.07
(4,4)	sp^2-sp^2	1.384, 1.436	$sp^2-sp^2-sp^2$	120.41
	sp^2-sp^3	1.515	$sp^3-sp^2-sp^3$	109.23
(5,5)	sp^2-sp^2	1.394,1.443	$sp^2-sp^2-sp^2$	120.27
	sp^2-sp^3	1.515	$sp^3-sp^2-sp^3$	108.81

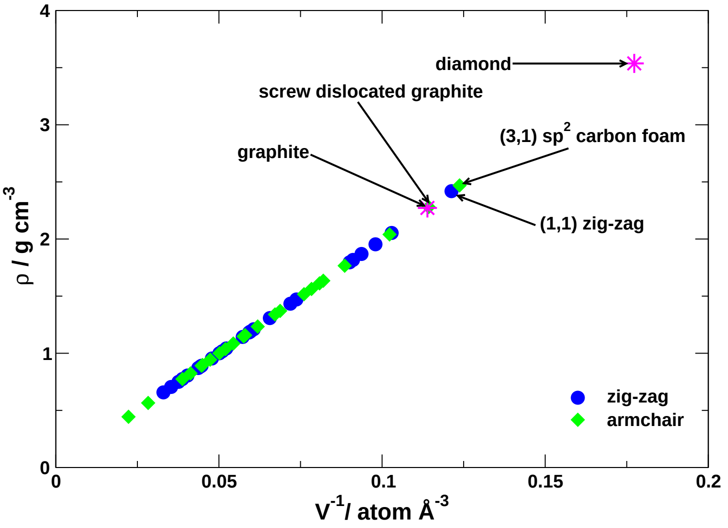

Figure 3.5: *The mass densities versus V^{-1} (V-the atomic volume) of carbon foams compared to graphite and diamond.*

$\rho = 2.42$ g cm^{-3}.

The smallest armchair foams (N,1) with an initial distance between the graphitic segments smaller than the van der Waals interlayer distance of graphite become very interesting systems after a full geometry optimization [Figure 3.6]. During the optimization, the sp^3 hybridized atoms of these structures open one of the four bonds and bind strongly to three neighbors only. This results in a porous system, built of sp^2 carbon atoms (in the following these forms are called 'sp^2 carbon foams'). To obtain such structures a larger unit cell in a direction is required (at least three times the original lattice) to allow the breaking of sp^3–sp^3 connections. Otherwise the optimization leads to a typical diamond system. As an example the (3,1) sp^2 armchair foam is shown in Figure 3.6 (a). Its distance $d = 3.24$ Å between the graphitic fragments as well as the bond lengths are similar to those of layered graphite, although the arrangement of the atoms is different. The mass density ($\rho = 2.47$ g cm^{-3}) of this foam is about the same as for the (1,1) zig-zag carbon foam. Analogous sp^2 foams were also discussed by Umemoto et al.[94] with similar conclusions.

Similar to the sp^2 foams, carbon foams can be constructed by screw twist-

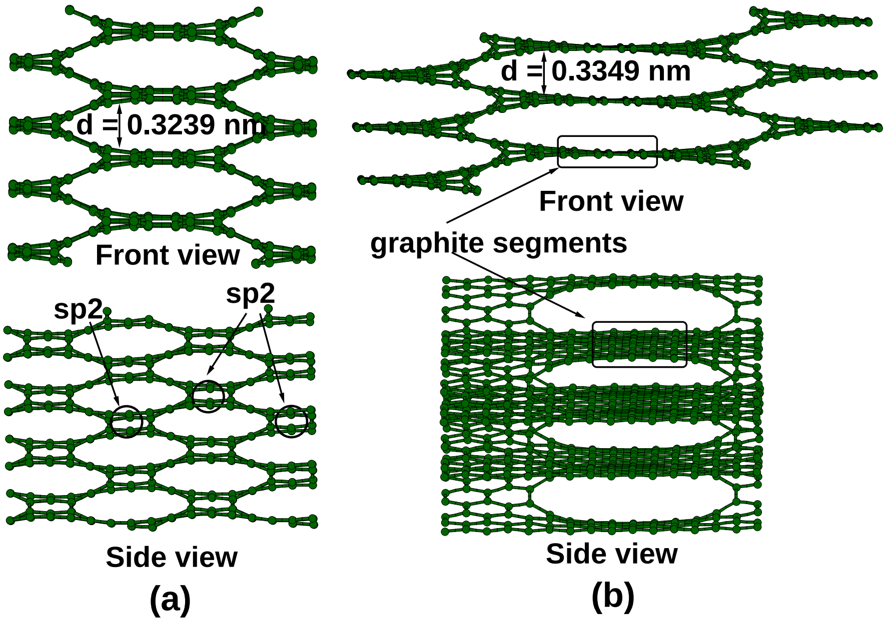

Figure 3.6: *The structure of* sp^2 *carbon foams: (a) the (3,1) armchair carbon foam and (b) screw dislocated graphite.*

ing of graphite layers. They can be related to the structure of 'Screw Dislocated Graphite (SDG)[47]' that is shown in Figure 3.6 (b). This type of carbon foams will be called 'screw dislocated graphite' or SDC in the following. SDC has the same interlayer distance and bond lengths as layered graphite. However, there are covalent bonds present in c direction that connect the neighboring graphene fragments parallel to the ab planes. By construction, these bonds are formed by providing atoms within the graphene layers with additional neighbors in c direction, locally removing planarity without changing the hybridization of the carbon atoms. The system - shown in Figure 3.6 (b) - corresponds to the SDG (7,1) armchair carbon foam.

Both types of sp^2 foams have different kinds of nanopores, but both form two-dimensional interconnected channels between the pores: the sp^2 carbon foams have direct connections between pores along the b direction [Figure 3.6 (a) bottom], while SDG connections are rather twisted [Figure 3.6 (b) bottom]. On the other hand, the $sp^2{-}sp^3$ carbon foams have closed nanopores (one-dimensional channels), similar to nanotubes.

3.1.3 Energetic and Mechanical Stability

The energetic and mechanical stability of different carbon foams was studied following the discussion in Section 3.1.1. The binding energy (per atom) as a function of n (n is the number of atoms per unit cell) is shown in Figure 3.7. The energy of carbon foams asymptotically approaches the binding energy of a graphene layer. According to the proposed model consideration (Section 3.1.1) the cohesive energy should follow a linear trend with respect to n^{-1}. Figure 3.8 shows that the energy of the investigated carbon foams indeed increases nearly linearly with n^{-1}, as expected from Equation (3.3). The deviations from the linearity [cf. Figure 3.8] may be explained by the differences in the types of boundary atoms (n_x) for a given type of structures. In zig-zag systems there are 8 sp^3 junction atoms per elementary unit cell, while 4 sp^2 and 4 sp^3 carbon atoms (per unit cell) occur at the junctions in armchair structures [cf. Figure 3.2]. The sp^2 carbon atoms in zig-zag foams form graphene stripes with a fully delocalized π-electron system. In armchair foams, the π-electron delocalization is distorted by the π bonds at the sp^2 atoms at the boundary of graphene-like stripes. This has obviously a stronger influence in smaller structures. For larger systems the bonding behavior of all boundary atoms becomes very similar, i.e. all structures have nearly the same n^{-1} size dependence. This is also confirmed by the observation, that the $sp^2{-}sp^2$ bond lengths in armchair systems depend on the size: The single and double bond lengths become similar with increasing the system size (Table 3.2). They slowly approach the values of bond lengths in graphite.

The calculations indicate that carbon foams are quite stable systems compared to the other well-known carbon allotropes. The origin of their favorable stability is the fact that the carbon foams discussed here do not contain bents, but only straight graphitic planes, in contrast to fullerenes and nanotubes that are also purely sp^2 bonded but exhibit curved graphitic fragments. The largest studied carbon foams [(5,5) zig-zag ($n = 116$) and (7,7) armchair ($n = 104$)] are almost as stable as graphite and diamond. Their cohesive energies were found to be smaller by only $\sim$0.09 eV atom^{-1} than that of a graphene layer ($E_{\text{bind}} = 7.986$ eV atom^{-1}). The least stable (1,1) zig-zag carbon foam ($n = 20$) with an energy of 7.538 eV atom^{-1} is as stable as the (5,5)

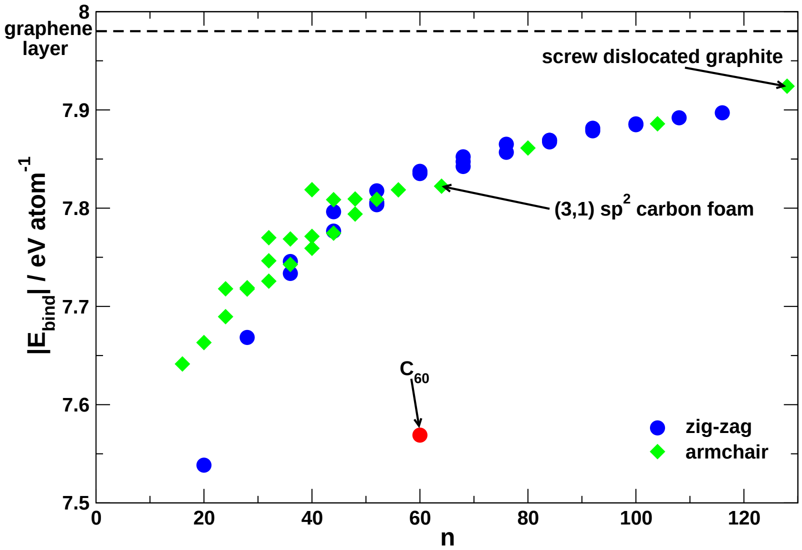

Figure 3.7: *The binding energy of the investigated carbon foams as a function of n (n-the number of atoms per unit cell). The corresponding energy of a single graphene layer is given as a reference (dashed line).*

armchair carbon nanotube ($E_{\text{bind}} = 7.539$ eV atom^{-1}) and similarly stable to the (10,0) zig-zag carbon nanotube ($E_{\text{bind}} = 7.501$ eV atom^{-1}). Furthermore, it was found that except for the (1,1) zig-zag carbon foam, all structures are more stable than the isolated C_{60} cage ($E_{\text{bind}} = 7.569$ eV atom^{-1} by at least $\sim$0.08 eV atom^{-1}. The sp^2 carbon foams are very stable, as well. As an example, the (3,1) foam is less stable by $\sim$0.16 eV atom^{-1} than the most stable carbon allotropes. The stability of SDG (7.924 eV atom^{-1}) and graphite/diamond is about the same. These results suggest that carbon foams can be stable once they have been formed.

The mechanical properties were studied by estimation of the bulk (**B**) and shear (**G**) moduli according to Equations (3.5) and (3.8). The results (Tables 3.3 and 3.4) show that with increasing size of the pores (N and M) the bulk modulus decreases. The smallest **B** belongs to the (1,5) zig-zag foam (4.25 GPa). The shear moduli have a similar tendency and the smallest value was found for the (7,7) armchair system (0.1 GPa). The most stiff carbon foam is the (1,1) zig-zag with **B** = 285.13 GPa and **G** = 176.95 GPa, because

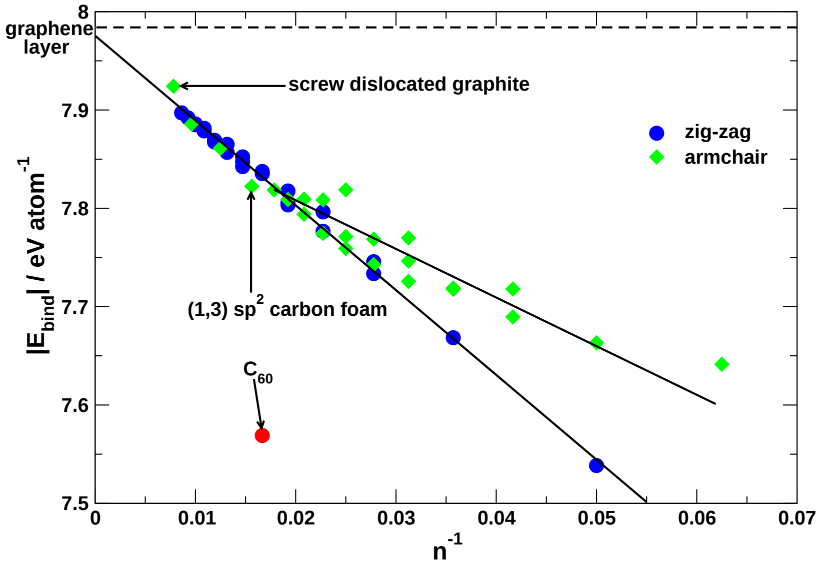

Figure 3.8: *The binding energy of carbon foams as a function of* n^{-1}*. The corresponding energy of a single graphene layer is given as a reference (dashed line).*

this structure is closest to the diamond structure. On the other hand, it is interesting to note that for a given pore size the armchair carbon foams seem to be mechanically more stable than the zig-zag structures. Another tendency is that the bulk as well as the shear moduli become smaller going from systems with $M = 1$ to $M = 5$.

As expected for structures built from graphite and diamond segments containing both sp^2 and sp^3 hybridized atoms, the calculated bulk moduli of the carbon foams vary over a wide range: ∼5 up to ∼300 GPa, i.e. ranging between that of graphite (5.5 GPa) and nearly approaching that of diamond (514 GPa). Moreover, the (3,1) armchair and SDG carbon foams also possess rather large bulk moduli of 48.5 GPa and 20.2 GPa, respectively, compared to graphite.

The **G** values of carbon foams are, however, clearly smaller than those of diamond (621 GPa) and for larger structures they become close to that of graphite (3 GPa). Evidently carbon foams are mechanically rather stable concerning the bulk moduli. However, it is important to notice that larger

Table 3.3: *The bulk and the shear moduli (**B** and **G**) of zig-zag carbon foams given in GPa.*

	B					**G**				
M N	**1**	**2**	**3**	**4**	**5**	**1**	**2**	**3**	**4**	**5**
1	285.1	89.0	21.5	8.25	4.25	176.95	53.1	15.3	4.3	3.6
2	265.5	157.7	54.85	18.3	6.95	105.8	32.3	13.5	6.6	3.2
3	225.2	172.9	97.0	69.5	21.0	122.7	17.9	8.7	8.1	4.6
4	148.6	137.3	124.8	73.9	69.1	142.8	11.6	6.3	4.6	4.6
5	183.5	107.9	109.4	98.9	75.5	76.5	7.95	5.0	3.8	2.9

Table 3.4: *The bulk and the shear moduli (**B** and **G**) of armchair carbon foams given in GPa.*

	B				**G**			
M N	**2**	**3**	**4**	**5**	**2**	**3**	**4**	**5**
1	266.7	78.2	28.8	12.6	64.35	24.65	12.45	7.9
2	213.3	156.3	57.4	23.4	26.2	16.8	9.2	6.4
3	140.6	162.1	95.7	47.2	12.2	8.7	4.7	4.3
4	89.6	114.8			9.0	4.3		
5	65.0	88.2	100.6	92.3	3.6	3.7	2.4	0.9

foams (Tables 3.3 and 3.4) could become unstable against shear forces, because of their small shear moduli. This behavior comes from the fact that carbon foams are highly anisotropic systems.

Furthermore, the properties of the investigated carbon foams with $M = 2$ and increasing N were studied to search for size dependent trends. The results are shown in Table 3.5. Indeed, these carbon foams slowly approach the properties of layered graphite. The bulk modulus reaches the maximum value at the (3,2) structure and decreases continuously with increasing sizes. As the foam with increasing size starts to mimic the structure of layered graphite, its binding energy increases as well. However, the mass densities are much smaller, because the distance between graphitic segments is almost three times larger than in layered graphite.

Table 3.5: *Calculated mass densities (ρ), bulk moduli ($\boldsymbol{B}$), band gaps (Δ) and binding energies per atom (E_{bind}) of zig-zag carbon foams with $M = 2$.*

(N,M)	ρ [g cm^{-3}]	**B** [GPa]	Δ [eV]	E$_{\mathrm{bind}}$ [eV atom^{-1}]
(1,2)	1.77	89.0	1.48	7.745
(2,2)	1.46	157.7	1.56	7.796
(3,2)	1.30	172.9	0.0	7.817
(4,2)	1.20	137.3	1.11	7.836
(5,2)	1.14	107.9	0.78	7.852
(6,2)	1.09	84.1	0.0	7.863
(7,2)	1.06	74.2	0.63	7.873
(8,2)	1.03	66.6	0.50	7.881
(9,2)	1.01	58.8	0.0	7.887
(10,2)	0.99	51.4	0.44	7.893
graphite	2.27	5.5	0.0	7.986

3.1.4 Electronic Properties

In this section the densities of states (DOS') and band structures of the investigated carbon foams are discussed. The calculated band gaps of zig-zag foams indicate a similar size dependence as for zig-zag nanotubes. They are metallic, if the distance between two junctions is a multiple of three hexagonal units:

$$(N, M) = [3 \cdot m, M] \tag{3.9}$$

and/or

$$(N, M) = [N, 3 \cdot m], \tag{3.10}$$

with $m = 1, 2, 3, \ldots$; otherwise the foams are semiconducting with a gap size in the same range as for semiconducting carbon nanotubes (0.6−1 eV). Similar to armchair carbon nanotubes, the armchair carbon foams are all metallic independent of their size.

Figure 3.9 shows the band structures and densities of states for the symmetric zig-zag carbon foams calculated in hexagonal lattices. These results are compared with the band structure and DOS of AA-stacked hexagonal graphite. Although the dispersion along the lowest conduction band as well as the highest valence band is very small, the systems were recognized as

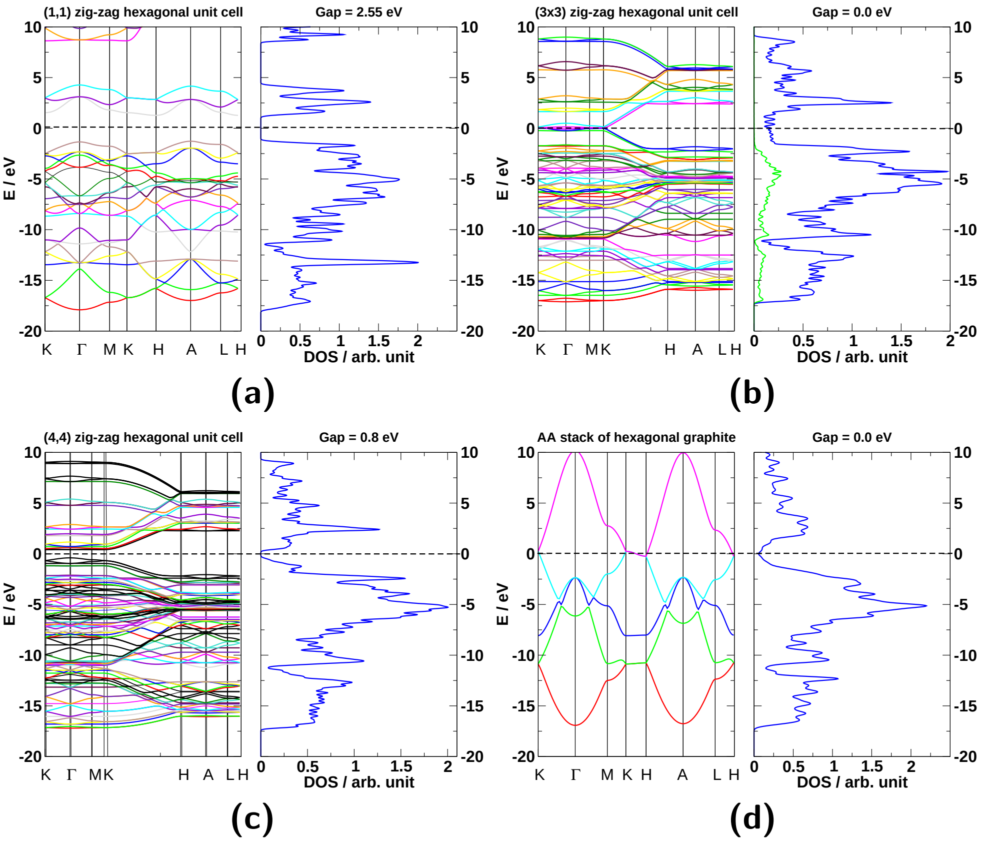

Figure 3.9: *The band structures and the densities of states of the symmetric zig-zag carbon foams (a−c) and graphite (d) in a hexagonal lattice representation. The green line in (b) denotes the PDOS of the sp^3 carbon atoms along the junction. The Fermi level is shifted to 0.0 eV (horizontal dashed lines).*

indirect-gap semiconductors. A distinct dispersion appears along the K−H lines [Figure 3.9 (b), (c)]. The electronic structure reveals that mostly the atoms in the direct neighborhood of the sp^3 carbon chains contribute to the bands near the Fermi level. The (3,3) zig-zag carbon foam is metallic with bands crossing the Fermi level at the K point of the Brillouin zone.

Some examples of band structures and DOS' of the orthorhombic ($N \neq M$) zig-zag carbon foams are shown in Figures 3.10 (a)−(b). These foams are metallic as it was stated in Equations (3.9) and (3.10). There is a visible large band dispersion along the $k_a - k_b$ plane [see Figure 3.3 for definition of

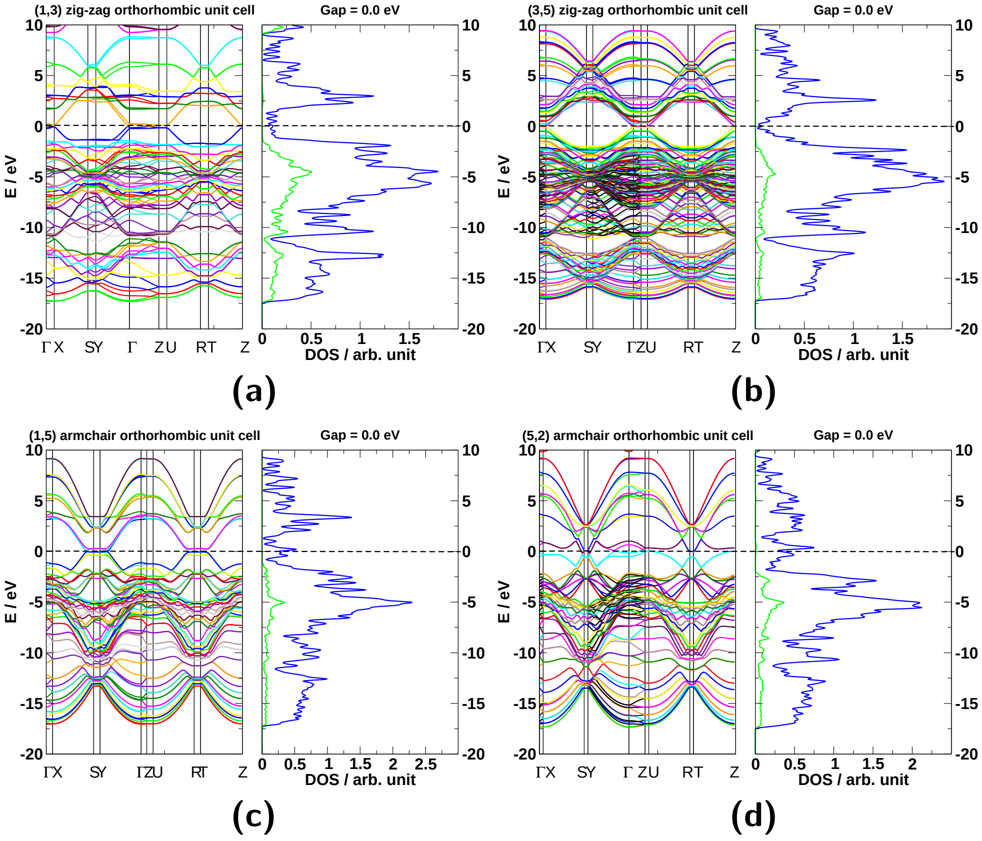

Figure 3.10: *The band structures and the densities of states of zig-zag (a, b) and armchair (c, d) carbon foams in an orthorhombic lattice representation. The green lines denote the PDOS' of the* sp^3 *carbon atoms along the junction. The Fermi level is shifted to 0.0 eV (horizontal dashed lines).*

k_a and k_b], similar to that of a graphene monolayer.

Band structures and DOS' of some armchair carbon foams are shown in Figures 3.10 (c)−(d). This group of metallic structures has bands crossing the Fermi level along the X−S and Y−Γ lines. Large dispersions of valence and conduction bands are visible as well.

PDOS' of the junction atoms (sp^3) are shown in Figures 3.9 and 3.10 for the metallic systems. It can be seen that the line of junction atoms has an insulating character and the metallic properties of the carbon foams are restricted to the graphene-like stripes with sp^2 hybridized carbon atoms.

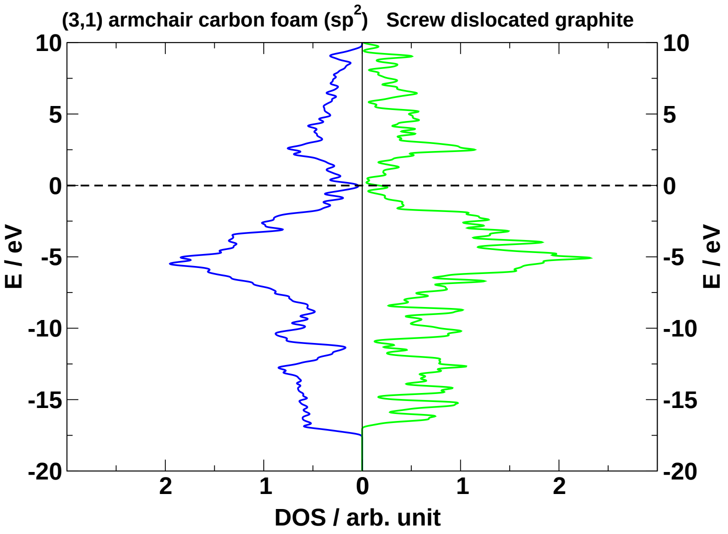

Figure 3.11: *The densities of states of the (3,1) armchair carbon foam (left) and the screw dislocated graphite (right). The Fermi level is shifted to 0.0 eV (horizontal dashed line).*

Thus, for larger semiconducting carbon foams the band gap will decrease with increasing size (cf. Table 3.5).

The family of sp^2 armchair foams is also metallic. The densities of states of the (3,1) structure and the SDG are shown in Figure 3.11. The band structures are very complicated and therefore not shown here. The DOS' of both systems are similar to that of layered graphite.

3.1.5 Foams Intercalated by Carbon Nanotubes

Since carbon foams are highly porous structures, their large cavities can act as hosts for several guest systems. This section is focused on the properties of carbon foams intercalated with carbon nanotubes (CNTICFs is used in the following). These structures are purely hypothetical. Such a combination of foams and tubes can change significantly the properties (e.g. mechanical properties) of the whole system compared to each component itself. This may also result in a changed sorption capability, as nanotubes inside pores of a foam may offer additional adsorption sites.

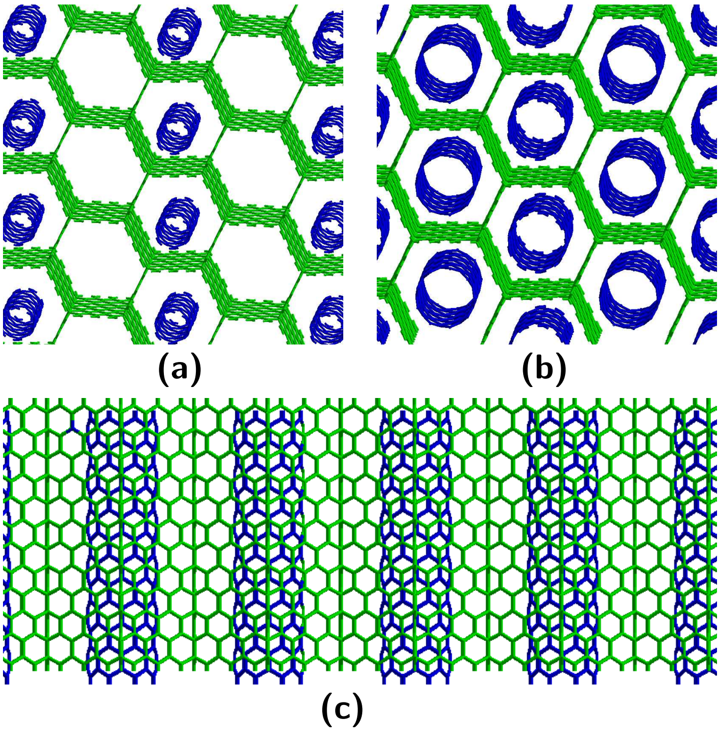

Figure 3.12: *The structures of the (3,3) zig-zag carbon foam intercalated by: (a) the (6,0), (b) the (9,0) and (c) the (8,0) carbon nanotube. The latter one (a side view) shows the ABAB-like stacking of the 6-fold rings between the foam and the tube.*

As a benchmark system the (3,3) zig-zag carbon foam was chosen. This foam is metallic with a bulk modulus of 97.0 GPa and a binding energy of 7.842 eV atom^{-1}. Figure 3.12 shows some examples of CNTICFs. Carbon nanotubes can intercalate a carbon foam in different ways. Two of them are discussed here: The first type of CNTICFs is with every pore in each second column occupied by a tube [Figure 3.12 (a)], whereas the second type has each pore intercalated by a CNT [Figure 3.12 (b)].

After the nanotube was introduced into a cavity, it has been observed that the arrangement between the tube and the foam mimic that of ABAB-stacked graphite [cf. Figure 3.12 (c)] with respect to the six-membered rings of both moieties. This is connected to the van der Waals interactions between the two moieties. Moreover, smaller tubes inside a large cavity of the foam shift to one of the corners of the foam, as in the case of the (6,0) carbon nanotube [cf. Figure 3.12 (a)]. The diameter of this nanotube is 4.77 Å. Taking into account the diameter of the foam pores (13.75 Å) one can see that the remaining distance between walls of the tube and the foam (4.49 Å) is larger than the van der Waals interlayer distance in graphite. Thus, the tube shifts closer to one side of the foam pore to allow an optimal interaction distance as in the layered graphite.

The properties of these combined systems are shown in Table 3.6. The results indicate that CNTICFs are energetically slightly less stable than the corresponding empty carbon foam. However, the stability increases with the size of the introduced CNT. The metallic character of the foam is kept in the combined systems. Mass densities increase for larger tubes, but stay lower or equal to that of graphite ($\rho = 2.27$ g cm^{-3}). Considering the bulk moduli of CNTICFs one can see that introduction of a larger tube indeed increases the stiffness of the carbon foam. For a (10,0) nanotube in every pore, the bulk modulus raises from 97.0 GPa to almost 180 GPa.

3.1.6 Defected Graphite

Graphite is well known as a moderator in nuclear reactors. Under irradiation the defined layered structure of graphite changes significantly and many defects are created. Often occurring defects, vacancies or interstitials can merge into extended defects called dislocation loops or lines. Aggregation of interstitials cause the interlayer distance expansion due to the formation of new layers. Vacancy lines, on the other hand, produce the basal contraction. In this section, two of the recently reported[47] dislocations are investigated: the zig-zag and the armchair prismatic edge dislocations.

Under strong irradiation the original layered structure of graphite ($d =$ 3.35 Å) is lost. Two types of highly defected graphite structures are shown in Figure 3.13. Both are formed from ABAB-stacked graphite.

In the zig-zag prismatic edge dislocated system the neighboring layers are interconnected locally by sp^3 carbon atoms [Figure 3.13 (a)]. This structure is similar to the carbon foams discussed above. Unlike in the carbon foams, the

Table 3.6: *Calculated mass densities (ρ), bulk moduli ($\boldsymbol{B}$) and binding energies per atom (E_{bind}) of the (3,3) zig-zag carbon foam intercalated by carbon nanotubes.*

(L,M)	ρ [g cm^{-3}]	**B** [GPa]	E$_{\mathrm{bind}}$ [eV atom^{-1}]
		Type I*	
(6,0)	1.40	107.4	7.774
(7,0)	1.47	97.6	7.797
(8,0)	1.53	104.6	7.813
(9,0)	1.59	119.6	7.823
(10,0)	1.65	138.0	7.829
		Type II*	
(6,0)	1.77	70.2	7.738
(7,0)	1.89	96.8	7.776
(8,0)	2.02	110.8	7.801
(9,0)	2.14	134.7	7.816
(10,0)	2.26	178.4	7.824

* - **Type I**: tubes in every second column of pores;
Type II: tubes in each pore.

sp^3 carbons connect only two graphitic stripes with sp^2−sp^3 C−C bonds of 1.491 Å. The occurrence of sp^3 hybridized atoms causes a reorientation of the single layers leading to the formation of connected double layers (containing loops or cavities). The cavities have a width of 6.7 Å. Each double layer is repeated with about 10 Å distance, thus the minimum distance between two graphitic fragments is as large as in layered graphite (3.3 Å).

On the other hand, the armchair prismatic edge dislocations are characterized by formation of wrinkled not bonded graphene layers [Figure 3.13 (b)]. In this case, well-defined cavities and a d-expansion appear due to the bends of the graphene layers. No direct connections between the neighboring layers exist and thus, the system is built only from sp^2 hybridized carbon atoms. This structure can be considered as an intercalated graphite similar to C_{60}-intercalated graphite, which will be discussed in the next section. Here the intercalant is simply a curled graphene layer. The bond lengths are typical for graphite. The maximal separation between the flat and the curled layers is about 6.8 Å, whereas the minimum is around 3.2 Å. The bent layers

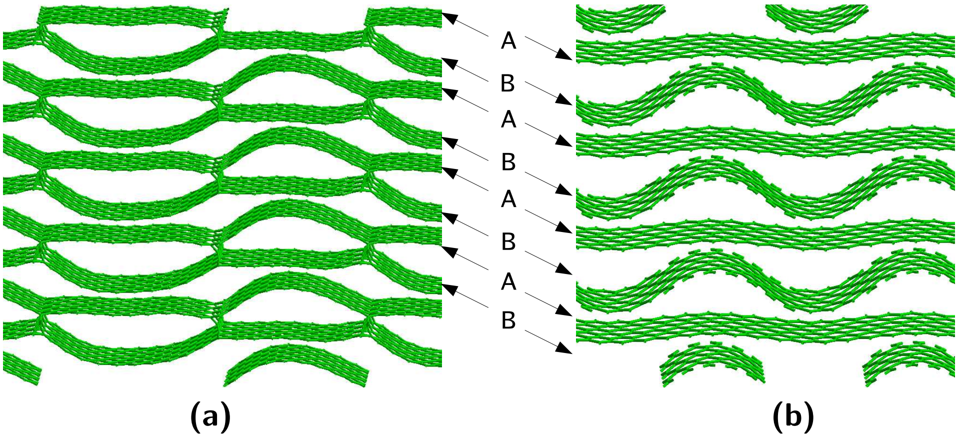

Figure 3.13: *(a) The zig-zag and (b) the armchair prismatic edge dislocations in layered graphite. A and B indicate the stacking of layers.*

can be considered as spacers in the AA-stacked graphite with an interlayer distance of 10.0 Å.

As both structures have pores with diameters larger than the van der Waals distance in graphite, the mass densities decrease from $\rho = 2.27$ g cm^{-3} (graphite) to $\rho = 1.62$ g cm^{-3} for both dislocated graphite modifications. The size of the pores (≈7 Å) of both structures is about the same as the optimal distance for hydrogen storage found for carbon slit-pore materials.[12,24] Moreover, they are very stable having binding energies of 7.88 eV atom^{-1} and 7.94 eV atom^{-1} for zig-zag and armchair dislocations, respectively.

3.2 C_{60}-Intercalated Graphite

The graphite intercalated compounds are well known for over 20 years.[107] A wide range of different atomic and molecular intercalants were discussed in the literature, among them K, Li, Rb, HNO_3, $AlCl_3$, AsF_5, etc.[107] The intercalation has been proposed as an interesting solution to expand the graphite lattice with the sheets kept intact. Recently, even larger carbon-based systems, like C_{60} molecules, have been used as intercalants.

In 1994 Fuhrer et al.[108] have proposed a new class of materials formed by the intercalation of C_{60} and alkali metals into a graphite host. In this way materials with single layers of doped C_{60} in between the graphite layers are formed. As an example, the synthesis of $C_{32}K_4C_{60}$ structure was proposed. The intermolecular spacing in this compound was predicted to be 10.0 Å and the graphite interlayer distance d to be about 13 Å.

However, pure C_{60} intercalated graphite (CIG) - first synthesized by Gupta et al.[92] - is more attractive than doped materials considering the storage applications. The lack of alkali metals offers a lower mass density and additional free space for guest molecules. The synthesis of CIG is rather simple: The 2:1 weight ratio of C_{60} and graphite is vacuum sealed in a quartz tube. This is next put into a furnace at 600°C for two weeks. The high-resolution transmission electron microscopy (HRTEM) images indicate the hexagonal pattern of close-packed C_{60} cages in between the graphite layers.

This section is focused on the separation of graphene layers by means of C_{60} fullerenes as spacers.[44]

3.2.1 Computational Details

The structures of a graphene layer and the C_{60} molecule were optimized at the DFTB level of theory. The geometry of C_{60} intercalated graphite was obtained from molecular mechanics (MM) calculations using the Universal Force Field (UFF), which was re-parametrized in terms of weak interactions for such light elements as carbon. The calculations were performed using the deMon code.[109] All energies were calculated at the DC-DFTB (dispersion corrected-DFTB) level (Section 2.4) as follows:

$$E_{\text{atom}} = \frac{E_{\text{tot}}}{N} - E_{\text{free}} \tag{3.11}$$

where E_{tot} denotes the total energy, N the number of carbon atoms in the unit cell, and E_{free} the energy of a free carbon atom. The AA-stacked graphite structure was used in this study. Periodic boundary conditions were employed to calculate the infinite crystal structure. Different positions and rotational orientations of C_{60} between the graphene layers were investigated. The band structure was computed along lines between high symmetry points of the Brillouin zone. The first Brillouin zone with the highly symmetric points for an orthorhombic unit cell is shown in Figure 3.3 (d) (Section 3.1.1).

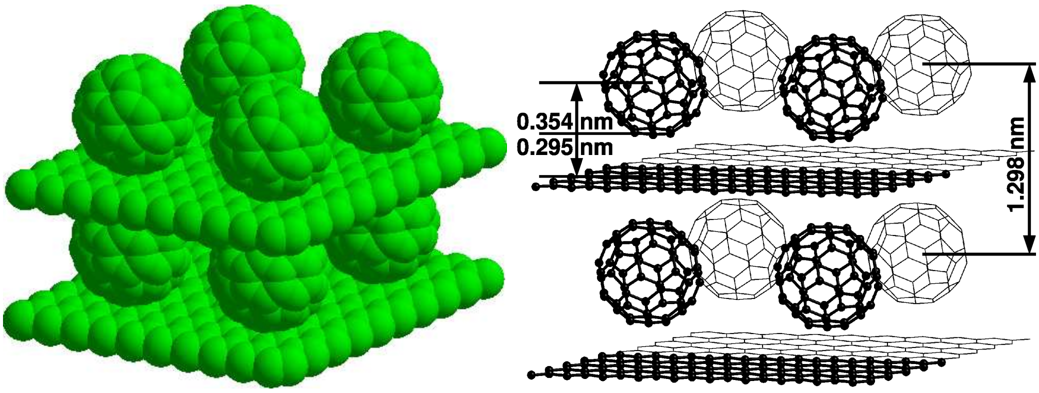

Figure 3.14: *The structure and the calculated center-to-center distances of* C_{60} *intercalated graphite in the hexagonal pattern.*

3.2.2 Structure

The structure of CIG is shown in Figure 3.14. In this system there are no direct covalent connections between the graphene layers and the C_{60} cages. In detail,[44] the calculated graphite interlayer distance is 12.98 Å and fits well the experimental findings of 12.7 Å.[92] Also, it is in perfect agreement with the predictions of Fuhrer et al.[108] for potassium-doped CIG. At the DFTB level of theory, the C_{60} radius of 3.54 Å is in close agreement with 3.55 Å found in X-ray experiments.[92,110] The van der Waals diameter between the cage and the graphene sheet was calculated to be 2.95 Å. The C_{60} center-to-center in-plane distance of about 12.3 Å, was estimated from the HRTEM image in the work of Gupta et al.[92] For the interlayer geometry the experimentally observed hexagonal pattern was used in the calculations, with the lattice constant of 12.5 Å. The center-to-center in-plane distance is by ∼2 Å larger than the one predicted for $C_{32}K_4C_{60}$.[108] Thus, this value was further optimized as well. After optimization, the C_{60} in-plane intermolecular distance dropped down to 10.1 Å, which fits to the predicted value for $C_{32}K_4C_{60}$. The energetically most favorable was hexagon-to-hexagon orientation with ABAB-like stacking between the C_{60} cage and the graphene layer. The calculated mass density of CIG (1.28 g cm^{-3}) is much smaller than that of pure graphite (2.27 g cm^{-3}) or solid C_{60} (1.73 g cm^{-3}). This fact is attractive for the possibility of gas

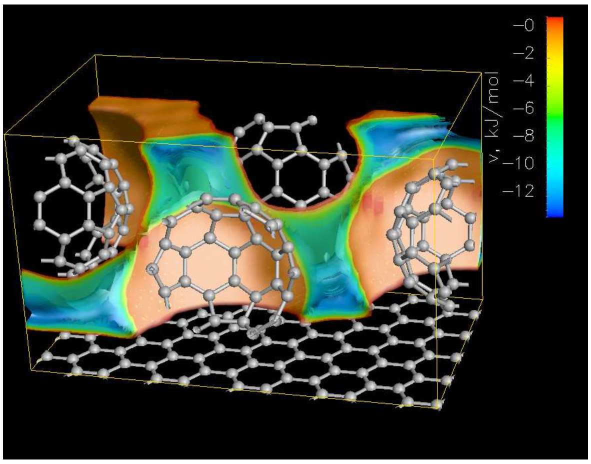

Figure 3.15: *The interaction potential between hydrogen molecule and* C_{60} *intercalated graphite in a hexagonal pattern. The potential energy isosurface is shown in a diagonal cut through the unit cell.*[44]

storage or sieving applications.

For CIG the active volume was found in the fosses and the grooves between the fullerenes and the graphene sheets, where the potential reaches the most negative value [-12.5 kJ mol^{-1}; Figure 3.15]. On the other hand, the active volume of CIG, determined by numerical integration, is found to be 19% of the total volume. In comparison, the same structure without fullerene spacers has an active volume of 62%. (The active volume can be defined as the space of attractive guest-host potential.) Thus, there is a need of lowering the density of C_{60} molecules between the graphene layers to optimize the structure in order to be a better storage medium.

3.2.3 Energetic Stability and Electronic Properties

The stability of CIG was compared to different carbon forms by means of atomization energies per carbon atom, according to Equation (3.11). CIG has an atomization energy per atom of 7.746 eV atom^{-1}. Hence, it is less stable than the most stable carbon allotropes, graphite and diamond, by about 0.24 eV atom^{-1} (see Table 3.7). CIG is, however, more stable than the isolated and solid C_{60}. The results indicate that this system is energetically

Table 3.7: *Calculated atomization energies per C atom (E_{atom}), gap energies (Δ) and mass densities (ρ) for various carbon allotropes*[a]*.*

Structure	E_{atom} [eV atom^{-1}]	Δ [eV]	ρ [g cm^{-3}]
graphite	7.986	0 (0)[111]	2.27 (2.27)[111]
diamond	7.982	6.88 (6.0)[111]	3.54 (3.51)[111]
C_{60} (gas phase)	7.555	1.78 (1.7)	
C_{60} (solid)	7.569	1.67 (1.7)[112]	1.73 (1.72)[112]
CIG	7.746	0	1.28

[a] Experimental values are given in parenthesis.

relatively stable.

The partial density of states and the band structure of C_{60} intercalated graphite is shown in Figure 3.16. The results indicate that CIG has a zero band gap. The C_{60} does not disturb the semi-metallic character of graphene layers. The bands cross the Fermi level at one point, similarly to pure graphite [see Figure 3.16 left]. Close to the Fermi level the bands are dominated by $2p$ states. The PDOS of the C_{60} carbon atoms in CIG is similar to that of pure solid C_{60}. The separation of the top of the valence band and the bottom of the conduction band is, however, slightly smaller in the CIG band structure. CIG keeps the parabolic spectrum around the Fermi energy that is typical for graphite systems.

3.3 Summary

In this chapter, different graphite modifications, carbon foams, defected graphite, and C_{60} intercalated graphite, were investigated. In the case of carbon foams, functionalization of the graphene layers was employed to expand the interlayer distance. The functionalization transforms sp^2 to sp^3 carbon atoms and allows covalent interlayer connections. As a consequence, a chain of sp^3 carbons appears along the pore junctions. Since carbon foams contain both sp^2 and sp^3 hybridized atoms, they can represent novel carbon modifications. Foam-like systems with only sp^2 hybridized atoms are also known and these structures have properties close to those of layered graphite.

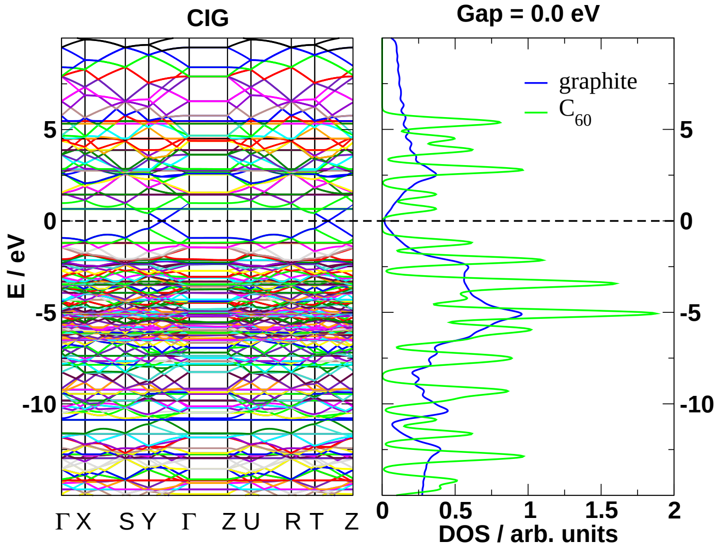

Figure 3.16: *(left) The band structure and (right) the partial density of states of* C_{60} *intercalated graphite. The Fermi level is shifted to 0.0 eV (horizontal dashed line).*

The present computations confirm high stability of carbon foams as compared to the most stable carbon allotropes (graphite and diamond). The foams have large bulk moduli, although they might become less resistant against shear forces, when the size of the pores is increased. The stiffness of carbon foams can be improved by intercalation with e.g. carbon nanotubes. The electronic properties of the investigated foams are very similar to those of carbon nanotubes. Zig-zag carbon foams are metallic only, if one of the walls has a size, which is a multiple of three hexagonal units. Otherwise, the zig-zag foams are semiconducting. Armchair foams have metallic character independent of their pore size.

High porosity, crystal-like structure and low mass density are very attractive features, in particular for guest-host interactions. Carbon foams were found to reach at the same time[24] the gravimetric and volumetric capacities proposed by DOE.[13]

Upon irradiation layered graphite may undergo a kind of dislocation and result in a defected graphite. In a zig-zag prismatic edge dislocation the interlayer distance is increased by locally present sp^3 carbon atoms which interconnect two neighboring layers. The second type is an armchair prismatic edge dislocation, where no sp^3 carbons exist and the distance is increased by the presence of wrinkled layers in between. This graphite modifications were found to be as stable as non-modified graphite. By means of volumetric capacity these structures easily reach the target of DOE.[24]

An alternative possibility to increase the interlayer distance is intercalation: In this case, the graphene sheets are kept intact and no direct connections exist between them and the intercalant. The size of the resulting cavities depends on the size of the spacers. As an example, C_{60} intercalated graphite was investigated. Here, the graphene layers are separated by a layer of close-packed fullerenes. The results confirm the structure and the stability of the recently reported CIG system.[92]

The shape of the spacers allows a free penetration of H_2 into and out of the material with no effect on its structural properties. The spacers double the interaction free energy of the material with H_2.[44] On the other hand, the fullerenes reduce the active volume of 62 % of the structure without spacers to 19 % in CIG, in which the C_{60} cages are hexagonal close-packed. Therefore, for hydrogen storage more promising materials could be created, if it would be possible to reduce the density of C_{60} inside CIG.

The discussed carbon nanostructures represent interesting systems to follow the realization of hydrogen-storage devices based on physisorption. The expansion of the interlayer distance in graphite is one of the most important factors to optimize graphite-based materials for practical storage applications.

Chapter 4

METAL-ORGANIC FRAMEWORKS

The assembly of new materials with tailored properties from well defined molecular building blocks[113] is nowadays of great interest. Copolymerization of a wide range of organic molecules with polynuclear complexes can result in the formation of Metal-Organic Frameworks (MOFs)[32,33,114–116] that are considered as a new class of coordination polymers. MOFs with their inorganic connecting units (based on a transition metal complex or cluster) and the manifold of organic linker molecules are promising materials with uniform and monodisperse pore sizes in the nanometer region.

For a given topology of a connector, e.g. a tetrahedral Zn_4O cluster, one can obtain isoreticular series of metal-organic frameworks. Indeed, such materials with zinc carboxylate clusters have been successfully synthesized by Eddaoudi et al.[117] using a strategy based on reticulating metal ions and organic carboxylate linkers into extended periodic structures. They have obtained 16 different metal-organic frameworks, so-called isoreticular MOFs (IRMOFs). Novel strategies of synthesis allow a systematic variation of the pore size using different organic linkers without changing the cubic topology of the whole framework. MOFs with non-cubic topologies are also known and the structures are obtained by changing the inorganic connector moieties. The synthesis of crystalline MOFs is simple and based on mixing together a solution of the acid form of the linker and a simple metal salt in the desired stoichiometry, as described in the literature.[117]

The scanning electron microscopy (SEM) images and the structures of two exemplary MOF materials are shown in Figure 4.1: $Zn_4O(BDC)_3$ (BDC: benzene-1,4-dicarboxylate)[117] and $Cu_3(BTC)_2(H_2O)_3$ (BTC: benzene-1,3,5-tricarboxylate).[115] The first structure, IRMOF-1, contains a tetrahedral array of the connector, while the second is based on a pseudooctahedral coordination sphere with an additional axial aqua ligand.

The framework topologies can be predicted by consideration of the geometry and conformational informations of secondary building units [SBUs; see Figure 4.2]. MOFs exhibit unique framework properties such as interpenetration, dynamical crystal-to-crystal transformations and chirality. Other properties of MOFs, such as cavity radius, density and free volume, can be widely varied, leading to the lowest known densities for a crystalline material.[119] These materials exhibit very large specific surfaces (1000−6000

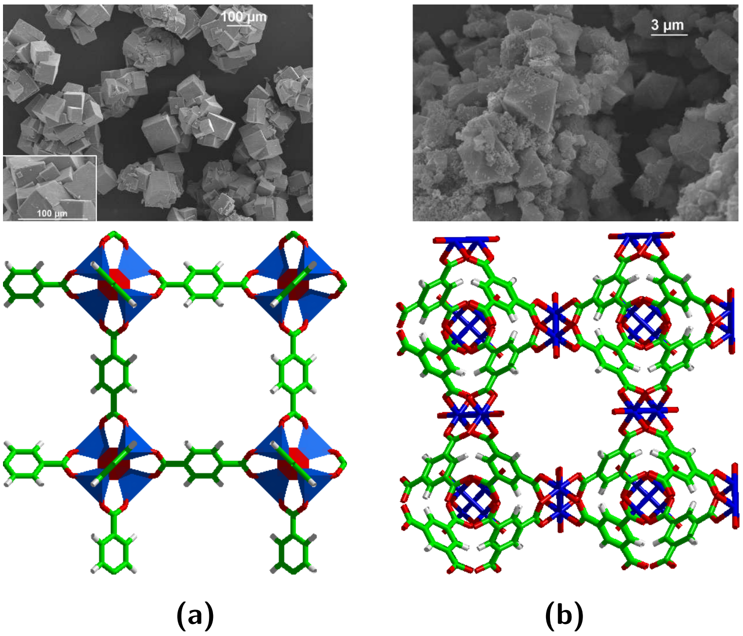

Figure 4.1: *The scanning electron microscopy images (adopted from the work of Panella et al.*[118]*) and the corresponding structures of: (a) IRMOF-1 ($Zn_4O(BDC)_3$; BDC: benzene-1,4-dicarboxylate) and (b) $Cu_3(BTC)_2(H_2O)_3$ (BTC: benzene-1,3,5-tricarboxylate).*

m^2g^{-1}).[120]

Taking into account the architecture of MOF materials, their properties can be modified by: substitution of the linker by other organic molecules, substitution of the connector (changing the metal atoms in it) or exchanging both, the linker and the connector. Such open-framework materials display flexibility and expand in size to accommodate adsorbed guests, thereby making MOFs interesting for gas separation, catalysis, molecular sensors and so forth.[36,119,121–124] The possibility to control the architecture, the pore size distribution, the functionalization of the organic part, as well as large surface areas, provide these crystalline compounds as excellent systems in molecular sorption applications.[35–37] Moreover, several possibilities of increasing the gas adsorption in MOFs have been suggested in the literature, among them catenation and inclusion of 'open' metal sites.[40,43,120,124] Catenation produces smaller pores and more adsorption sites per unit cell, which both

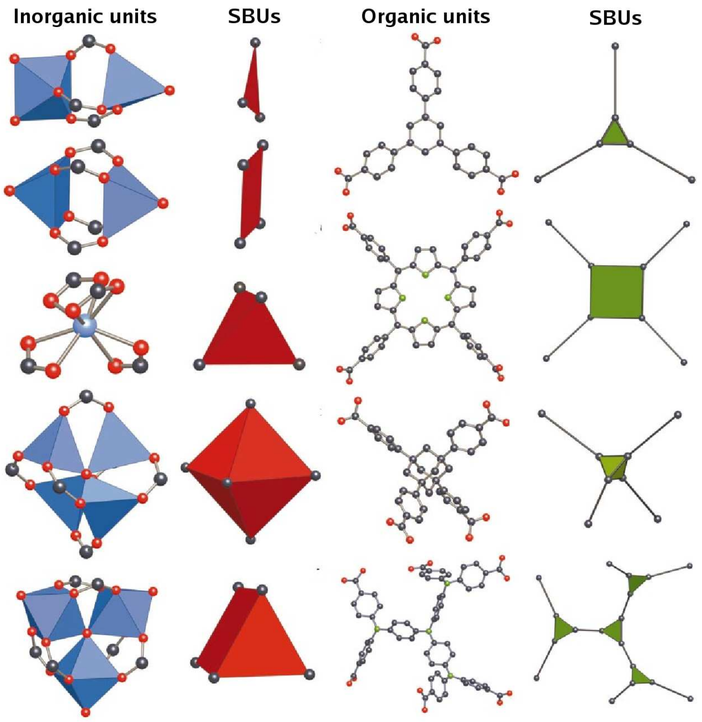

Figure 4.2: *Examples of inorganic connectors and organic linkers, and the corresponding secondary building units. Adopted from the work of Yaghi et al.*[32]

should provide higher heats of adsorption. Open metal sites should increase the guest-host interaction.

This chapter is organized as follows: MOFs, also catenated, with a Zn-based connector and different organic linkers are discussed in Section 4.1. Section 4.2 shows the results on Cu-based MOF with open metal sites. In Section 4.3 the guest-host interactions between H_2 and IRMOF-1 are investigated. Finally, the results are summarized in Section 4.4.

4.1 Zn-Based Metal-Organic Frameworks

This section is devoted to the properties of Zn-based metal-organic frameworks, built up with a tetrahedral ZnO connector. Such a topology of the connector gives a series of cubic networks, which differ only in the type of the

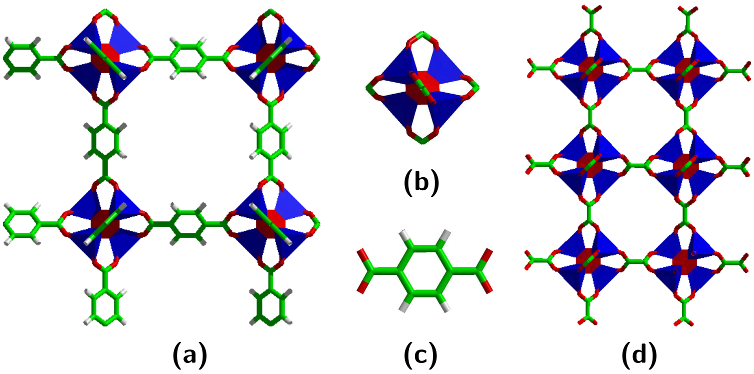

Figure 4.3: *The structure of IRMOF-1 (MOF-5) consists of cubic fragments (a). The corners of each cube are built up of a connector (b). The connectors are linked by organic linkers (e.g. benzene-1,4-dicarboxylate) (c), which form the edges of the cube. The connector can be described as four distorted tetrahedra* $Zn(O)_3O$ *connected by a central O atom. (d) The chosen reference system (IRMOF-M0; see text). Blue, red, white and green represent Zn, O, H and C atoms, respectively.*

linker. The smallest in this series, IRMOF-1, is shown in Figure 4.3 together with its building blocks. The investigations were focused on the structures, in which the linker in IRMOF-1 was exchanged by other organic molecules.

Theoretical investigations of just a few MOF structures have so far been reported in the literature.[125–129] The exchange of the transition metal (Zn by Cd, Be, Mg or Ca) in IRMOF-1 has been studied theoretically for example by M. Fuentes-Cabrera et al.[125] LDA calculations of the geometry, electronic and mechanical properties were performed for IRMOF-1 by Mattesini et al.[127] using periodic boundary conditions (PBC). Kim et al.[128] have employed GGA-DFT with PBC in their calculations of the IRMOF-x structures ($x = 1, 3, 18$). These systems are derived from IRMOF-1: the hydrogen atoms in the benzene ring are substituted by a $-NH_2$ group (IRMOF-3) or a $-CH_3$ group (IRMOF-18). For these materials the authors have investigated mainly the electronic structures. Semiempirical, HF and DFT calculations were also employed by Braga et al.[126] to study the structure of IRMOF-1. They used different model systems to represent the properties of the crystal structure: starting from $Zn_4O(CH_3COO)_6$ through $Zn_4O(PhCOO)_6$ up to the enlarged system of $C_6H_4(COO)_2(Zn_4O)_2(CH_3COO)_{10}$. In the work of Civalleri et al.,[129] the authors have calculated IRMOF-1 employing DFT calculations at the B3LYP level using PBC. After a geometry optimization, they have performed calculations of a deformation charge density map with respect to the isolated atoms (using Born effective charges) as well as the electronic structure and the vibrational frequencies calculations.

In this section, the results from a systematic study are presented and an overview over the properties of a wide range of IRMOFs[130] is given. The investigations are focused on the the organic linker nature in metal-organic frameworks.

4.1.1 Computational Details

The DFTB method (see Section 2.4) was used to determine the geometry, stability and the electronic structure of isoreticular series of Zn-MOFs. Some of the initial structure models of IRMOFs were built from the reported crystal structure data.[36,131] Periodic boundary conditions were used to represent the framework of the crystalline solid state. The lattice parameters as well as the structures were fully optimized. The number of **k**-points was determined by reaching convergence for the total energy as a function of the number of **k**-points. The mechanical properties were investigated by determining the bulk moduli (see Section 3.1.1 for details). The Mulliken atomic charges and densities of states were calculated in order to describe the electronic properties of the MOFs. Molecular dynamics (MD) simulations were performed within NVT ensembles at room temperature and 1200 K to check the thermal stability of these materials.

Both, well reported and hypothetical structures with the $(OZn_4)^{6+}$ connectors linked by different organic molecules are investigated. Such an architecture results in highly porous materials. Figure 4.4 shows a large variety of organic linkers considered in the present studies. They are either polycyclic hydrocarbons (PAHs) or carbon cages (cubane, dodecahedron, fullerenes). As a reference system, a hypothetical structure without an organic linker [named IRMOF-M0; see Figure 4.3 (d)], was chosen. Here, the letter M stands for modified or hypothetical systems.

The linkers are divided into four groups.[130] In the remainder, the numbering of atoms will be used according to Figure 4.5:

- Group 1: symmetric linkers with O2–C1–C1–O2 atoms in the same line coinciding the linkage axis (IRMOF-1, IRMOF-993, IRMOF-13/14, etc.) [Figure 4.5 (a)];
- Group 2: asymmetric linkers relative to the linkage axis, but with O2–C1–C1–O2 atoms in the same line (IRMOF-7, IRMOF-M4a, IRMOF-M5, etc.);
- Group 3: symmetric linkers with O2–C1–C1–O2 atoms not in the same line (IRMOF-8, IRMOF-M1b, IRMOF-M6b, etc.) [see Figure 4.5 (b)];
- Group 4: asymmetric linkers with O2–C1–C1–O2 atoms not in the same line (IRMOF-M4b, IRMOF-M3d, IRMOF-M6a, etc.).

MOFs with face-centered cubic (FCC), simple cubic (SC) or body-centered cubic (BCC) [Figure 4.6] crystal structures were taken into account. BCC structures can be considered also as a two-fold interpenetrated SC systems.

4.1.2 Structures

The structures considered in the present section can be represented as octahedral arrays of dicarboxylate organic bridges connected to a complex of tetrahedral $(OZn_4)^{6+}$ moieties. As an example the structure of IRMOF-1 (MOF-5) is shown in Figure 4.3 (a). This system can be considered as composed of two distinct structural units: the zinc-oxide-based connector [Figure 4.3 (b)] and the benzene-based linker [Figure 4.3 (c)], resulting in a porous cubic network.

A linker and a connector are both designed to assemble three-dimensional open frameworks [Figure 4.3]. The connector is a complex consisting of four distorted $Zn1(O1)_3O2$ tetrahedra, which are connected by a central O2 forming a $(Zn1)_4(O2)$ tetrahedron. Such an arrangement creates six inorganic (zinc-oxo carboxylato) and six organic (e.g. benzene) rings per corner [Figure 4.5]. Dicarboxylate organic linkers form rigid metal carboxylate clusters

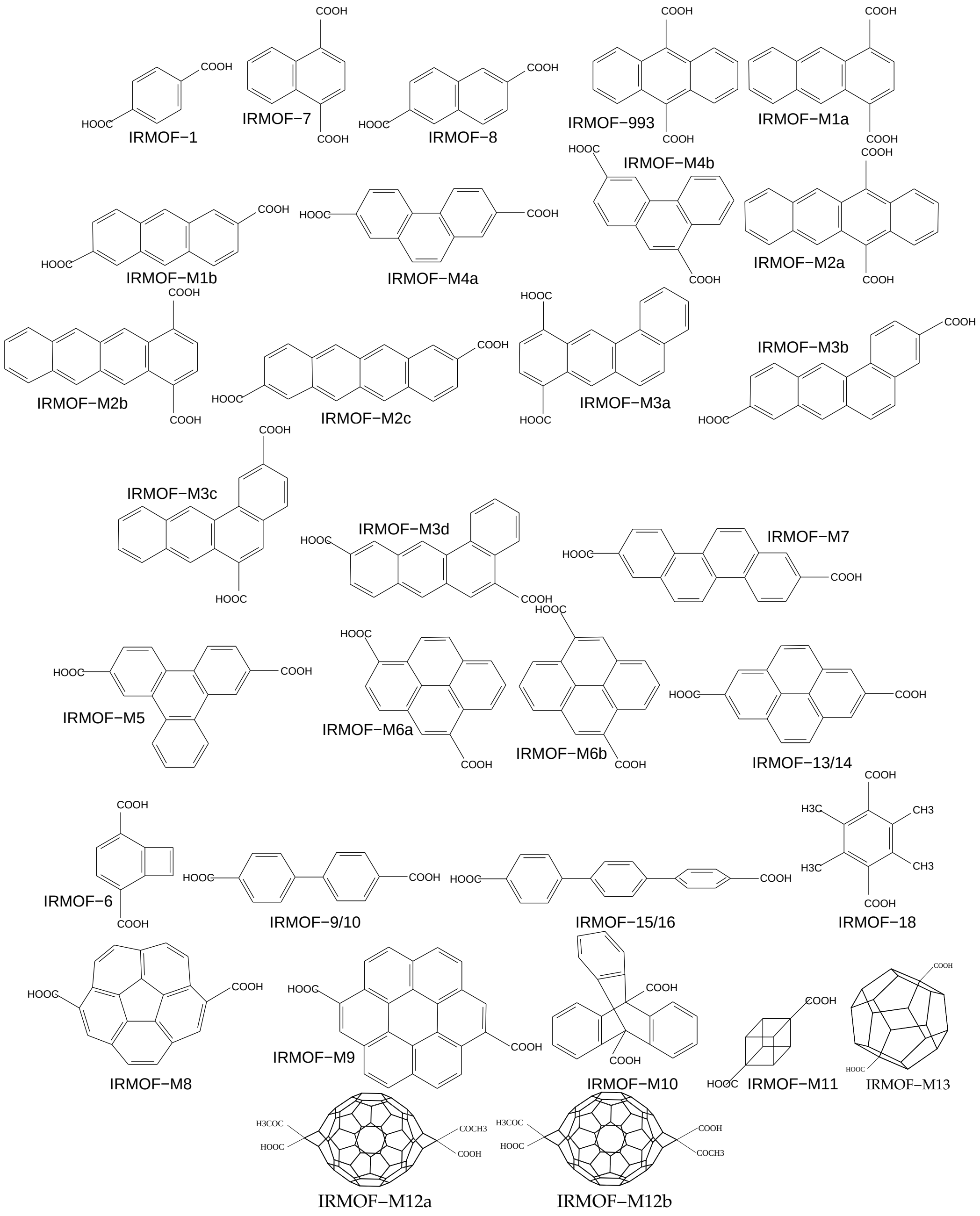

Figure 4.4: *Organic linkers considered in the present work. For clarity hydrogen atoms are not shown. Notation: IRMOF-x, where* $x = 1, 2, 3 \ldots$*, corresponds to the name given in the literature for experimentally known MOFs. IRMOF-Mx denotes the proposed linkers for hypothetical MOFs studied here (a, b, c, etc. indicate different isomers for a given linker).*

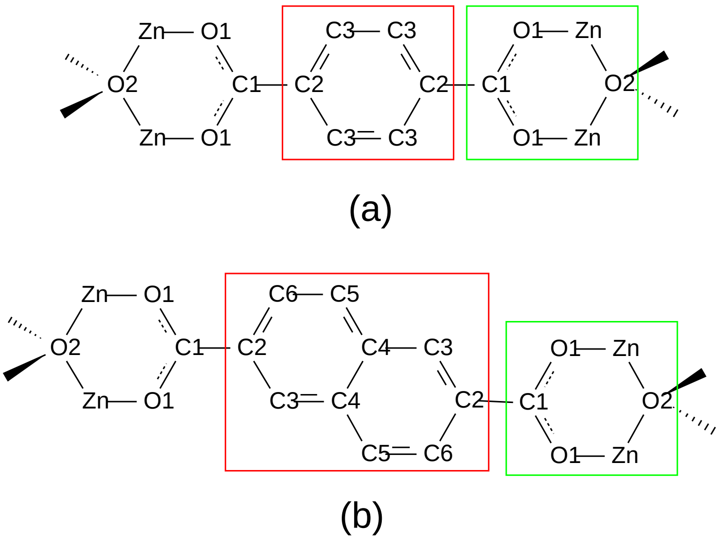

Figure 4.5: *The representation of the zinc-oxo carboxylato (green) and the organic rings (red) in IRMOF-1 (a) and IRMOF-8 (b). Both rings are in an 'in-plane' orientation; the numbering of atoms is given, as well. For clarity hydrogen atoms are omitted.*

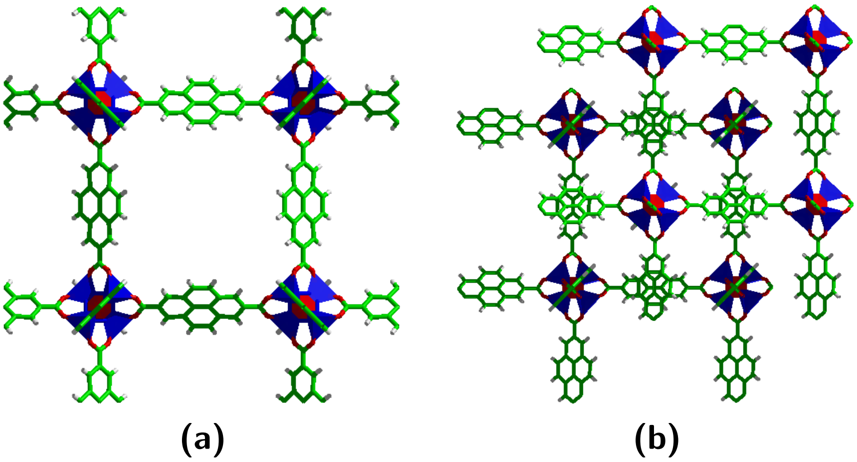

Figure 4.6: *The structure of IRMOF-14 in a simple cubic (a) and a body centered cubic (b; IRMOF-13) representation.*

that act as secondary building units in the extended solid. The way of connection between the building blocks in a MOF is as important as the molecular units themselves.[32,117,119]

The calculated equilibrium distances of selected bonds in the studied MOFs are summarized in Table 4.1. The results are compared with the available experimental data. Table 4.1 reveals that the bond lengths in the zinc-oxo carboxylato rings of different organic linkers are almost unchanged compared to the reference system of IRMOF-M0. The calculated C−C bond lengths agree very well with the corresponding measured distances (ΔR <2%). The agreement between calculated and experimental O−C distances is also good (ΔR ∼2−3%). However, the O−C distances in IRMOF-7, -8, -14 are somewhat larger than the experimental findings. Also the calculated Zn−O distances are slightly larger than measured bond lengths. However this overestimation is uniform for all systems, where experimental data was available.

Table 4.1: Selected bond distances [Å] and the O1−Zn−O1 angle [deg.] of the zinc-oxo carboxylato ring in different IRMOFs. The atoms are numbered according to the crystallographic positions [Figure 4.5]. The experimental values are given in parenthesis. (SC−simple cubic, BCC−body centered cubic, otherwise FCC lattices).

Structure	O1−Zn	O2−Zn	O1−C1	C1−C2	O1−Zn−O1
IRMOF-M0	2.088	2.072	1.307		
	SC 2.092	2.065	1.302		
IRMOF-1	2.092	2.072	1.316	1.464	109
	(1.941)	(1.922)	(1.301)	(1.486)	
	SC 2.085	2.092	1.319	1.460	115
	(1.941)	(1.922)	(1.301)	(1.486)	
	BCC 2.084	2.095	1.319	1.460	112−114
IRMOF-7	2.069	2.067	1.305	1.462	105−115
	(2.000)	(1.938)	(1.250)	(1.460)	
IRMOF-8	2.080	2.062	1.315	1.455	108−113
		(1.938)	(1.234)	(1.482)	
IRMOF-993	2.082	2.060	1.312	1.470	109
IRMOF-M1a	2.119	2.082	1.315	1.466	99−119

Continued

Table 4.1 – Continued

Structure	O1–Zn	O2–Zn	O1–C1	C1–C2	O1–Zn–O1
IRMOF-M1b	2.085	2.081	1.316	1.460	109–113
IRMOF-M4a	2.091	2.097	1.318	1.460	113–115
IRMOF-M4b	2.069	2.082	1.310	1.456	110–118
IRMOF-M2a	2.074	2.066	1.310	1.468	97–120
IRMOF-M2b	2.097	2.083	1.313	1.464	97–119
IRMOF-M2c	2.086	2.096	1.321	1.459	108–113
IRMOF-M3a	2.080	2.091	1.315	1.463	93–126
IRMOF-M3b	2.070	2.069	1.313	1.455	109–112
IRMOF-M3c	2.107	2.118	1.337	1.450	109–122
IRMOF-M3d	2.088	2.090	1.310	1.456	106–120
IRMOF-M6a	2.095	2.098	1.307	1.455	108–124
IRMOF-M6b	2.080	2.098	1.320	1.459	110–116
IRMOF-14	2.089	2.067	1.320	1.460	108
	(1.990)	(1.950)	(1.250)		
IRMOF-13	BCC 1.995	2.000	1.293	1.456	108
IRMOF-M7	2.060	2.085	1.316	1.451	109–113
IRMOF-M5	2.094	2.094	1.320	1.460	112–114
IRMOF-6	2.085	2.065	1.315	1.408	109
	(1.949)	(1.939)	(1.275)	(1.440)	
IRMOF-10	2.088	2.074	1.319	1.460	107
	(1.936)	(1.928)	(1.283)	(1.444)	
IRMOF-9	BCC 1.980	1.990	1.293	1.448	107
	(1.923)	(1.928)	(1.267)	(1.444)	
IRMOF-16	2.093	2.065	1.310	1.480	108
	(1.926)	(1.935)	(1.306)	(1.45)	
IRMOF-15	BCC 2.014	2.012	1.298	1.460	108
	(1.926)	(1.935)	(1.306)	(1.450)	
IRMOF-18	2.084	2.074	1.312	1.480	110–111
	(1.926)	(1.941)	(1.248)	(1.483)	
IRMOF-M8	2.075	2.086	1.319	1.460	108–114
IRMOF-M9	2.081	2.087	1.317	1.460	105–116
IRMOF-M10	2.081	2.078	1.310	1.494	109–112
IRMOF-M11	2.082	2.066	1.312	1.468	109
IRMOF-M13	2.099	2.076	1.312	1.496	109
IRMOF-M12a	2.062	2.216	1.313	1.490	114–129
IRMOF-M12b	2.105	2.184	1.314	1.489	115–122

Theoretical and experimental investigations agree in the fact that the O1−Zn bond length is a bit larger than that of O2−Zn in most of the cases. This tendency can be seen also for the hypothetical IRMOFs. Furthermore, it can be noticed that the O1−C1 distances correspond to values between those for a typical single and double O−C bond (1.42 Å and 1.22 Å, respectively), while C1−C2 bond lengths are close to the typical single $sp^2{-}sp^2$ C−C bond (∼1.46 Å).

We find, however, that the orientation of organic and inorganic rings [see Figure 4.5] changes significantly for different types of organic linkers, going from an in-plane to a perpendicular orientation with twisted forms in between. If the connector is not distorted, then the O1−C1−C2−C3 torsion angle is 180° (or 0°) and the value of the O1−Zn−O1 angle is fixed. This is typical for group 1 of organic linkers (see Section 4.1.1 for group definition). For linkers from group 3 the zinc-oxo carboxylato ring can be slightly distorted. In this case the O1−Zn−O1 angles vary in a small range and both, organic and inorganic, rings can be either in-plane or orthogonal to each other. A wide range of values for the O1−Zn−O1 angle and the twisted O1−C1−C2−C3 torsion angle is typical for a large distortion of the inorganic part (group 2 and 4).

Thus, both rings are in the same plane when the linker is symmetric and not extended into the inner space of a MOF crystal, like in IRMOF-1, IRMOF-8, IRMOF-14, IRMOF-M1b, etc. In the case of symmetric and functionalized linkers both rings are perpendicular to each other (IRMOF-18). Asymmetric and large symmetric linkers cause a distortion of the connector and a large variation of the O1−Zn−O1 angle distribution, depending on the size of the linker (IRMOF-M6a, IRMOF-M1a, IRMOF-M9, etc.).

Moreover, if both rings are in the same plane, then the O1−Zn−O1 angle is fixed at ∼109° or is slightly distorted (∼109−113°). The facts mentioned above show that the distortions of a connector (caused by some linkers) may lead to the lowering of the crystal symmetry. These systems can crystallize in other than cubic structures.

In case of IRMOF-9/10 (group 1) the benzene rings of the biphenyl linker might give different conformers. This may lead to a distortion of the inorganic part. However, benzene rings in these systems can be stacked, e.g. in the case of IRMOF-13/14. Such materials have not distorted connectors, similar to the group 1. A similar situation can be seen in the case of IRMOF-15/16.

The calculated equilibrium lattice constants (a) for all compounds studied here are given in Table 4.2. Experimental data exists only for some of the IRMOFs. These are given as well. The calculated lattice parameters were found to be in all cases slightly larger than those measured in the experiments. The error for a is in the range of 2−4%. Table 4.2 includes also the HOMO-LUMO gaps, bulk moduli ($\mathbf{B}$), mass densities (ρ) and energies of formation (ΔE) that will be discussed in the following sections. The mass densities of IRMOFs, besides IRMOF-M0, are considerably smaller than 1 g cm^{-3}.

Table 4.2: The calculated equilibrium lattice parameters ($a/2$), mass densities (ρ), band gaps (Δ), bulk moduli ($\mathbf{B}$), and the energies of formation (ΔE), of several $(OZn_4)^{6+}$-based IRMOFs with different linkers. Experimental values are given in parenthesis. A formation energy was calculated according to the Reaction (4.1). (SC−simple cubic, BCC−body centered cubic, otherwise FCC lattices).

Structure	$a/2$ [Å]	ρ [g cm^{-3}]	Δ [eV]	$\mathbf{B}$ [GPa]	ΔE [kJ mol^{-1}]
IRMOF-M0	9.152	1.182	4.17	24.3	−313.779
	SC 9.157	1.172	5.56	22.3	−303.731
IRMOF-1	13.440	0.527	3.73	8.70	−309.506
	(12.916)				
	SC 13.197	0.556	3.66	6.33	−294.140
	BCC 13.213				
IRMOF-7	13.343	0.643	2.77	3.70	−299.530
	(12.914)				
IRMOF-8	15.348	0.423	2.83	2.40	−299.768
	(15.046)				
IRMOF-993	13.463	0.728	2.16	3.60	−311.000
IRMOF-M1a	13.285	0.758	2.04	4.50	−291.361
IRMOF-M1b	17.761	0.317	2.13	3.20	−276.777
IRMOF-M4a	17.550	0.329	2.89	3.40	−296.877
IRMOF-M4b	15.318	0.495	2.67	1.50	−298.297
IRMOF-M2a	13.329	0.856	1.50	2.41	−295.186
IRMOF-M2b	13.279	0.865	1.56	6.90	−291.984
IRMOF-M2c	19.974	0.254	1.61	2.00	−303.469

Continued

Table 4.2 – Continued

Structure	$a/2$ [Å]	ρ [g cm^{-3}]	Δ [eV]	**B** [GPa]	ΔE [kJ mol^{-1}]
IRMOF-M3a	13.202	0.881	2.15	5.10	−287.275
IRMOF-M3b	19.767	0.262	2.39	2.60	−305.003
IRMOF-M3c	15.283	0.568	2.22	3.00	−292.456
IRMOF-M3d	17.740	0.363	2.25	1.10	−263.769
IRMOF-M6a	15.370	0.522	2.11	1.70	−293.214
IRMOF-M6b	15.591	0.501	2.28	3.40	−301.428
IRMOF-14	17.693 (17.190)	0.342	2.63	5.90	−308.395
IRMOF-13	BCC 17.661	0.689	2.62	9.70	−254.333
IRMOF-M7	19.653	0.267	2.65	0.30	−300.142
IRMOF-M5	17.601	0.372	2.90	4.20	−297.322
IRMOF-6	13.516 (12.921)	0.570	3.35	12.41	−304.097
IRMOF-10	17.674 (17.140)	0.300	3.07	6.00	−306.048
IRMOF-9	BCC 17.486	0.620	3.15	9.80	−287.373
IRMOF-16	22.012 (21.490)	0.191	3.06	7.50	−283.098
IRMOF-15	BCC 22.024 (21.459)	0.382	2.94	7.90	−306.582
IRMOF-18	13.382 (12.807)	0.650	4.28	5.00	−338.050
IRMOF-M8	16.814	0.267	2.66	3.50	−297.809
IRMOF-M9	17.857	0.419	2.38	4.40	−297.644
IRMOF-M10	13.252	0.927	4.56	9.20	−314.160
IRMOF-M11	13.334	0.594	4.91	12.6	−313.601
IRMOF-M13	15.078	0.638	5.49	9.00	−309.196
IRMOF-M12a	18.717	0.781	1.32		−233.291
IRMOF-M12b	18.717	0.768	1.31		−289.234

4.1.3 Energetic and Mechanical Stability

To compare the stability of the investigated MOFs, a formation energy (ΔE) has been estimated as the difference in total energies of the products and reactants, according to the following reaction:

$$\mathrm{Zn_4O(OH)_6 + 3R(COOH)_2 \longrightarrow Zn_4OR_3(COO)_6 + 6H_2O} \qquad (4.1)$$

The calculated formation energies are shown in Table 4.2. All values are negative, which suggests that energetically a formation of these structures is favorable.

The most stable structure, concerning ΔE, is IRMOF-18 that contains as organic linker a benzene ring functionalized by four methyl groups (2, 3, 5, 6-tetramethyl-benzene-1, 4-dicarboxylate). These linkers are arranged in a conformation, in which the steric repulsion between both rings is minimized. This suggests that the functionalization of the linker is one of the factors that can stabilize the system. Moreover, the results show that only for longer linkers the BCC structures are more stable than the corresponding FCC structures, due to steric hindrance effects. Also, it can be noticed that different isomers of the same linker have similar energies of formation (e.g. IRMOF-M4a and -M4b). Generally, the formation energy depends strongly on the size and the shape of the organic linker.

The mechanical properties were also estimated and the results are given in Table 4.2, as well. The structures are held together by strong Zn−O1−C bonds. The linkage between the Zn_4O2 group and the organic moieties results in rather soft materials with relatively small bulk moduli, as compared to cubic diamond (theory:[83] 441−457 GPa, exp.:[132] 443 GPa) and the wurtzite structure of zinc oxide (theory:[133] 160 GPa, exp.:[134] 183 GPa). The calculated values of $\mathbf{B}$ indicate that IRMOFs are easily compressible systems. Since the inorganic basic system ZnO has a much larger bulk modulus, the lowering of $\mathbf{B}$ in the MOFs is caused by the introduction of the linker molecules. The most rigid system is therefore the reference system IRMOF-M0. It can also be shown that the bulk moduli depend significantly on the length of the linker. A longer linker gives a mechanically less resistant system. The largest values of $\mathbf{B}$ belong to IRMOFs with hypothetical linkers based on the cage-like structures. Also, the results show that the BCC structures are more stiff than the corresponding FCC systems.

Furthermore, the organic linkers can rotate freely in the solid MOF at ambient conditions. The calculated energy barrier of a linker rotation (ΔE_{rot})

in IRMOF-1 along the connection axis is ∼0.35 eV. Thus, the rotation of the linker can be thermally activated, which has been observed also in MD simulations. The nearly free rotation of the linker was observed in these simulations already at room temperature. The simulations at 1200 K indicate, moreover, a good thermal stability of the investigated MOFs.

4.1.4 Electronic Properties

Charge distribution

In this section, the charge distributions of the studied MOFs are analyzed. The results of extended crystals were compared to those of the free building blocks. The calculated Mulliken atomic charges (q) of the MOF systems are summarized in Table 4.3. These results show that the studied metal-organic frameworks with different organic linkers have in all cases an almost unchanged charge distribution. Moreover, the solid structures keep nearly the same charges as the free linkers and connector.

Table 4.3: *The calculated atomic charges (q [e]) of the linker and the connector atoms of selected MOFs. C(−H) indicates the carbon atoms of the linker that are saturated by H atoms. C(−CH) denotes the carbon atoms of the linker that are connected to C(−H) carbon atoms [as an example see carbon C4 in Figure 4.5 (b)].*

Structure	C(−H)	C2	C(−CH)	Zn	O1	O2	C1
IRMOF-M0				0.92	−0.70	−0.88	0.92
IRMOF-1	−0.08	0.01		0.93	−0.73	−0.88	0.92
IRMOF-7	−0.12, −0.07	∼0.0	0.04	0.92	−0.75	−0.90	0.92
IRMOF-8	−0.10, −0.07	−0.01	0.04	0.92	−0.75	−0.93	0.92
IRMOF-993	−0.11	−0.01	0.04	0.91	−0.72	−0.88	0.93
IRMOF-M1a	−0.12, −0.07	∼0.0	0.04	0.94	−0.75	−0.94	0.92
IRMOF-M1b	−0.11, −0.06	−0.03	0.04	0.92	−0.74	−0.93	0.92
IRMOF-M2c	−0.11, −0.06	−0.02	0.03	0.92	−0.74	−0.96	0.92
IRMOF-18		−0.05		0.92	−0.72	−0.91	0.95
IRMOF-M8	−0.10, −0.05	−0.02	0.04	0.93	−0.77	−0.91	0.92
IRMOF-M9	−0.12, −0.08	−0.03	0.03	0.92	−0.75	−0.97	0.92
IRMOF-M11	−0.11, −0.08	−0.01		0.91	−0.72	−0.88	0.93

The Zn atoms are positively charged ($q = +0.92$). This value is in between $q = +1.09$ and $q = +0.82$, which correspond to charges of the Zn atom in the free connector [Figure 4.7] and the bulk ZnO (wurtzite) structure, respectively. The oxygen atoms O1 and O2 are both negatively charged with $q = -0.70 \ldots -0.77$ and $q = -0.88 \ldots -0.97$, respectively. In the free connector, the O1 and O2 atoms are charged with $q = -0.92$ and $q = -1.26$, respectively. Both values are larger by ≈0.25 than the corresponding charges in the MOF crystal. On the other hand, the charge of −0.82 for the oxygen atoms in bulk ZnO is slightly smaller than that for the equivalent O2 atom in the MOFs. In the free linker [dicarboxylate linker; Figure 4.7] one can distinguish between the O1 atoms connected to the C1 atoms with a double bond and the O1 atoms of the hydroxyl group. The charge of O1 in the first case is −1.02 and in the other one −0.35. Thus, the charge of the O1 atom in the MOF crystal is averaged over the corresponding charges in the free linker. The C1 atoms, which bind the linker and the connector together, are positively charged with $q = +0.92$ and this value does not change for structures with different linkers. Carbon atoms bound to hydrogen atoms (C(−H)) are slightly negatively charged ($q = -0.11$ and $q = -0.07$). C2 atoms have charges close to zero in all cases. Generally, the carbon atoms in the free linker and the MOF crystal have the same charge distribution.

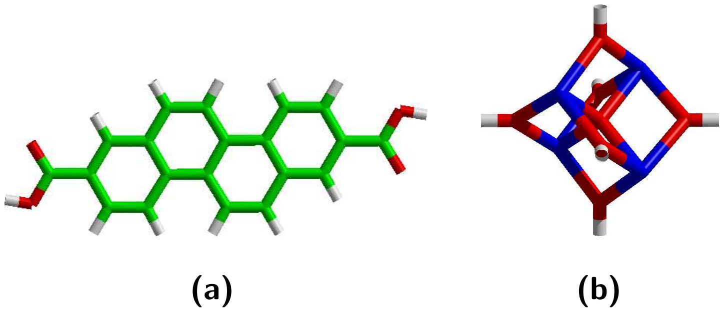

(a) **(b)**

Figure 4.7: *The structures of the free building blocks: (a) the example linker for IRMOF-M7 and (b) the connector.*

Densities of States

The partial and total densities of states (PDOS' and TDOS') of MOF systems studied in this work were compared to PDOS' of the free linkers and the free connector. The carbon PDOS of the free building blocks nearly does not change compared to the MOF crystals. On the other hand, the oxygen PDOS differs in both cases. In an extended MOF there is one type of O1, whereas in the free linker there are two types (cf. Section 'Charge Distribution'). The PDOS of the zinc atoms in the free connector is very similar to those of the bulk ZnO wurtzite and an extended MOF. This can be expected, as the inorganic part in IRMOFs mimics a fragment of the bulk ZnO wurtzite [see Figure 4.8]. The overall electronic properties of IRMOFs are basically characterized by the properties of $(\mathrm{Zn1})_4(\mathrm{O2})$ clusters that bring to the systems the character of a wide band gap semiconductor. This can be understood, since bulk ZnO wurtzite is a semiconductor with a band gap of 3.37 eV. On the other hand, the organic linkers (especially PAHs) reduce the gap size.

IRMOF-M0 was chosen as a reference system to analyze the differences in the electronic properties for different organic linkers in MOFs. The PDOS of IRMOF-M0 (for different states of a given atom) shows that the valence band is composed of the Zn $3d$ states, the O $2p$ and the C $2p$ states. The unoccupied band is determined by s and p states of the Zn atoms, and the p states of the O and C atoms. Similar electronic properties are found for IRMOF-1 [Figure 4.9], which is also in agreement with the results of the earlier work of Fuentes-Cabrera et al.[125]

Figures 4.10 and 4.11 show the PDOS' of MOFs with differently sized polycyclic hydrocarbon molecules. These are compared with the PDOS of the reference system and IRMOF-M11 (cubane-based linker). The values of the band gaps for different linkers are summarized in Table 4.2. MOFs have band gaps in the range of 1.0/-5.5 eV. That means they cross the borderline between insulating and semiconducting materials. A size dependence of the band gaps for different linkers was found. Smaller values are observed for linkers with larger numbers of carbon atoms. Band gaps are determined by the π states and the number of sp^2 C atoms. It can be seen from Figure 4.10

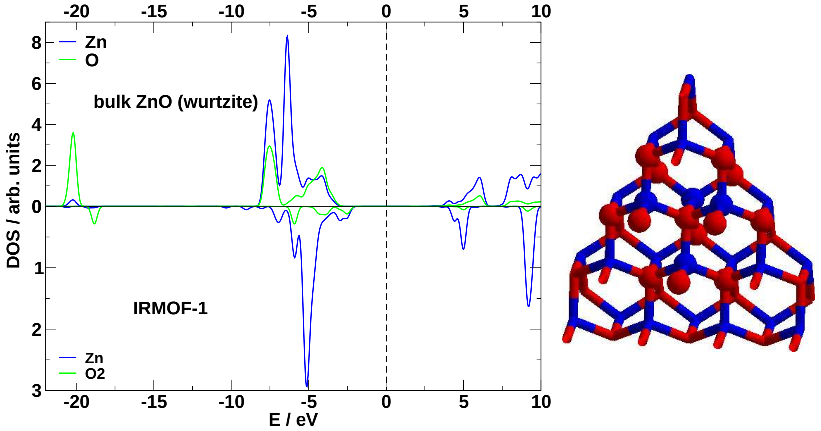

(a) (b)

Figure 4.8: *(a) The partial densities of states of the bulk ZnO wurtzite and the free IRMOF-1 connector. For clarity only Zn and O2 states of IRMOF-1 [Figure 4.3] are shown. The Fermi level is shifted to 0.0 eV (vertical dashed line). (b) The fragment of the bulk ZnO wurtzite with a highlighted fragment of the connector. Note the different scalings on the y axes.*

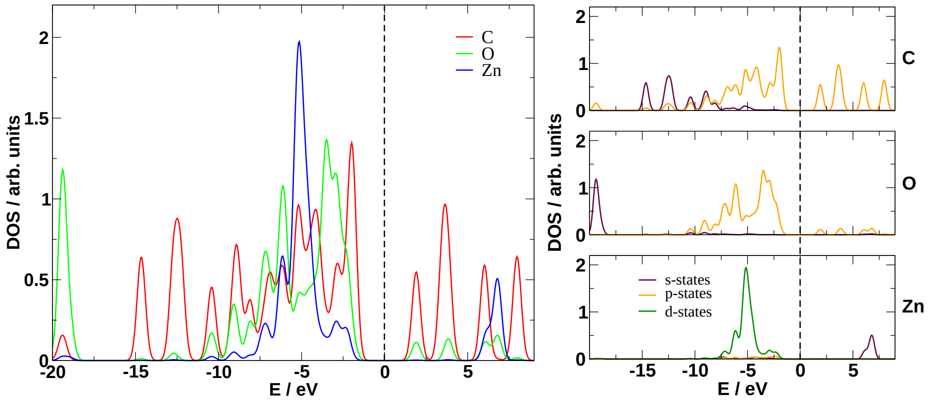

(a) (b)

Figure 4.9: *(a) The partial densities of states for the C, O and Zn atoms in IRMOF-1. (b) The PDOS' of s, p and d states of each element. The Fermi level is shifted to 0.0 eV (vertical dashed line).*

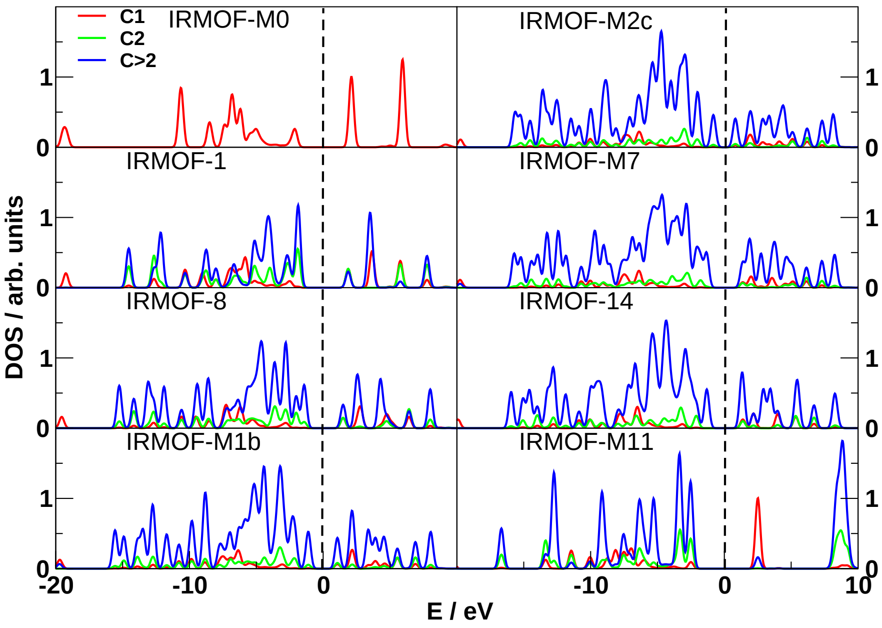

Figure 4.10: *The partial densities of states of C atoms in the example structures and IRMOF-M0. The Fermi level is shifted to 0.0 eV (vertical dashed line). For numbering of the atoms see Figure 4.5.*

that the band gaps decrease with increasing number of sp^2 carbons in the linker. The top of the valence band and the bottom of the conduction band are both dominated by the π states of these atoms. Systems with cage-like linkers (e.g. IRMOF-M11 or IRMOF-M13) and IRMOF-M0 have large band gaps due to the lack of the sp^2 C atoms.

In all cases, adding the organic linker causes a shift of the O1 p states compared to the reference system [Figure 4.11]. The peak is shifted to lower energies relative to Fermi level (E_F). On the other hand, the central O2 atom in the connector has an unchanged density of states for different linkers. These differences in the electronic structures of O1 and O2 might be explained by the fact that the O1 atom is involved in an sp^2-like bonding with atom C1, whereas O2 is sp^3 hybridized and connected to four surrounding Zn atoms. The peaks of the Zn 3d states are also shifted to lower energies relative to E_F [Figure 4.11].

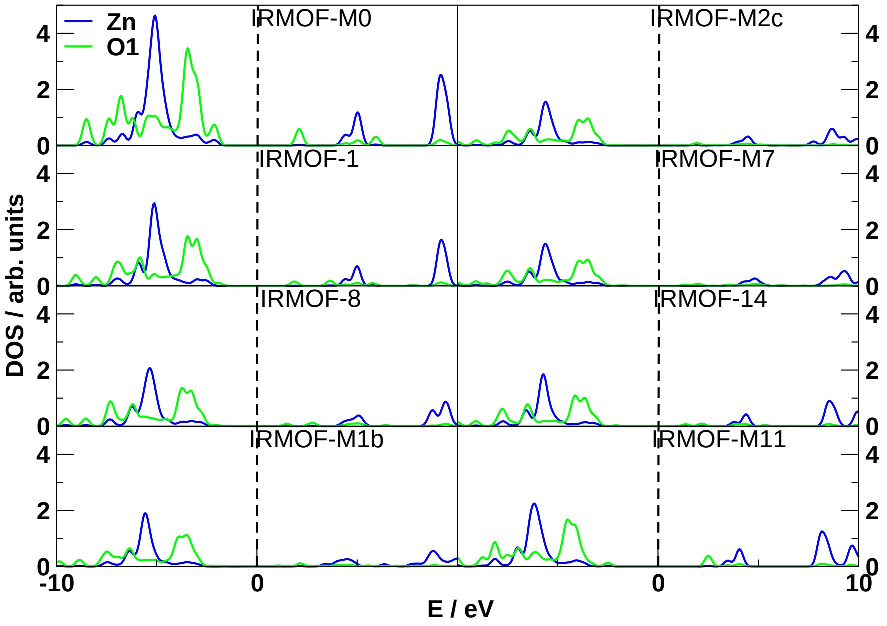

Figure 4.11: *The partial densities of states of Zn atoms in the example structures and IRMOF-M0. The O1 p states are shown as well. The Fermi level is shifted to 0.0 eV (vertical dashed line).*

4.2 A Cu-Based Metal-Organic Framework

By exchanging the metal atom in the connector topologically distinct crystal structures may be obtained. This section is focused on the properties of a MOF material which contains copper atoms in the connector, $Cu_3(BTC)_2(H_2O)_3$ (BTC: benzene-1,3,5-tricarboxylate; in the remainder Cu-BTC will be used). The structure and SEM image of Cu-BTC are shown in Figure 4.1 (b). The connector contains a Cu-Cu dimer. Each metal atom completes its pseudooctahedral coordination sphere with four oxygen atoms in a square plane and one Cu atom and an axial aqua ligand on the tops of the octahedron.

At first, this crystal was described by Chui et al.[115] The synthesis of this material was then further improved by others.[33] Recently, several groups investigated a potential use of Cu-BTC for gas purification, separation and storage,[124,135] due to the possibility of forming 'open' metal sites.

All the calculations presented in this section were performed similarly to those of the Zn-based MOFs, as it is described in Section 4.1.1.

4.2.1 Structure

Although Cu-BTC forms a cubic lattice, the architecture is significantly different from those of Zn-based MOFs presented in Section 4.1. In Figure 4.12 the structure of Cu-BTC is shown together with its building block. This material has a bimodal pore size distribution.[136] A first larger pore system [Figure 4.12 (a)] is built up from 12 $Cu_2(COO)_4$ moieties, so-called paddle-wheel units [see Figure 4.12 (b)], forming a cuboctahedron. Four carboxylate groups of the paddle-wheel are arranged in a square. One of the copper coordinating water molecules points towards the center of the pore. Experimental investigations emphasize that water molecules bound with Cu^{2+} ions can be easily removed in vacuum. This might create 'open' copper sites for catalytic transformations.[33] A second pore system [Figure 4.12 (a)], accessible from the larger pores, is built up from four benzene rings that form the inner surface. The centers of the rings form a tetrahedron with triangular windows of three copper ions. A view along the [100] direction of the cubic cell of Cu-BTC in Figure 4.12 (a) reveals channels with

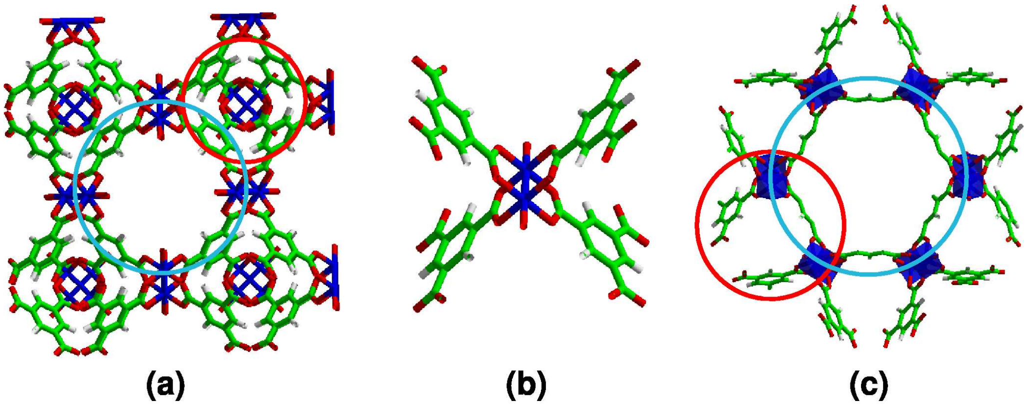

Figure 4.12: *(a) The structure of $Cu_3(BTC)_2(H_2O)_3$ (Cu-BTC) viewed along the [100] direction: blue and red circles indicate larger (square-shaped) and smaller (triangular-shaped) pore systems, respectively. (b) The building block of Cu-BTC, so-called Cu_2-paddle-wheel. (c) Cu-BTC viewed along the [111] direction reveals a hexagonal-shaped (blue) window at the intersection of the nanopores. For clarity H atoms of ligand water molecules are omitted. Blue, red, white and green represent Cu, O, H and C atoms, respectively.*

four-fold symmetry. On the other hand, a view along the cell body diagonal [111], shown in Figure 4.12 (c), reveals a honey-comb arrangement of large hexagonal-shaped windows at the intersections of both types of pore systems.

The optimized geometry of the Cu-BTC system agrees well with the reported experimental findings (see Table 4.4). In detail, the vertical and diagonal Cu−Cu distances of the fourfold symmetry channels are 16.43 Å and 11.65 Å, respectively. This is in very good agreement with reported experimental values of 16.0 Å and 11.3 Å.[33] The same geometry was obtained for the oxygen atoms of the water molecules but the corresponding O−O distances across the pore are 12.3 Å and 8.75 Å (exp.: 11.67 Å and 8.25 Å), respectively. The diameter of the hexagonal-shaped windows is 18.85 Å, while the intersecting 3D system of the large square-shaped pores is 9.65 Å by 9.65 Å. The smaller triangular window is indicated by three copper ions 8.22 Å apart from each other.

The agreement between calculated and experimental Cu−O distances is

Table 4.4: *The selected calculated and experimental bond lengths [Å], unit cell parameters (a [Å]), and the pore sizes [Å] of Cu-BTC structure. The mass densities (ρ [g cm^{-3}]) and the bulk moduli (**B** [GPa]) are given, as well.*

property	theory	theory (no H_2O)	experiment
a	26.661	26.748	26.343
Cu−Cu	2.415	2.467	2.628
Cu−O(CO)	2.020	2.017	1.952
Cu−O(H_2O)	2.065		2.165
(O)C−C(C)	1.450	1.450	1.500
O−C	1.334	1.347	1.252
Cu−Cu$_{\text{diag}}$	16.43	16.45	16.0
Cu−Cu$_{\text{vertic}}$	11.65	11.63	11.3
(H_2O)O−O$_{\text{diag}}$	12.30		11.67
(H_2O)O−O$_{\text{vertic}}$	8.75		8.25
Cu−Cu$_{\text{triangle}}$	8.22	8.17	8.0
hexagonal$_{\text{diameter}}$	18.85	19.07	18.6
square$_{\text{vertic}}$	9.65	9.65	9.5
ρ	0.92	0.84	0.96
B		18.8	

good (ΔR ~2−4 %). However, the Cu−Cu distance is somewhat smaller than the experimental findings. The Cu−O bond length with the oxygen atom from the carboxylate groups is shorter than that with the oxygen atoms from the water molecules, indicating that the latter is only weakly bound to the copper ions. The O−C distances (1.33 Å) correspond to values between that for the typical single (1.42 Å) and double (1.22 Å) oxygen-carbon bond. The calculated C$_{\text{ring}}$−C$_{\text{carboxyl}}$ bond lengths of 1.45 Å indicate that these are typical single sp^2−sp^2 C−C bonds (~1.46 Å), while experimental findings give a slightly longer value (1.5 Å). The results obtained for the Cu-BTC structure, in which the ligand water molecules were removed, are about the same or slightly larger (~1 %) than those for the system with water coordinated to the copper atoms (see Table 4.4).

As it was shown by theoretical investigations,[22] the optimum pore size for hydrogen adsorption in slit-pore materials should be around 7 Å. In conclusion, the geometry of the Cu-BTC structure, namely the smaller triangular windows with the edges of around 8 Å, makes the material a good candidate for hydrogen storage. These smaller pores should be accessible for adsorbates as small as H_2 molecules and should favor an effective packing of the gas due to the presence of the benzene rings. Moreover, this material has a very low mass density of only 0.92 g cm^{-3}, which drops down to only 0.84 g cm^{-3} when the crystal is water-free.

The Cu-BTC structure free of the water ligands has a bulk modulus of 18.8 GPa, which makes it a rather soft material. On the other hand, this number is higher than these of the Zn-based MOFs. Although Cu-BTC is energetically stable, the calculated value of **B** still indicates that it is an easily compressible system. This might affect the structure during (un)loading of gas under high pressure.

For hydrogen storage applications more attractive is the material without coordinated water molecules, thus in the following only this strcture is discussed.

4.2.2 Electronic Properties

The electronic properties were studied by analyzing the charge distribution and the density of states, similarly to the Zn-based MOFs. The calculated atomic Mulliken charges of Cu-BTC are as follows: The copper atoms are positively charged ($q = +1.75$). The oxygen atoms of the carboxyl groups (O1 in notation adopted from the Zn-based MOFs) are negatively charged with $q = -0.68 \ldots - 0.90$. The carbon atoms of the carboxyl groups (C1) in the organic linkers are positively charged with $q = +0.70$, while other carbon atoms have charges close to zero.

The density of states of Cu-BTC was compared with that of Tenorite, as the inorganic connector is similar to a part of this CuO crystal [see Figure 4.13]. Tenorite with a band gap of approximately 2.0 eV (experimental value) is considered as a direct-gap semiconductor.[137–139] Theoretical calculations of its band structure show that the system has a character of a semiconductor-like structure with a direct gap of 1.6 eV at the Γ point.[140] There is a Fermi surface present with the top of valence band (VB) 0.95 eV

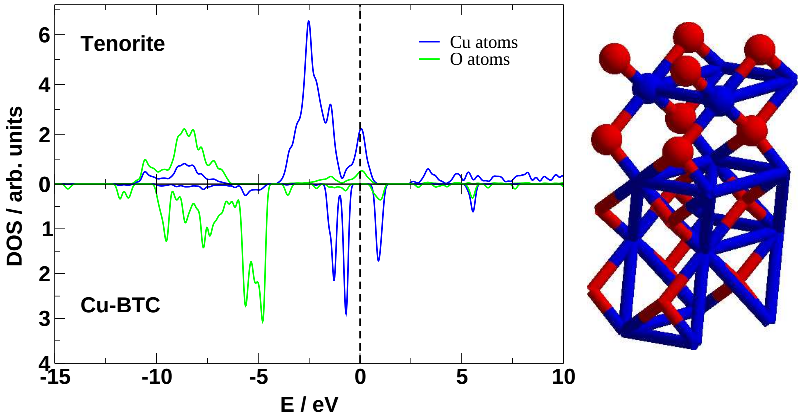

(a) (b)

Figure 4.13: *(a) The partial densities of states of Cu-BTC and Tenorite. For clarity only the states of the Cu and O atoms in Cu-BTC are shown. (b) The fragment of the Tenorite crystal with a highlighted fragment of the connector used in Cu-BTC. The Fermi level is shifted to 0.0 eV (vertical dashed line). Note the different scalings on the y axes.*

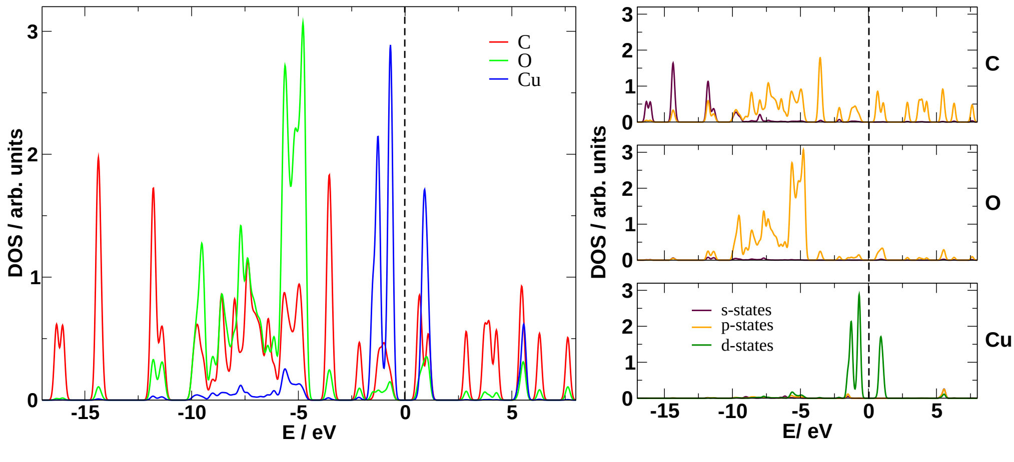

(a) (b)

Figure 4.14: *(a) The partial densities of states for C, O and Cu atoms in Cu-BTC. (b) The PDOS of s, p and d states for each element are shown. The Fermi level is shifted to 0.0 eV (vertical dashed line).*

above the Fermi level (E_F) and the bottom of conduction band (CB) 2.55 eV above E_F. This also can be seen in the DOS of Tenorite [see Figure 4.13 (a)]. The partial density of states of Cu-BTC differs, however, significantly from that of Teronite. The band gap is shifted to be centered at E_F. The results reveal that Cu-BTC with the band gap of 0.96 eV (1.35 eV for structure with coordinated water) is a semiconducting material. However, this value is smaller than those of the Zn-based MOFs.

Partial densities of states of each element in Cu-BTC are shown in Figure 4.14. Copper and oxygen atoms bring to the structure the character of a semiconductor (similarly to Tenorite), while the $2p$ states of the carbon atoms decrease the band gap. In the VB and CB the states are dominated by the $3d$ states of copper and the $2p$ states of the C and O atoms. Obviously, the introduction of organic linkers in Cu-BTC significantly changes the DOS compared to Tenorite.

4.3 Interactions between H_2 and Metal-Organic Frameworks

Metal-organic frameworks have been intensively studied both experimentally and theoretically as hydrogen storage media over the past few years. The first reported computations on the gas adsorption in MOFs were performed by Kawakami et al.[141] They have studied adsorption of N_2, CO_2, Ar, H_2 and O_2 in IRMOF-1 using *ab initio* methods and Monte Carlo (MC) simulations. The predicted amounts of adsorbed gas were, however, significantly higher (1.7 to 3 times) than the experimental findings.[142] The authors attributed these differences to defects in the experimental materials.

Since this time a large number of theoretical works on gas adsorption in MOFs has appeared in the literature. Three main groups of simulations have to be mentioned: Monte Carlo, in particular Grand Canonical MC (GCMC), density-functional theory (DFT) based methods, and post-Hartree-Fock (HF) methods, like e.g. MP2 (second order Møller-Plesset) perturbation theory, CCSD (coupled cluster restricted to single and double excitations), CI (configuration interaction), etc.

It has been shown experimentally that some MOFs show indeed large hydrogen storage capacities:[36,118,120,143] 4.5 wt% (78 K and 0.7 bar) in IRMOF-1, 2.0 wt% (298 K and 10 bar) in IRMOF-8 or 7.5 wt% (77 K and 70 bar) in MOF-177. It is, however, unclear which mechanism is responsible for this property. The fundamental interactions underlying the H_2 adsorption in metal-organic frameworks have to be well understood in order to tune the storage capacity of these materials. So far, it is not clear which interaction (London dispersion or electrostatics) is mainly responsible for the H_2 physisorption in MOFs. Experiments emphasize that the strongest H_2 adsorption sites are close to the metal oxide connectors.[144,145] This is interpreted in such a way that metal cations form M−O (M = Zn, Cu, Mg, etc.) dipoles, whose charges are most effective in polarizing the gas molecules leading to strong interactions.[37]

However, the adsorption mechanism and even the adsorption energy are matter of discussion. In agreement, theory and experiment have identified the low-energy adsorption sites,[145] but there is no agreement in quantification of the guest-host interaction potential. As this potential can not be accessed in the experiment, it is important to employ theoretical calculations. But also the theoretical determination is not straight-forward: A good model for the H_2-MOF system can be proposed, but the energies are calculated with DFT,[145–147] which is feasible to effort large systems but fails to correctly describe London dispersion interactions.[148,149] On the other hand, the MOF structure can be reduced to independent model clusters (connectors and linkers) and the guest-host interaction can then be calculated at a higher computational level (e.g. MP2) with a correct treatment of the London dispersion.[150–155] However, with this second approach controversial results have been obtained: In consensus, the interaction energy of H_2 with organic linkers is pure London dispersion and has been determined[146,150,154] to be 3.5−5 kJ mol^{-1}, but values reported for the interaction energy of H_2 with the zinc oxide connector of IRMOF-1 vary much stronger,[150,151] between 2 and 7 kJ mol^{-1}. More important, different origins of the interaction have been suggested, namely dipole-induced dipole interactions[155] and weak London dispersion.[151]

In order to determine the H_2-MOF potential energy surface in future, a better qualitative understanding of the fundamental non-bonding interactions between H_2 and MOFs (London dispersion and induced electrostatic effects) is needed. Furthermore, the discrepancies found in the literature should be resolved. Below, a wide range of detailed high-level calculations is covered, in order to determine an accurate treatment of weakly bound H_2 in MOFs.[156,157] The results allow a more detailed understanding of the H_2-MOF interactions and can possibly suggest better strategies to optimize MOFs with higher H_2 storage capacities. The most widely investigated IRMOF-1 was chosen as a benchmark system.

4.3.1 Model Structures and Validity of Methods

The accurate calculation of the H_2 interactions with MOF structures requires the representation of the extended system [Figure 4.15 (a)] with smaller model structures. The models studied in this work for the IRMOF-1 are shown in Figure 4.15 (b)−(c). The $Zn_4O(HCO_2)_6$ cluster [Figure 4.15 (b)] was used to model the connector and $C_6H_4(COOH)_2$ [benzene-1,4-dicarboxylate, Figure 4.15 (c)] for the linker. The connector can be viewed as tetrahedral arrangement of Zn atoms around the central O atom and four distorted tetrahedral of ZnO_4 moieties. The high-symmetry adsorption sites, proposed from neutron scattering experiments,[144,145] are also indicated in Figure 4.15 (a). In the remainder of this section, α and β will denote sites at the connector and δ and ε will denote sites at the linker. The α site lies on a triangular face of the octahedron. Its vertics are defined by the carbon atoms of the carboxylate groups. The β site is above a face of the $ZnO2(O1)_3$ tetrahedron. The δ site lies on the top of the benzene ring, and finally the ε site is at the edge of the ring. The considered H_2 orientations on each adsorption site and the model nomenclature used in the text are shown in Figure 4.16.

A major task of this section is to attribute the interaction energy between H_2 and the MOFs to London dispersion and to electrostatic interactions. It is well known that London dispersion, which gives an important contribution to the physisorption energy of weakly bound systems, is a correlation phenomenon, and therefore not included in the HF method. HF does account,

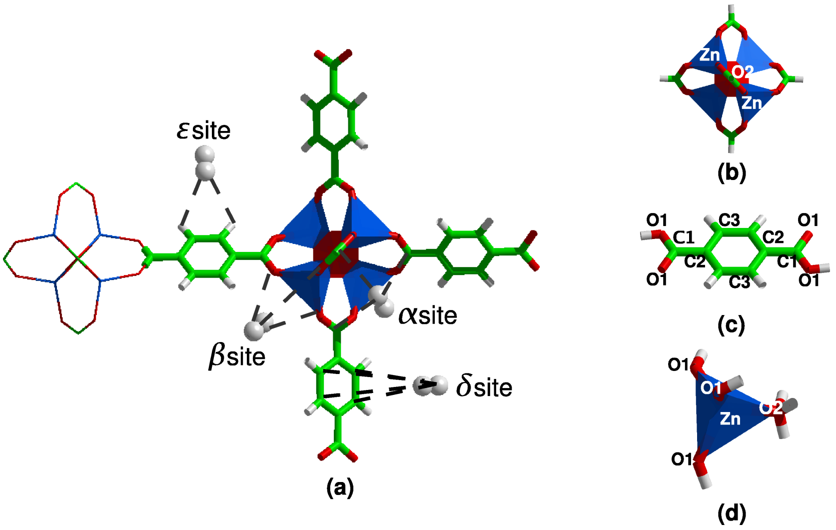

Figure 4.15: *(a) The considered adsorption sites within the IRMOF-1 unit cell and the used model systems: (b) the connector* $Zn_4O(HCO_2)_6$*, (c) the linker* $C_6H_4(COOH)_2$*, and (d) the alternative connector model* ZnO_4H_6*. The numbering of the atoms used in the text is shown, as well.*

however, correctly for electrostatic interactions (charge-dipole, dipole-dipole, dipole-induced dipole) and Pauli repulsion. The long-range interaction is also poorly described in the presently available exchange-correlation functionals in DFT.[149] Nevertheless, a large number of DFT calculations of the H_2-MOF interactions has been performed,[145–147,158–163] using the full MOF unit cell. Storage capacities need to account for the mobility of H_2, which is beyond the applicability of DFT. DFT is, however, capable to predict the low-energy adsorption sites. The results (see Tables 4.5 and 4.6) show that for the gradient-corrected hybrid functional PBE0[164] the distances between the molecular centers are close to the equilibrium, whereas the interaction energies are far from the correct values. The long-range interaction is, however, correctly included in the post-Hartree-Fock methods that properly treat correlation effects. MP2 is a method which is feasible to treat the systems discussed in this section, also with larger basis sets, and still providing sufficient accuracy. As it will be shown below, a high accuracy can only be achieved if the interaction energies are corrected for basis set superposition

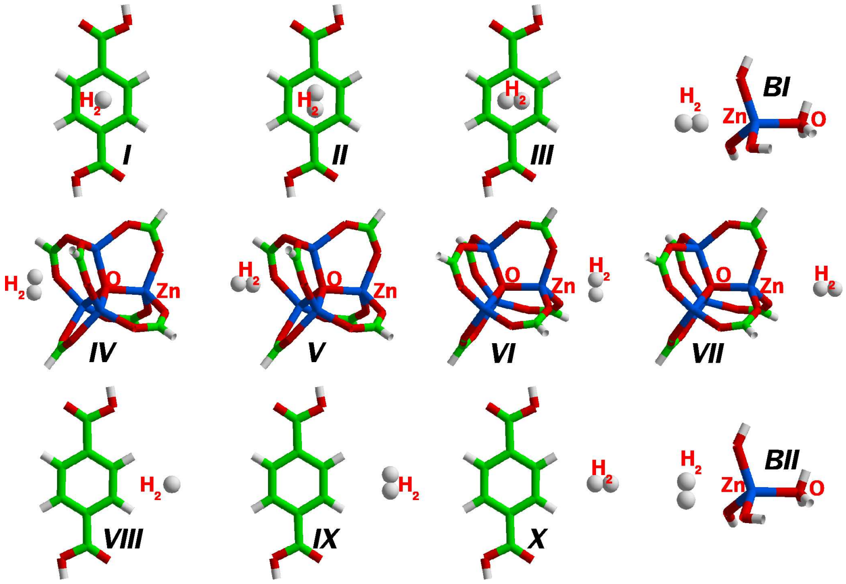

Figure 4.16: *Model structures and considered H_2 orientations:* ***I–III*** *and* ***VIII–X*** *for the linker,* ***IV– VII*** *for the larger connector and* ***BI–BII*** *for the benchmark connector.*

errors (BSSE):[165]

$$\Delta E_{\text{int}}^{\text{BSSE}} = E_{AB}\,(AB) - \left[E_A\,(AB) + E_B\,(AB)\right] \tag{4.2}$$

where $\Delta E_{\text{int}}^{\text{BSSE}}$ is the BSSE corrected interaction energy, the dimer AB is composed of the monomer A (H_2 molecule) and the monomer B (connector or linker), the used basis set is indicated in parentheses and E_i ($i = A, B, AB$) denotes the energies of each component.

The model structures have been optimized at the B3LYP/6-31G(d) level using the Gaussian03[166–169] code. The fragments have been kept fixed for the calculations of interaction energies between H_2 and the models of the IRMOF-1. Various high-level calculations available in the literature[22,49,51] agree that MP2 theory with moderately large basis sets can describe the weak interactions between a hydrogen molecule and systems similar to the nonpolar linker with sufficient accuracy. The top and bottom panel in Figures 4.17 (a) demonstrate that these findings apply also for MOF linkers (see also Table 4.5). They can be treated with good accuracy at the MP2/cc-pvTZ

Table 4.5: *Calculated interaction energies at the MP2 and DFT level, and equilibrium distances between the molecular centers of the H_2 molecule and the linker on the δ site.*

Method/Basis Set	ΔE_{int} [kJ mol^{-1}]	d [Å]	$\Delta E_{\text{int}}^{\text{BSSE}}$ [kJ mol^{-1}]	d [Å]
	Model I			
PBE/cc-pvTZ	1.30	3.4	1.14	3.45
SVWN5/cc-pvTZ	8.40	2.8	8.02	2.8
MP2/cc-pvDZ	3.50	3.2	1.70	3.4
MP2/cc-pvTZ	4.61	3.1	3.44	3.2
	Model II			
PBE/cc-pvTZ	0.79	3.45	0.68	3.45
SVWN5/cc-pvTZ	7.68	2.7	7.32	2.7
MP2/cc-pvDZ	1.76	3.2	0.65	3.5
MP2/cc-pvTZ	3.46	3.0	2.64	3.1
	Model III			
PBE/cc-pvTZ	0.98	3.4	0.83	3.4
MP2/cc-pvDZ	1.94	3.2	0.73	3.4
MP2/cc-pvTZ	3.73	3.0	2.87	3.1

level with the BSSE correction.

The interaction of H_2 with metal oxides is, however, less precisely investigated in the literature. The connector model, shown in Figure 4.15 (b), has too many electrons for a high-level calculation. Therefore, a smaller model, ZnO_4H_6 [Figure 4.15 (d)], has been chosen to benchmark the level of theory. This model can describe the physisorption of H_2, only at the β adsorption site. The basis set dependency of the MP2 results of the H_2 interaction with the ZnO_4H_6 model [Figure 4.16 **BI**] is shown in Figures 4.17 (top) (b)−(c). The corresponding results for other H_2 orientation [Figure 4.16 **BII**] are presented in Figures 4.17 (bottom) (b)−(c). The fast convergence of the BSSE-corrected interaction energies to a maximum value of 2.5 kJ mol^{-1} and 4.2 kJ mol^{-1} has been obtained, for the model **BI** and **BII**, respectively. On the other hand, the BSSE-uncorrected numbers strongly overestimate the interaction energies, with values which can be as large as 10 kJ mol^{-1}. It is well known that combined large and moderate basis sets can give meaningless results. The long-range polarization and diffuse functions increase the basis

Table 4.6: *Calculated interaction energies at the MP2 and DFT level, and equilibrium distances between the H_2 molecular center and the Zn atom of the ZnO_4H_6 connector on the β site.*

Method **Basis Set**	ΔE_{int} [kJ mol^{-1}]	d [Å]	$\Delta E_{\text{int}}^{\text{BSSE}}$ [kJ mol^{-1}]	d [Å]
	Model BI			
PBE/cc-pvTZ/6-31+G(2d,p)	3.74	3.8	2.25	4.0
SVWN5/cc-pvTZ/6-31+G(2d,p)	10.60	2.9	7.31	3.0
B3LYP/cc-pvTZ/6-31+G(2d,p)	2.54	4.2	1.26	4.7
cc-pvDZ-PP	4.29	3.1	2.19	4.1
cc-pvTZ-PP	6.25	3.1	2.35	4.0
cc-pvQZ-PP	5.32	3.1	2.46	3.9
aug-cc-pvDZ-PP	7.35	3.4	2.26	4.0
aug-cc-pvDZ/6-31+G(2d,p)	4.37	3.7	2.23	4.0
aug-cc-pvTZ-PP	5.11	3.6	2.45	3.9
aug-cc-pvTZ/6-31+G(2d,p)	7.33	3.2	2.40	3.9
aug-cc-pvQZ/6-31+G(2d,p)	8.95	3.2	2.46	3.9
	Model BII			
PBE/cc-pvTZ/6-31+G(2d,p)	5.52	2.9	2.22	3.0
SVWN5/cc-pvTZ/6-31+G(2d,p)	24.98	2.3	19.07	2.3
B3LYP/cc-pvTZ/6-31+G(2d,p)	2.86	3.2	−0.30	3.4
cc-pvDZ-PP	8.02	2.8	0.22	3.6
cc-pvTZ-PP	7.87	2.8	2.32	3.1
aug-cc-pvDZ-PP	10.14	2.8	2.85	3.1
aug-cc-pvDZ/6-31+G(2d,p)	6.76	2.9	2.92	3.1
aug-cc-pvTZ-PP	5.99	2.8	3.95	2.9
aug-cc-pvTZ/6-31+G(2d,p)	8.65	2.7	3.85	3.0
aug-cc-pvQZ-PP	5.57	2.8	4.33	2.9
aug-cc-pvQZ/6-31+G(2d,p)	10.77	2.6	4.17	2.9

set on the host to accommodate its electrons and result in a significantly lowered energy for the H_2-host system. Systematic investigations on the basis set size showed that for the aug-cc-pvTZ basis set[170] for C, O and H and the aug-cc-pVTZ-PP for Zn the BSSE-corrected interaction energies are in close agreement with the converged results (see Table 4.6), underestimated by only 0.2 kJ mol^{-1}.

To study the H_2 interaction with the described connector model [Figure 4.15 (b)] this level of theory is still too expensive. Therefore, the basis set for atoms far from the interaction site has been reduced to 6-31+G(2d,p) or even to 6-31G(d) bases. However, it is necessary to keep the large basis on H_2 and its closest neighbors to allow a high-level description of the weak interaction between the two moieties and to account for its polarizability and polarization. While the BSSE-uncorrected results are meaningless for weakly bound systems, the BSSE-corrected results are close to those of converged MP2 calculations with balanced basis sets (see Table 4.6). Therefore, this computational strategy can be safely adopted in the remainder of this section.

Considering the electrostatic effects, the strongest polarization of H_2 has been expected, if the hydrogen molecule lies on the axis of the central Zn−O bond of the connector [see Figure 4.16 **BI**]. Figure 4.17 (d) of the top panel shows the H_2-connector interactions for **BI** at the basis set converged HF level of theory. Assuming that the total interaction (resulting from MP2) is only London dispersion and electrostatic interactions, the HF results should account for the latter one, as London dispersion is not included here. Indeed, with this assumption the electrostatics account for about 50% of the total interaction energy in this orientation. This large amount is, however, an artifact of the small benchmark model: the total interaction is weak (around 2.5 kJ mol^{-1}) and the system has a relatively high dipole moment due to the influence of the terminal hydroxyl groups. Results for the perpendicular orientation [see Figure 4.16 **BII**] indicate no electrostatic interaction, as the interaction energy at the HF level of calculations is negligible [Figure 4.17 (d) of the bottom panel]. It is worth to point out, that the total interaction energy (MP2 results) is stronger for **BII** than for **BI**, even though it is based almost exclusively on London dispersion. The overestimated interac-

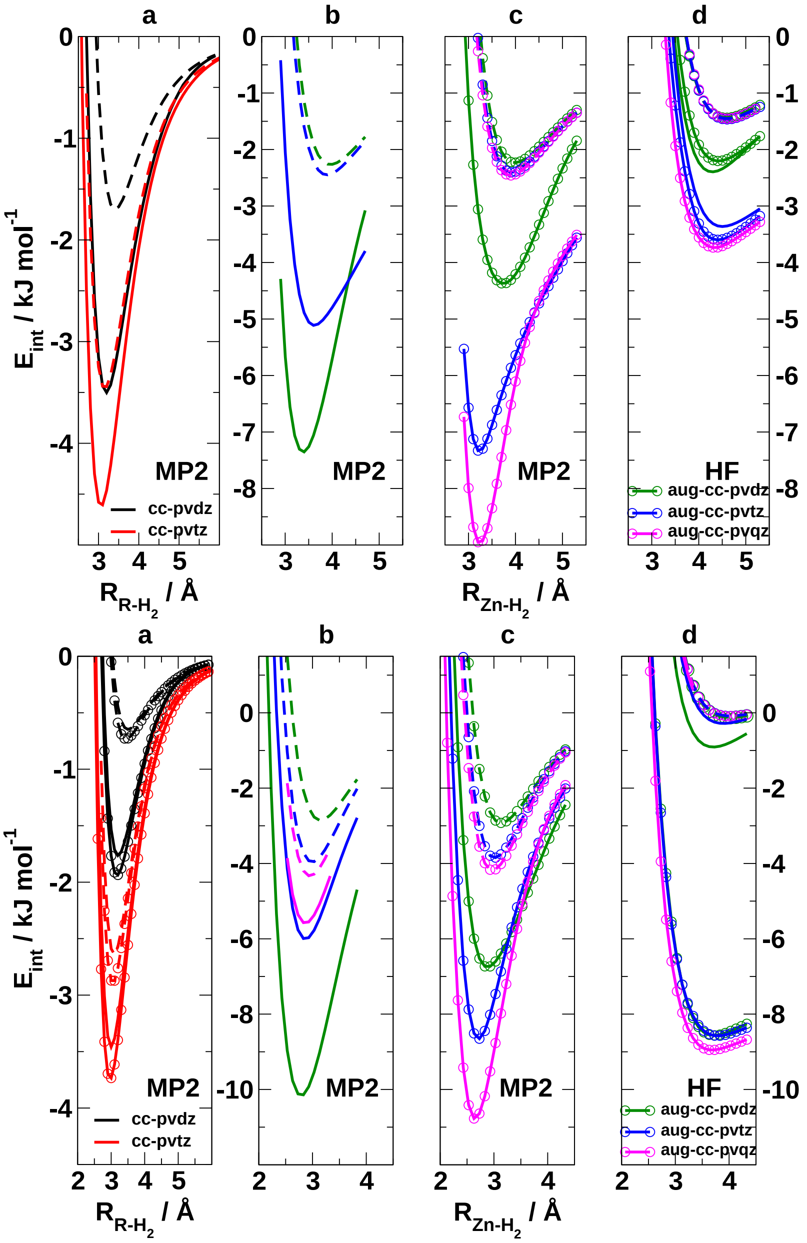

Figure 4.17: *The potential energy curves of H_2 on (a) the linker and (b-c) the connector; top panels: model **I** and **BI** [see Figure 4.16]; bottom panels: models **II**, **III** and **BII** at MP2 (a-c) and HF (d) levels. Solid lines give the relative energy of the adsorbed with respect to the dissociated systems. Dashed lines denote those results corrected for BSSE. Basis sets are given in the plots, (c) shows results where small basis sets (6-31+G(2d,p)) have been employed at positions far from the adsorption site (see text). Note the different scalings of the y axes.*

tion energy (HF level) without counterpoise corrections (independent of the H_2 orientation) is rather an artifact of the finite basis set and not related to any physical interaction.

The benchmark calculations show that the H_2-connector interaction energy can be calculated correctly at the MP2 level with aug-cc-pvTZ basis sets at the H_2 molecule and its closest neighbors, and a small basis (6-31G(d)) for the remaining cluster. However, the BSSE corrections have to be included. The interaction between the hydrogen molecule and the linker can be treated accurately already at the MP2/cc-pvTZ level including the counterpoise correction. Smaller basis sets are not appropriate for this class of weakly bound systems because the underestimate the strength of the interactions and overestimate the equilibrium distances (see Tables 4.5 and 4.6). The difference between MP2 and HF interaction energies can be attributed to London dispersion interactions. In the following the individual high-symmetry H_2 adsorption sites of IRMOF-1 are discussed using the $Zn_4O(HCO_2)_6$ model system.

4.3.2 H_2 Interaction with Building Blocks

The interaction of H_2 with various adsorption site models of IRMOF-1 [**I** to **X** in Figure 4.16] are shown in Figure 4.18 as a function of the H_2-host distances. For the δ adsorption site [Figure 4.16 **I**], where H_2 points to the ring center of the linker in perpendicular orientation, the highest interaction energy of 3.44 kJ mol^{-1} [Figure 4.18 (a)] is very similar to that of H_2 with benzene (3.78 kJ mol^{-1}).[51] The equilibrium distance between the molecular centers of H_2 and the ring is 3.2 Å. This result is close to that of Buda et al.[154] (3.18 kJ mol^{-1} RI-MP2/cc-pvTZ). When H_2 is oriented parallel to the ring (models **II** and **III**), the interaction is 1 kJ mol^{-1} weaker, but the equilibrium distance is about the same. Both parallel orientations are energetically equivalent to each other. The presence of hydroxyl groups does not significantly change the strength of physisorption. No attraction at the HF level [Figure 4.18 (c)] is found for the δ site and so this interaction is attributed exclusively to London dispersion.

Moreover, there is an alternative organic linker site [Figure 4.16 **VIII**–**X**],

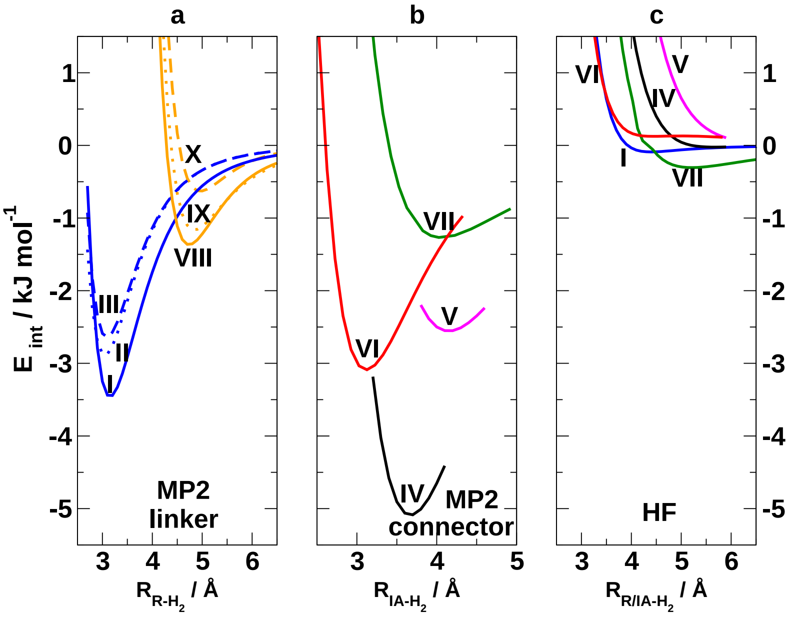

Figure 4.18: *The interaction of H_2 with the IRMOF-1 (a) linker and (b) connector as function of the H_2-host distance. In (c) the electrostatic contribution to the interaction from HF calculations is shown. Model structures and adsorption sites are given in Figure 4.16.*

the so-called ε site. Here the interaction energy (1.4 kJ mol^{-1}) is significantly lower than at the corresponding δ site (see Table 4.7). This result is in good agreement with the results of Buda et al.,[154] who found the interaction energy on the ε site of 1.26 kJ mol^{-1}. However, as many of these sites are present in IRMOF-1 and London dispersion interactions are additive, they probably contribute also to the high H_2 adsorption capacities reported in the experiment.[40,120,131] The distances between the molecular centers for this adsorption site are about 1.5 Å longer than those for the δ site. Both parallel orientations are not equivalent [see Figure 4.18 (a)] and the interaction with H_2 is very weak: 1.16 and 0.63 kJ mol^{-1}.

For the connector model [Figure 4.15 (b)] the interaction mechanism is different [Figure 4.18 (b)]. Although in the adsorption β site, models **VI** and **VII** [Figure 4.16], the Zn atom is well exposed to the H_2 molecule, the lack of other atoms surrounding the H_2 prevents larger dispersion energy

Table 4.7: *Interaction energies calculated at the MP2/cc-pVTZ level and equilibrium distances between the molecular centers of the H_2 molecule and the linker on the ε site.*

Model	ΔE_{int} [kJ mol^{-1}]	d [Å]	$\Delta E_{\mathrm{int}}^{\mathrm{BSSE}}$ [kJ mol^{-1}]	d [Å]
VIII	1.70	4.7	1.36	4.7
IX	1.43	4.8	1.16	4.8
X	1.00	4.9	0.63	5.0

contributions to the binding energy. The strongest interaction is found when H_2 is perpendicular to the central Zn−O bond (model **VI**). The equilibrium distance between the center of H_2 and the closest interaction atom (Zn atom) is 3.1 Å and the interaction energy is 3.1 kJ mol^{-1} (see Table 4.8), which is 0.3 kJ mol^{-1} less than for the H_2-linker interaction. Bordiga et al.[151] found, however, the interaction energy smaller by 1 kJ mol^{-1} than our findings, while their reported equilibrium distance is about the same (3.18 Å). An even smaller interaction energy (1.34 kJ mol^{-1}) was found for this site and the same model by Klontzas et al.[155] at the IR-MP2/TZVPP level. As the interaction is independent (see Table 4.9) on the azimuthal orientation of H_2 to the Zn−O axis, only one perpendicular orientation was studied in detail.

Table 4.8: *Interaction energies calculated at the MP2 level and equilibrium distances between the H_2 molecule and the $Zn_4O(HCO_2)_6$ connector. The distances are given between the molecular center of H_2 and the central O atom (on the α site) and the closest Zn atom (on the β site).*

Orientation	Ads. Site	$\Delta E_{\mathrm{int}}^{\mathrm{BSSE}}$ [kJ mol^{-1}]	d [Å]
Perpendicular 1	α	5.09	3.7
	β	3.09	3.1
Perpendicular 2	α	2.55	4.2
	β	1.27	4.0

A much weaker interaction of only 1.3 kJ mol^{-1} was found for the parallel orientation of H_2 to the central Zn−O bond (model **VII**). The equilibrium distance of 4.0 Å from the Zn atom is more than 1 Å longer than for the

Table 4.9: *Interaction energies calculated at the MP2/6-311G(2d,p) level and equilibrium distances between the* H_2 *molecule and the* $Zn_4O(HCO_2)_6$ *connector. The distances are given between the molecular center of* H_2 *and the central O atom (on the* α *site) and the closest Zn atom (on the* β *site). Both* H_2 *perpendicular orientations are shown.*

Orientation	Ads. Site	ΔE_{int} [kJ mol^{-1}]	d [Å]
Perpendicular 1	α	3.53	3.1
	β	10.26	3.3
Perpendicular 2	α	3.53	3.1
	β	10.28	3.3

perpendicular orientation. These findings are close to the results of Klontzas et al.,[155] who reported an interaction energy of 1.05 kJ mol^{-1} at 3.7 Å. It is important to note that when rotating H_2 at its minimum in complex **VI** by 90° complex **VII** is obtained, with a repulsive H_2-host interaction at that H_2 position. This does not allow a stable configuration of the complex for rotating H_2. Comparing the benchmark calculations with those for the models **VI** and **VII**, the results show that the larger clusters interact less. For model **VI** (3.1 kJ mol^{-1}) compared to **BII** (3.6 kJ mol^{-1}), where the interaction is mainly London dispersion, the difference is small and the binding energy is reduced by only 0.5 kJ mol^{-1}. However, comparing model **VII** (1.27 kJ mol^{-1}) with its smaller analogue **BI** (2.52 kJ mol^{-1}), the interaction is reduced to 50%. The distances between the molecular centers stay unchanged for both models and corresponding orientations. The difference in the interaction energy, when going from the model **BI** to **VII**, is attributed to electrostatics. Obviously, the electrostatic interaction is significantly lower than in the smaller cluster. This is confirmed by HF calculations [see Figure 4.18 (c)], which show no guest-host attraction.

Employing the Mulliken and Natural Bond Orbital (NBO) charges the dipole moment induced on H_2 was estimated, using the point charge approximation. Two cases were considered, where the hydrogen molecule is physisorbed at the clusters **BI** and **VII**. The results were compared with the dipole moment of a strongly polarized H_2 molecule between two point charges of opposite signs, $q^+ \cdots H_2 \cdots q^-$. The point charges were placed on opposite sites of the hydrogen axis at distances of 3.5 Å from the H_2 molecular center. For the $q^+ \cdots H_2 \cdots q^-$ model the induced dipole moment at H_2 is 1.56 Debye using Mulliken charges. This value drops down to 0.20 (0.12 in the NBO model) Debye for the **BI** model and almost vanishes (0.04 (0.02) Debye) for the larger adsorption model **VII**. It can be concluded that in the connector there are no specific polarizing centers. This is also in agreement with the results of Bordiga et al.[151] and Civalleri et al.[129]

Finally, the consideration is focused on the α adsorption site, where H_2 is enclosed in a sort of a pocket of three surrounding Zn atoms and carboxyl groups [see Figure 4.16 **IV** and **V**]. At this site there are more atoms interacting with the hydrogen molecule. This increases the contribution of the dispersive forces to the total binding energy. In model **IV**, H_2 fits very well into the pocket, with various interatomic distances of 3.0−3.7 Å between the H atoms and their surrounding heavier atoms. Consequently the strongest interaction energy is found for this site: 5.1 kJ mol^{-1}. This result is much smaller than that of Sagara et al.,[150] who reported 9.15 kJ mol^{-1} (without BSSE) and 6.86 kJ mol^{-1} (at the 'basis set limit'). On the other hand, the experimental estimation of Bordiga et al.[151] (3.5 kJ mol^{-1}) is by 1.5 kJ mol^{-1} smaller than the results presented in this work. Similar results (3.1 kJ mol^{-1}) are reported in the work of Klontzas et al.[155] The interaction energy is lowered significantly for this binding site if the orientation of H_2 is changed (model **V**). Now only one H atom has many close contacts to the host structure. For this site (model **V**) the energy is estimated as 2.5 kJ mol^{-1} at the equilibrium distance of 4.2 Å between the center of H_2 and the central O atom. This result is again larger by around 1 kJ mol^{-1} than that of Klontzas et al.[155] Comparing the distances between the center of H_2 and the 'interaction atom' for models at the α and β site, larger values for the α site are found. This can be explained again by the geometry of the connector, which permits that many neighboring atoms attract the H_2 guest molecule.

4.4 Summary

The investigations of over 30 structures of so-called isoreticular metal-organic frameworks showed that MOFs are energetically stable systems. The structures studied in this work were built from the tetrahedral moieties $(OZn_4)^{6+}$ (connector) linked by wide range of different organic molecules (linkers). Moreover, the structure of Cu-BTC, with a pseudooctahedral coordination of each metal atom in the connector, was investigated as well.

All energies of formation are negative and strongly dependent on the size and shape of the linker. It was found that the organic linkers in the studied Zn-based MOFs may rotate freely and this rotation can be thermally activated (energy barrier of rotation). This was observed in the NVT ensemble MD simulations already at 300K. MOF lattices have small bulk moduli and are easily compressible. However, stiffer hypothetical linkers, based on carbon cages, have been proposed. Changing the topology of the MOF connector, like in the Cu-BTC crystal, may result in formation of a material with better mechanical properties.

The studied metal-organic frameworks have a charge distribution which is unchanged compared to the building blocks. The only difference is found for atomic charges of the linking oxygen atoms, as they are changed, going from the free linker to the MOF. The electronic properties of these materials reveal a wide range of band gaps (1.0–5.5 eV). Thus, all systems studied here can be classified as semiconductors or insulators. The bands near the Fermi level are dominated by C sp^2 states of the organic linkers. The partial densities of states of the carbon and the zinc atoms are kept almost unchanged when going from the building blocks to the extended MOF crystals. The electronic properties are the same for both, building units and MOF crystals. The knowledge of this fact gives an opportunity to create proper materials for hydrogen storage, optical applications, etc. Longer linkers result in smaller band gaps but, unfortunately, such systems loose their stiffness.

The results from the guest-host interaction show that the physisorption of H_2 in MOFs is mainly due to weak London interaction between linkers and connectors with the hydrogen molecule. The small charge separation in the MOF cannot induce a significant dipole moment in H_2 and thus, the electrostatic interaction plays a minor role. The results of the present work point out that a correct treatment of correlation effects and application of BSSE corrections are essential for the correct estimation of H_2-MOF interaction energies. The H_2-MOF interaction can not be treated correctly with present first-principle DFT functionals. HF can be used to estimate the induced electrostatic effects for well-separated H_2-MOF systems. Also for short distances HF correctly estimates the Pauli repulsion between both moieties. The MP2 method includes all necessary interactions between the guest and the host, and the difference between MP2 and HF results can be attributed to London dispersion. It is essential to have large basis sets at H_2 and the nearest interacting atoms, while moderate bases and pseudo potentials are sufficient elsewhere. The interactions, moreover, need to be corrected for BSSE. It is important to note that adsorption properties can only be calculated on the basis of reasonably large cluster models.

For the studied connector and linker models of IRMOF-1 similar interaction energies with the hydrogen molecule were found. The presented results qualitatively agree with the experiment:[144,145] the strongest interaction is found for site α, with the sequence $\alpha > \beta > \delta \gg \varepsilon$. The most favorable orientation of hydrogen is the orientation perpendicular to the benzene ring or to the central Zn−O bond for the linker and the connector, respectively. However, H_2 can rotate nearly freely and therefore appears as physisorbed sphere rather than linear molecule. Thus, the mean interaction energy cannot be compared only with the most stable orientation of the hydrogen molecule, but has to be averaged over all orientations.

Chapter 5

CONCLUSIONS

The main goal of this work is to search for new stable porous carbon-based materials, which have the ability to accommodate and store hydrogen gas. Theoretical and experimental studies suggest a close relation between the nano-scale structure of the material and its storage capacity. In order to design materials with a high storage capacity, a compromise between the size and the shape of the nanopores must be considered.[12;24] Therefore, a number of different carbon-based materials has been investigated: carbon foams, dislocated graphite, graphite intercalated by C_{60} molecules, and metal-organic frameworks. The structures of interest include experimentally well-known as well as hypothetical systems. The studies were focused on the determination of important properties and special features, which may result in high storage capacities.

Many hypothetical structures can be proposed, but some of them are either not stable or have a rather amorphous character. Novel storage material should be light-weight with large surface areas and a strong surface polarization. They should also have well-defined and controllable pore sizes. Energetic and mechanical stability is of great importance as well. Therefore, carbon-based nanoporous materials are a reasonable choice.

The detailed results of this work were summarized in Sections 3.3 and 4.4 for carbon structures and metal-organic frameworks, respectively. In this chapter, the main conclusions on the applicability of the investigated structures in gas storage will be summarized.

In the first part of this work, graphite-based carbon materials have been discussed. In order to create systems for practical storage applications the graphite interlayer distance needs to be increased. In case of carbon foams this is achieved by a functionalization of the graphene layers. Their one-dimentional system of channels form highly porous structures composed of graphitic strips interconnected with one another by sp^3 hybridized carbon atoms. This results in crystal-like structures with low mass densities. The pore size of the foams is controlled by the length of the strips between two junctions. They are very stable compared to the most stable carbon allotropes (graphite and diamond). Intercalation of the foams by carbon nanotubes improves their mechanical properties. Although the mass densities slightly increase, the intercalants may offer additional sites for gas sorption.

When the radius of a carbon foam cavity is increased (>9 Å) the potential in the middle of the pore becomes weaker.[24] However, carbon foams with optimal size and well defined pores (∼6−8 Å) are good storage materials. At the same time they can reach the gravimetric and volumetric capacities proposed by the DOE.[13] This makes them more reliable storage materials than carbon nanotubes. On the other hand, first computations based on the quantum liquid DFTB method show that smaller pores allow H_2 physisorption only on one of the walls in the cavity.[171] Therefore, due to the large $H_2{-}H_2$ repulsion the opposite wall would be a forbidden region. This could be a factor convincing that the larger pores, rather than small ones, are of greater interest. Larger cavities allow for the adsorption of a second H_2 layer.

Future work could focus on the carbon foam structures derived from ABAB-stacked graphite (like defected graphite) and/or systems with non-hexagonal channels.

In the second part of this work, a large number of metal-organic frameworks were studied. These materials have a three-dimentional interconnected system of pores and the metal sites may be crucial for better gas adsorption as well. MOFs have an easily controllable pore size distribution, they have the lowest known mass densities for crystalline materials. The results of this study show that they are very stable as well.

The investigations show that the H_2-MOFs interactions are mainly due to London dispersion and the electrostatic contribution is negligible. The strength of these interactions is similar on the metal and the organic sites. However, in the extended MOF crystals the always attractive long-range interaction potentials of the nanopores will overlap and superpose to considerable strength, hence a stronger interaction with H_2 is expected. The nanoporosity of MOFs can be tuned in order to maximize the interaction with H_2. The highest storage capacity is expected for those MOFs where the pore size is similar to that of carbon slit-pore materials (∼ 0.6 nm).[12] These expectations correlate with the recent work of Frost et al.,[172] who found that storage capacities in MOFs are proportional to the adsorption energies for low loadings of H_2, while for high loadings the surface area plays a major role.

The results from this work will be used to parameterize the H_2-MOF interaction potential which will allow the estimation of the free interaction energy and the amount of hydrogen uptake using quantum liquid density functional theory.[31] Future work on metal-organic frameworks could cover the investigations of the H_2 interaction with MOFs, which consist of different metal atoms. The systematic theoretical investigations may provide general and specific clues to enhance for example the sorption properties of MOFs and may play a helpful role in the design of new interesting MOF-like systems.

Although the variety of possible pure carbon structures and metal-organic frameworks is almost infinite, the materials described in this work possess the main structural characteristics, which are important for gas storage.

References

1. Schlapbach, L.; Züttel, A. *Nature* **2001**, *414*, 353–358.
2. von Helmolt, R.; Eberle, U. *J. Pow. Sour.* **2007**, *165*, 833–843.
3. Orimo, S. I.; Nakamori, Y.; Eliseo, J. R.; Züttel, A.; Jensen, C. M. *Chem. Rev.* **2007**, *107*, 4111–4132.
4. Züttel, A.; Wenger, P.; Rentsch, S.; Sudan, P.; Mauron, P.; Emmenegger, C. *J. Pow. Sour.* **2003**, *118*, 1–7.
5. Zhou, L.; Zhou, Y. P.; Sun, Y. *Int. J. Hyd. En.* **2004**, *29*, 475–479.
6. Wang, Q.; Johnson, J. K. *J. Chem. Phys.* **1999**, *110*, 557–586.
7. Sudan, P.; Züttel, A.; Mauron, P.; Emmenegger, C.; Wenger, P.; Schlapbach, L. *Carbon* **2003**, *41*, 2377–2383.
8. Perng, T. P.; Wu, J. K. *Mater. Lett.* **2003**, *57*, 3437–3438.
9. Yoon, C. W.; Sneddon, L. G. *J. Am. Chem. Soc.* **2006**, *128*, 13992–13993.
10. Chen, P.; Wu, X.; Lin, J.; Tan, K. L. *Science* **1999**, *285*, 91–93.
11. Dillon, A. C.; Jones, K. M.; Bekkedahl, T. A.; Kiang, C. H.; Bethune, D. S.; Heben, M. J. *Nature* **1997**, *386*, 377–379.
12. Gogotsi, Y.; Dash, R. K.; Yushin, G.; Yildirim, T.; Laudisio, G.; Fischer, J. E. *J. Am. Chem. Soc.* **2005**, *127*, 16006–16007.
13. http://www1.eere.energy.gov/hydrogenandfuelcells/storage/.

14. Schimmel, H. G.; Nijkamp, G.; Kearley, G. J.; Rivera, A.; de Jong, K. P.; Mulder, F. M. *Mater. Sci. Eng. B-Sol. St. Mater. Adc. Tech.* **2004**, *108*, 124–129.

15. Kadono, K.; Kajiura, H.; Shiraishi, M. *Appl. Phys. Lett.* **2003**, *83*, 3392–3394.

16. Liu, C.; Fan, Y. Y.; Liu, M.; Cong, H. T.; Cheng, H. M.; Dresselhaus, M. S. *Science* **1999**, *286*, 1127–1129.

17. Zhu, H. W.; Cao, A. Y.; Li, X. S.; Xu, C. L.; Mao, Z. Q.; Ruan, D. B.; Liang, J.; Wu, D. H. *Appl. Surf. Sci.* **2001**, *178*, 50–55.

18. Seifert, G.; Schulte, J. *Phys. Lett. A* **1994**, *188*, 365–370.

19. Turnbull, J. D.; Boninsegni, M. *Phys. Rev. B* **2005**, *71*, 205421.

20. Banerjee, S.; Murad, S.; Puri, I. K. *Proc. IEEE* **2006**, *94*, 1806–1814.

21. Ströbel, R.; Garche, J.; Moseley, P. T.; Jorissen, L.; Wolf, G. *J. Pow. Sour.* **2006**, *159*, 781–801.

22. Patchkovskii, S.; Tse, J. S.; Yurchenko, S. N.; Zhechkov, L.; Heine, T.; Seifert, G. *Proc. Nat. Acad. Sci. USA* **2005**, *102*, 10439–10444.

23. Rzepka, M.; Lamp, P.; de la Casa-Lillo, M. A. *J. Phys. Chem. B* **1998**, *102*, 10894–10898.

24. Zhechkov, L. *Technische Universität Dresden, PhD thesis, Hydrogen storage in carbon materilas.* **2007**.

25. Nijkamp, M. G.; Raaymakers, J. E. M. J.; van Dillen, A. J.; de Jong, K. P. *Appl. Phys. A-Mater. Sci. Proc.* **2001**, *72*, 619–623.

26. Züttel, A.; Wenger, P.; Sudan, P.; Mauron, P.; Orimo, S. I. *Mater. Sci. Eng. B-Sol. St. Mater. Adv. Tech.* **2004**, *108*, 9–18.

27. Lueking, A. D.; Yang, R. T. *Appl. Cat. A-Gen.* **2004**, *265*, 259–268.

28. Darkrim, F.; Levesque, D. *J. Phys. Chem. B* **2000**, *104*, 6773–6776.

29. Panella, B.; Hirscher, M.; Roth, S. *Carbon* **2005**, *43*, 2209–2214.

30. Kowalczyk, P.; Holyst, R.; Terrones, M.; Terrones, H. *Phys. Chem. Chem. Phys.* **2007**, *9*, 1786–1792.

31. Patchkovskii, S.; Heine, T. *Phys. Chem. Chem. Phys.* **2007**, *9*, 2697–2705.

32. Yaghi, O. M.; O'Keeffe, M.; Ockwig, N. W.; Chae, H. K.; Eddaoudi, M.; Kim, J. *Nature* **2003**, *423*, 705–714.

33. Schlichte, K.; Kratzke, T.; Kaskel, S. *Microp. Mesop. Mater.* **2004**, *73*, 81–88.

34. Li, H.; Eddaoudi, M.; O'Keeffe, M.; Yaghi, O. M. *Nature* **1999**, *402*, 276–279.

35. Panella, B.; Hirscher, M. *Adv. Mater.* **2005**, *17*, 538–541.

36. Rosi, N. L.; Eckert, J.; Eddaoudi, M.; Vodak, D. T.; Kim, J.; O'Keeffe, M.; Yaghi, O. M. *Science* **2003**, *300*, 1127–1129.

37. Rowsell, J. L. C.; Spencer, E. C.; Eckert, J.; Howard, J. A. K.; Yaghi, O. M. *Science* **2005**, *309*, 1350–1354.

38. Ferey, G.; Mellot-Draznieks, C.; Serre, C.; Millange, F.; Dutour, J.; Surble, S.; Margiolaki, I. *Science* **2005**, *309*, 2040–2042.

39. Lin, X.; Jia, J. H.; Zhao, X. B.; Thomas, K. M.; Blake, A. J.; Walker, G. S.; Champness, N. R.; Hubberstey, P.; Schroder, M. *Angew. Chem. Int. Ed.* **2006**, *45*, 7358–7364.

40. Rowsell, J. L. C.; Yaghi, O. M. *J. Am. Chem. Soc.* **2006**, *128*, 1304–1315.

41. Mellot-Draznieks, C.; Ferey, G. *Prog. Sol. St. Chem.* **2005**, *33*, 187–197.

42. Frost, H.; Snurr, R. Q. *J. Phys. Chem. C* **2007**, *111*, 18795–18803.

43. Jung, D. H.; Kim, D.; Lee, T. B.; Choi, S. B.; Yoon, J. H.; Kim, J.; Choi, K.; Choi, S. H. *J. Phys. Chem. B* **2006**, *110*, 22987–22990.

44. Kuc, A.; Zhechkov, L.; Patchkovskii, S.; Seifert, G.; Heine, T. *Nano Lett.* **2007**, *7*, 1–5.
45. Karfunkel, H. R.; Dressler, T. *J. Am. Chem. Soc.* **1992**, *114*, 2285–2288.
46. Kuc, A.; Seifert, G. *Phys. Rev. B* **2006**, *74*, 214104–1–10.
47. Suarez-Martinez, I. *University of Sussex, PhD thesis,Theory of diffiusion and plasticity in layered carbon materials* **2007**.
48. Donchev, A. G. *J. Chem. Phys.* **2007**, *126*, 124706–1–6.
49. Ferre-Vilaplana, A. *J. Chem. Phys.* **2005**, *122*, 104709–1–10.
50. Henwood, D.; Carey, J. D. *Phys. Rev. B* **2007**, *75*, 245413.
51. Heine, T.; Zhechkov, L.; Seifert, G. *Phys. Chem. Chem. Phys.* **2004**, *6*, 980–984.
52. Born, M.; Oppenheimer, R. *Ann. Phys.* **1927**, *84*, 0457–0484.
53. Koch, W.; Holthausen, M. C. *A Chemists Guide to Density Functional Theory*; Wiley-VCH, 2001.
54. Springborg, M. *Methods of Electronic-Structure Calculations: From Molecules to Solids*; Wiley-VCH, 2000.
55. Young, D. *Computational Chemistry: A Practical Guide for Applying Techniques to Real-World Problems*; Wiley-VCH, 2001.
56. Moller, C.; Plesset, M. S. *Phys. Rev.* **1934**, *46*, 0618–0622.
57. Eschrig, H. *The Fundamentals of Density Functional Theory*; EAG Leipzig, 2003.
58. Hohenberg, P.; Kohn, W. *Phys. Rev. B* **1964**, *136*, B864–B871.
59. Kohn, W.; Sham, L. J. *Phys. Rev.* **1965**, *140*, 1133–1138.
60. Hedin, L.; Lundqvis, B. I. *J. Phys. C-Solid State Phys.* **1971**, *4*, 2064–2083.

61. Vosko, S. H.; Wilk, L.; Nusair, M. *Canad. J. Phys.* **1980**, *58*, 1200–1211.

62. Perdew, J. P. *Phys. Rev. B* **1986**, *33*, 8822–8824.

63. Porezag, D.; Frauenheim, T.; Kohler, T.; Seifert, G.; Kaschner, R. *Phys. Rev. B* **1995**, *51*, 12947–12957.

64. Seifert, G.; Porezag, D.; Frauenheim, T. *Int. J. Quantum Chem.* **1996**, *58*, 185–192.

65. Goringe, C. M.; Bowler, D. R.; Hernandez, E. *Reports Prog. Phys.* **1997**, *60*, 1447–1512.

66. Frauenheim, T.; Seifert, G.; Elstner, M.; Hajnal, Z.; Jungnickel, G.; Porezag, D.; Suhai, S.; Scholz, R. *Phys. Status Solidi B* **2000**, *217*, 41–62.

67. Frauenheim, T.; Seifert, G.; Elstner, M.; Niehaus, T.; Kohler, C.; Amkreutz, M.; Sternberg, M.; Hajnal, Z.; Di Carlo, A.; Suhai, S. *J. Phys.* **2002**, *14*, 3015–3047.

68. Eschrig, H.; Bergert, I. *Phys. Status Solidi B* **1978**, *90*, 621–628.

69. Elstner, M.; Porezag, D.; Jungnickel, G.; Elsner, J.; Haugk, M.; Frauenheim, T.; Suhai, S.; Seifert, G. *Phys. Rev. B* **1998**, *58*, 7260–7268.

70. Mulliken, R. S. *J. Chem. Phys.* **1955**, *23*, 1833–1840.

71. Kroto, H. W.; Heath, J. R.; Obrien, S. C.; Curl, R. F.; Smalley, R. E. *Nature* **1985**, *318*, 162–163.

72. Iijima, S. *Nature* **1991**, *354*, 56–58.

73. Novoselov, K. S.; Geim, A. K.; Morozov, S. V.; Jiang, D.; Katsnelson, M. I.; Grigorieva, I. V.; Dubonos, S. V.; Firsov, A. A. *Nature* **2005**, *438*, 197–200.

74. Iijima, S. *J. Cryst. Grow.* **1980**, *50*, 675–683.

75. Kroto, H. W. *Nature* **1992**, *359*, 670–671.

76. Dahl, J. E.; Liu, S. G.; Carlson, R. M. K. *Science* **2003**, *299*, 96–99.

77. McIntosh, G. C.; Yoon, M.; Berber, S.; Tomanek, D. *Phys. Rev. B* **2004**, *70*, 045401–1–8.

78. Smith, B. W.; Monthioux, M.; Luzzi, D. E. *Nature* **1998**, *396*, 323–324.

79. Li, J. L.; Peng, Q. S.; Bai, G. Z.; Jiang, W. *Carbon* **2005**, *43*, 2830–2833.

80. Tomanek, D. *Phys. B* **2002**, *323*, 86–89.

81. Liu, A. Y.; Cohen, M. L. *Phys. Rev. B* **1992**, *45*, 4579–4581.

82. Liu, A. Y.; Cohen, M. L.; Hass, K. C.; Tamor, M. A. *Phys. Rev. B* **1991**, *43*, 6742–6745.

83. Mailhiot, C.; Mcmahan, A. K. *Phys. Rev. B* **1991**, *44*, 11578–11591.

84. Hoffmann, R.; Hughbanks, T.; Kertesz, M.; Bird, P. H. *J. Am. Chem. Soc.* **1983**, *105*, 4831–4832.

85. Guerin, K.; Pinheiro, J. P.; Dubois, M.; Fawal, Z.; Masin, F.; Yazami, R.; Hamwi, A. *Chem. Mater.* **2004**, *16*, 1786–1792.

86. Gupta, V.; Nakajima, T.; Ohzawa, Y.; Zemva, B. *J. Fluor. Chem.* **2003**, *120*, 143–150.

87. Deng, W. Q.; Xu, X.; Goddard, W. A. *Phys. Rev. Lett.* **2004**, *92*, 166103–1–4.

88. He, H. Y.; Klinowski, J.; Forster, M.; Lerf, A. *Chem. Phys. Lett* **1998**, *287*, 53–56.

89. Lerf, A.; He, H. Y.; Forster, M.; Klinowski, J. *J. Phys. Chem. B* **1998**, *102*, 4477–4482.

90. Telling, R. H.; Ewels, C. P.; El-Barbary, A. A.; Heggie, M. I. *Nat. Mater.* **2003**, *2*, 333–337.

91. Suarez-Martinez, I.; Savini, G.; Heggie, M. I. *Heggie, M. I.*, 'First Principles Modelling of Dislocations in AA Graphite', 'Conference-Carbon 2006', Aberdeen.

92. Gupta, V.; Scharff, P.; Risch, K.; Romanus, H.; Müller, R. *Solid State Comm.* **2004**, *131*, 153–155.

93. Balaban, A. T.; Klein, D. J.; Folden, C. A. *Chem. Phys. Lett.* **1994**, *217*, 266–270.

94. Umemoto, K.; Saito, S.; Berber, S.; Tomanek, D. *Phys. Rev. B* **2001**, *64*, 193409–1–3.

95. Klett, J.; Hardy, R.; Romine, E.; Walls, C.; Burchell, T. *Carbon* **2000**, *38*, 953–973.

96. Klett, J. W.; McMillan, A. D.; Gallego, N. C.; Walls, C. A. *J. Mater. Sci.* **2004**, *39*, 3659–3676.

97. Ribeiro, F. J.; Tangney, P.; Louie, S. G.; Cohen, M. L. *Phys. Rev. B* **2005**, *72*, 214109–1–6.

98. Blank, V. D.; Buga, S. G.; Serebryanaya, N. R.; Denisov, V. N.; Dubitsky, G. A.; Ivlev, A. N.; Mavrin, B. N.; Popov, M. Y. *Phys. Lett. A* **1995**, *205*, 208–216.

99. Serebryanaya, N. R.; Blank, V. D.; Ivdenko, V. A.; Chernozatonskii, L. A. *Solid State Comm.* **2001**, *118*, 183–187.

100. Talyzin, A. V.; Dubrovinsky, L. S.; Oden, M.; Le Bihan, T.; Jansson, U. *Phys. Rev. B* **2002**, *66*, 165409–1–7.

101. Vanvechten, J. A.; Keszler, D. A. *Phys. Rev. B* **1987**, *36*, 4570–4573.

102. Wang, Z. W.; Zhao, Y. S.; Tait, K.; Liao, X. Z.; Schiferl, D.; Zha, C. S.; Downs, R. T.; Qian, J.; Zhu, Y. T.; Shen, T. D. *Proc. Nat. Acad. Sci. USA* **2004**, *101*, 13699–13702.

103. Park, N.; Ihm, J. *Phys. Rev. B* **2000**, *62*, 7614–7618.

104. Bucknum, M. J.; Castro, E. A. *J. Chem Theory Comput.* **2006**, *2*, 775–781.

105. Monkhorst, H. J.; Pack, J. D. *Phys. Rev. B* **1976**, *13*, 5188–5192.

106. Wang, C. X.; Yang, Y. H.; Liu, Q. X.; Yang, G. W.; Mao, Y. L.; Yan, X. H. *Appl. Phys. Lett.* **2004**, *84*, 1471–1473.

107. Dresselhaus, M. S.; Dresselhaus, G. *Adv. Phys.* **1981**, *30*, 139–326.

108. Fuhrer, M. S.; Hou, J. G.; Xiang, X. D.; Zettl, A. *Sol. St. Comm.* **1994**, *90*, 357–360.

109. Köster, A. M.; Flores, R.; Geudtner, G.; Goursot, A.; Heine, T.; Patchkovskii, S.; Reveles, J. U.; Vela, A.; Salahub, D. R. **2003**, deMon.

110. Krätschmer, W.; Lamb, L. D.; Fostiropoulos, K.; Huffman, D. R. *Nature* **1990**, *347*, 354–358.

111. Greenwood, N. N.; Earnshaw, A. *Chemistry of the Elements*; Elsevier: Amsterdam, 1997.

112. Dresselhaus, M. S.; Dresselhaus, G. *Annu. Rev. Mater. Sci.* **1995**, *25*, 487–523.

113. O'Keeffe, M.; Eddaoudi, M.; Li, H. L.; Reineke, T.; Yaghi, O. M. *J. Solid State Chem.* **2000**, *152*, 3–20.

114. Rosi, N. L.; Eddaoudi, M.; Kim, J.; O'Keeffe, M.; Yaghi, O. M. *Cryst. Eng. Comm.* **2002**, 401–404.

115. Chui, S. S. Y.; Lo, S. M. F.; Charmant, J. P. H.; Orpen, A. G.; Williams, I. D. *Science* **1999**, *283*, 1148–1150.

116. Rowsell, J. L. C.; Yaghi, O. M. *Microp. Mesop. Mater.* **2004**, *73*, 3–14.

117. Eddaoudi, M.; Moler, D. B.; Li, H. L.; Chen, B. L.; Reineke, T. M.; O'Keeffe, M.; Yaghi, O. M. *Acc. Chem. Res.* **2001**, *34*, 319–330.

118. Panella, B.; Hirscher, M.; Puetter, H.; Mueller, U. *Adv. Funct. Mater.* **2006**, *16*, 520–524.

119. Eddaoudi, M.; Kim, J.; Rosi, N. L.; Vodak, D.; Wachter, J.; O'Keeffe, M.; Yaghi, O. M. *Science* **2002**, *295*, 469–472.

120. Rowsell, J. L. C.; Yaghi, O. M. *Angew. Chem. Int. Ed.* **2005**, *44*, 4670–4679.

121. Eddaoudi, M.; Li, H. L.; Yaghi, O. M. *J. Am. Chem. Soc.* **2000**, *122*, 1391–1397.

122. Seo, J. S.; Whang, D.; Lee, H.; Jun, S. I.; Oh, J.; Jeon, Y. J.; Kim, K. *Nature* **2000**, *404*, 982–986.

123. Halder, G. J.; Kepert, C. J.; Moubaraki, B.; Murray, K. S.; Cashion, J. D. *Science* **2002**, *298*, 1762–1765.

124. Krawiec, P.; Kramer, M.; Sabo, M.; Kunschke, R.; Frode, H.; Kaskel, S. *Adv. Eng. Mater.* **2006**, *8*, 293–296.

125. Fuentes-Cabrera, M.; Nicholson, D. M.; Sumpter, B. G.; Widom, M. *J. Chem. Phys.* **2005**, *123*, 124713–1–5.

126. Braga, C. F.; Longo, R. L. *J. Mol. Struct.-Theochem* **2005**, *716*, 33–38.

127. Mattesini, M.; Soler, J. M.; Yndurain, F. *Phys. Rev. B* **2006**, *73*, 094111–1–8.

128. Kim, D.; Lee, T. B.; Choi, S. B.; Yoon, J. H.; Kim, J.; Choi, S. H. *Chem. Phys. Lett.* **2006**, *420*, 256–260.

129. Civalleri, B.; Napoli, F.; Noel, Y.; Roetti, C.; Dovesi, R. *Crystengcomm* **2006**, *8*, 364–371.

130. Kuc, A.; Enyashin, A.; Seifert, G. *J. Phys. Chem. B* **2007**, *111*, 8179–818.

131. Rowsell, J. L. C.; Millward, A. R.; Park, K. S.; Yaghi, O. M. *J. Am. Chem. Soc.* **2004**, *126*, 5666–5667.

132. McSkimin, H. J.; Andreatch, P., J.; Glynn, P. *J. App. Phys.* **1972**, *43*, 985–987.

133. Ahuja, R.; Fast, L.; Eriksson, O.; Wills, J. M.; Johansson, B. *J. App. Phys.* **1998**, *83*, 8065–8067.

134. Karzel, H.; Potzel, W.; Kofferlein, M.; Schiessl, W.; Steiner, M.; Hiller, U.; Kalvius, G. M.; Mitchell, D. W.; Das, T. P.; Blaha, P.; Schwarz, K.; Pasternak, M. P. *Phys. Rev. B* **1996**, *53*, 11425–11438.

135. Wang, Q. M.; Shen, D. M.; Bulow, M.; Lau, M. L.; Deng, S. G.; Fitch, F. R.; Lemcoff, N. O.; Semanscin, J. *Microp. Mesop. Mater.* **2002**, *55*, 217–230.

136. Vishnyakov, A.; Ravikovitch, P. I.; Neimark, A. V.; Bu1low, M.; Wang, Q. M. *Nano Lett.* **2003**, *3*, 713–718.

137. Pierson, J. F.; Thobor-Keck, A.; Billard, A. *Appl. Surf. Sci.* **2003**, *210*, 359–367.

138. Santra, K.; Sarkar, C. K.; Mukherjee, M. K.; Ghosh, B. *Thin Solid Films* **1992**, *213*, 226–229.

139. Ray, S. C. *Sol En. Mater. Sol. Cel.* **2001**, *68*, 307–312.

140. Ching, W. Y.; Xu, Y. N.; Wong, K. W. *Phys. Rev. B* **1989**, *40*, 7684–7695.

141. Kawakami, T.; Takamizawa, S.; Kitagawa, Y.; Maruta, T.; Mori, W.; Yamaguchi, K. *Polyhedron* **2001**, *20*, 1197–1206.

142. Li, H.; Eddaoudi, M.; Groy, T. L.; Yaghi, O. M. *J. Am. Chem. Soc.* **1998**, *120*, 8571–8572.

143. Collins, D. J.; Zhou, H. C. *J. Mater. Chem.* **2007**, *17*, 3154–3160.

144. Rowsell, J. L. C.; Eckert, J.; Yaghi, O. M. *J. Am. Chem. Soc.* **2005**, *127*, 14904–14910.

145. Yildirim, T.; Hartman, M. R. *Phys. Rev. Lett.* **2005**, *95*, 215504–1–4.

146. Mueller, T.; Ceder, G. *J. Phys. Chem. B* **2005**, *109*, 17974–17983.

147. Samanta, A.; Furuta, T.; Li, J. *J. Chem. Phys.* **2006**, *125*, 084714–1–8.

148. Grimme, S. *J. Comp. Chem.* **2006**, *27*, 1787–1799.

149. Zhechkov, L.; Heine, T.; Patchkovskii, S.; Seifert, G.; Duarte, H. A. *J. Chem. Theory Comput.* **2005**, *1*, 841–847.

150. Sagara, T.; Klassen, J.; Ganz, E. *J. Chem. Phys.* **2004**, *121*, 12543–12547.

151. Bordiga, S.; Vitillo, J. G.; Ricchiardi, G.; Regli, L.; Cocina, D.; Zecchina, A.; Arstad, B.; Bjorgen, M.; Hafizovic, J.; Lillerud, K. P. *J. Phys. Chem. B* **2005**, *109*, 18237–18242.

152. Sagara, T.; Ortony, J.; Ganz, E. *J. Chem. Phys.* **2005**, *123*, 214707–1–6.

153. Sagara, T.; Klassen, J.; Ortony, J.; Ganz, E. *J. Chem. Phys.* **2005**, *123*, 014701–1–4.

154. Buda, C.; Dunietz, B. D. *J. Phys. Chem. B* **2006**, *110*, 10479–10484.

155. Klontzas, E.; Mavrandonakis, A.; Froudakis, G. E.; Carissan, Y.; Kopper, W. *J. Phys. Chem. C* **2007**, *111*, 13635–13640.

156. Kuc, A.; Heine, T.; Seifert, G.; Duarte, H. A. *Theoret. Chem. Acc* **2008**, accepted.

157. Kuc, A.; Heine, T.; Seifert, G.; Duarte, H. A. *Angew. Chem. Int. Ed.* **2008**, submitted.

158. Mulder, F. M.; Dingemans, T. J.; Wagemaker, M.; Kearley, G. J. *CHem. Phys.* **2005**, *317*, 113–118.

159. Yang, Q. Y.; Zhong, C. L. *J. Phys. Chem. B* **2006**, *110*, 655–658.

160. Lee, T. B.; Kim, D.; Jung, D. H.; Choi, S. B.; Yoon, J. H.; Kim, J.; Choi, K.; Choi, S. H. *Catalysis Today* **2007**, *120*, 330–335.

161. Sun, Y. Y.; Kim, Y. H.; Zhang, S. B. *J. Am. Chem. Soc.* **2007**, *129*, 12606–12607.

162. Li, Y. W.; Yang, F. H.; Yang, R. T. *J. Phys. Chem. C* **2007**, *111*, 3405–3411.

163. Negri, F.; Saendig, N. *Theor. Chem. Acc.* **2007**, *118*, 149–163.

164. Perdew, J. P.; Burke, K.; Ernzerhof, M. *Phys. Rev. Lett.* **1996**, *77*, 3865–3868.

165. Boys, S. F.; Bernardi, F. *Mol. Phys.* **1970**, *19*, 553–566.

166. Becke, A. D. *J. Chem. Phys.* **1993**, *98*, 5648–5652.

167. R., D.; Hehre, W. J.; Pople, J. A. *J. Chem. Phys.* **1971**, *54*, 724–728.

168. Frisch, M. J. et al. Gaussian, Inc., Wallingford, CT, 2004.

169. Lee, C.; Yang, W.; Parr, R. G. *Phys. Rev. B* **1988**, *37*, 785–789.

170. Kendall, R. A.; Dunning Jr., T. H.; Harrison, R. J. *J. Chem. Phys.* **1992**, *96*, 6796–6806.

171. Martinez, A. *Private communication* **2007**.

172. Frost, H.; Duren, T.; Snurr, R. Q. *J. Phys. Chem. B* **2006**, *110*, 9565–9570.

Versicherung § 5 Abs. 1 Nr. 5

Versicherung nach § 5 Abs. 1 Nr. 5 der Promotionsordnung der Fakultät Mathematik und Naturwissenschaften an der Technischen Universität Dresden in der Fassung vom 16. April 2003:

a) Hiermit versichere ich, dass ich die vorliegende Arbeit ohne unzulässige Hilfe Dritter und ohne Benutzung anderer als der angegebenen Hilfsmittel angefertigt habe; die aus fremden Quellen direkt oder indirekt übernommenen Gedanken sind als solche kenntlich gemacht. Die Arbeit wurde bisher weder im Inland noch im Ausland in gleicher oder ähnlicher Form einer anderen Prüfungsbehörde vorgelegt.

b) Die vorliegende Arbeit wurde in der Arbeitsgruppe Theoretische Chemie am Institut für Physikalische Chemie an der Technischen Universität Dresden unter der wissenschaftlichen Betreuung von Prof. Gotthard Seifert angefertigt.

c) Hiermit versichere ich, dass ich keine früheren erfolglosen Promotionsverfahren bestritten habe.

d) Hiermit erkenne ich die Promotionsordnung der Fakultät Mathematik und Naturwissenschaften an der Technischen Universität Dresden in der Fassung vom 16. April 2003 an.

Datum Unterschrift